# DESIGN OF PASSIVE MILLIMETER-WAVE COAXIAL COMPONENTS FOR ADDITIVE MANUFACTURING

by

LJUBODRAG B. BOSKOVIC

B.S., University of Belgrade, Serbia, 2010

A thesis submitted to the

Faculty of the Graduate School of the

University of Colorado in partial fulfillment

of the requirement for the degree of

Master of Science

Electrical, Computer, and Energy Engineering Department

2022

Committee Members:

Prof. Dejan S. Filipovovic

Dr. Mohamed Elmansouri

Dr. W. Neill Kefauver

Dr. Erik Lier

Ljubodrag B. Boskovic (MSc., Electrical, Computer, and Energy Engineering Department University of Colorado Boulder)

Design of Passive Millimeter-Wave Coaxial Components for Additive Manufacturing

Thesis directed by Professor Dejan S. Filipovic.

Additive manufacturing is gaining popularity in many different areas across engineering and science, with functional devices and systems being used for both prototyping and end-use. Steady improvement in the accuracy of 3D printing technologies has seen their increased adoption for RF applications deep into millimeter-wave frequencies. This thesis presents an overview of the current commercially available 3D printing techniques and examples of their utilization for fabrication of high-end RF components.

Coaxial lines have seldom been considered, mainly due to the challenges associated with the physical support of the inner conductor. This work demonstrates an implementation of additive manufacturing for the fabrication of non-radiating components such is air-filled coaxial transmission lines also used as a mechanical anchor in an RF system and quadrature hybrid. Both components are designed and measured as stand-alone devices. On the system level, a coaxial anchor is integrated with a helix antenna also designed for additive manufacturing. The design feasibility is demonstrated in the direct metal laser sintering (DMLS) process for coaxial anchor, coaxial quadrature hybrid, and helical antenna integrated with the coaxial anchor for millimeter-wave frequencies 18GHz to 40GHz. Each device has a specific band inside the mentioned frequency range.

The stereolithography (SLA) process is also used, however, mainly for proof of concept fabrication prior to the DMLS fabrication. Also, the SLA and the fused deposition modeling (FDM) are used for radome fabrication for helical antenna

environmental protection enhancement. The environmental impact on helical antenna performances is assed with a thermal/pressure chamber developed in this thesis. The designed systems can achieve good performance across a wide, instantaneous bandwidth (air-filled coaxial anchor and helical antenna) and low levels of imbalances (coaxial quadrature hybrid). Also, the environmental impact is minimal on AUT performances.

# DEDICATION

To my beautiful wife Dragana and our two lovely kids Neda and Novak.

# ACKNOWLEDGMENT

This work is funded by Lockheed Martin Space Corporation and the Office of Naval Research.

I can not express my gratitude for how much I owe to Prof. Dejan S. Filipovic for all help and support. Thank you Filip! Hvala najlepse!

Also, Mohamed, Maxim, Gaeron, and Songyi thank you all for your help!

CONTENTS

CHAPTER

I. INTRODUCTION ..... 1

1.1. Historical Background and Motivation ..... 1

1.2. Additive Manufacturing Technology ..... 2

1.2.1. Polymer Additive Manufacturing ..... 4

1.2.1.1. Stereolithography ..... ..... 4

1.2.1.2. Selective Laser Sintering ..... 5

1.2.1.3. Fused Deposition Modeling..... 6

1.2.1.4. Multi-Jet Fusion..... ..... 7

1.2.1.5. Poly Jet..... ..... 8

1.2.1.6. Binder Jetting..... ..... 9

1.2.1.7. Carbon Digital Light Sinthesis ..... ..... 10

1.2.2. Metal Additive Manufacturing Technology ..... 12

1.2.2.1. Direct Metal Laser Sintering..... .. 12

1.2.2.2. Selective Laser Melting..... ..... ..... 12

1.2.2.3. Electron Beam Melting..... ..... 13

1.2.2.4. Directed Energy Deposition..... ..... ..... 13

1.2.3. Hybrid Additive Manufacturing Technology ..... 15

1.2.3.1. Powder Bed Fusion..... 15

1.2.3.2. Conductive Ink printing..... 16

1.2.3.3. Atomic Difusion Additive Manufacturing..... 17

1.3. Thesis Organization and Contribution ..... 18

1.3.1. Organization ..... 18

1.3.2. Contributions ..... 19

II. DESIGN OF RF ANCHOR ..... 20

2. Introduction..... 20

2.1. Coaxial Anchor Design: Mechanical Perspective..... 22

2.2. Coaxial Anchor Design: Electrical Perspective..... 27

2.3. Fabrication and Measurements..... 30

2.4. Conclusion..... 33

III. DESIGN OF COAXIAL QUADRATURE HYBRID ..... 34

3. Introduction..... 34

3.1. Quadrature Coaxial Hybrid Design ..... 35

3.2. Quadrature Coaxial Hybrid Fabrication and Measurements . 39

3.3. Conclusion..... 42

IV. DESIGN AND CHARACTERIZATION OF A 3D PRINTED HELICAL ANTENNA MONOLITHICALLY INTEGRATED AND FED BY AN AIR-LOADED COAXIAL LINE..... 43

4. Introduction..... 43

4.1. Helical Antenna Design..... 45

4.2. Helical Antenna with Integrated Coaxial Anchor: Fabrication and Measurements ..... 51

4.3. Conclusion..... 56

V. 3D PRINTED RADOME DESIGN FOR MILLIMETER-WAVE HELICAL ANTENNA AND ENVIRONMENTAL TESTING..... 58

5. Introduction..... 58

5.1. Radome Design and Results..... 60

5.2. Helical Antenna Radome Fabrication and Measurements Results..... 64

5.3. Radom Measurements Results in Thermal/Pressure Chamber..... 76

5.4. Conclusion..... 88

VI. CONCLUSION..... 89

BIBLIOGRAPHY.....91

TABLES

Table

1. Critical Polymer Additive Manufacturing Parameters of Interest for RF...11
2. Critical Metal Additive Manufacturing Parameters of Interest for RF .....15
3. Critical Hybrid Additive Manufacturing Parameters of Interest for RF ....18
4. Critical DMLS Parameters of Interest for RF Anchor…….. .....22
5. Parameters of the Helical Antenna with Integrated Coaxial Anchor ……..47
6. DMLS and SLA Parameters.....58
7. Helical Antenna Parameters ……59
8. Thermal/Pressure Chamber Material Properties ……..78

FIGURES

Figure

1. Stereolithography proces concept ……...4
2. Selective laser sintering process concept ……6
3. Fused deposition modeling concept ……...7
4. Multi-jet fusion process concept……8
5. Poly jet process concept…..…….9
6. Binder jetting concept ……..10
7. Direct metal laser sintering system ……12
8. Direct energy deposition concept ……..14
9. Conductive ink printing ……..17
10. A 3D model of the half-coaxial anchor with its constitutive features (a), and photograph of the inspected component with subtractive method on a CNC machine post DMLS fabrication and characterization (b)……. .....22
11. Simplified mechanical drawing of the shorted stub coaxial approach as an anchoring block. All dimensions are in mm .....23
12. Static diagram…… .....24
13. The RF anchor with escape holes. .....29
14. Simulated effects of the escape holes on anchor's S-parameters; a) reflection coefficient, b) transmission coefficient .....29
15. Simulated effects of the different stubs spacing .....30
16. Post-processing and assembling of the designed anchor. Also shown is one of the excavated models, further indicating good mechanical contact and line integrity across the length of the device .....31

17. Simulated and measured S-parameters of fabricated device, a) reflection coefficient, b) transmission coefficient ..... 32
18. Simulated and measured VSWR of the two fabricated devices ..... 33
19. The geometry of the quadrature hybrid for microstrip configuration..... 35
20. Layout of the coaxial quadrature hybrid..... 36
21. Coaxial quadrature hybrid geometry ..... 37
22. Designed components in a split block configuration..... 37
23. S parameters simulation results ..... 38
24. Simulated results for amplitude imbalances ..... 38
25. Simulated results for phase imbalances ..... 39
26. Fabrication and assembling..... 40
27. Measured S parameters ..... 41
28. Measured vs. simulated amplitude imbalances..... 41
29. Measured vs. simulated phase imbalances..... 42
30. Helical antenna configuration (a), and illustration of helix parameters (b)……..44
31. Helical antenna diameter impact on a bandwidth ..... 46
32. A cross-section of the designed helical antenna with an integrated coaxial anchor (a), Simulation setup in ANSYS HFSS with annotated structural parts of this system (b) ..... 47
33. Simulated VSWR for antenna with integrated coaxial feed..... 48
34. Broadside realized co- and cross-polarized gains..... 48
35. Total efficiency..... 49
36. Axial ratio at broadside. The designed elevation cone for this antenna is 14°……..... 49
37. Normalized radiation patterns at 24GHz (a), 25GHz (b) ..... 50
38. Normalized radiation patterns at 26GHz (a), 27GHz (b) ..... 50

39. Normalized radiation patterns at 28GHz ..... 51
40. Helical antenna proof of concept fabrication in SLA process ..... 52
41. Helical antenna as fabricated in DMLS and deployed post-processing steps..... 52
42. VSWR results. Redline simulation, solid black DMLS, and black dashed SLA measurements results ..... 53
43. Photographs of the antenna inside the chamber with the absorber placed around it (left) and without absorber (right) ..... 53
44. Measured and simulated broadside (co- and cross-polarized) gains ..... 54
45. Measured and simulated efficiency (taken as the ratio of realized gain and directivity) ..... 54
46. Measured and simulated axial ratios at broadside and 14° elevation ..... 55
47. Measured and simulated radiation patterns at 24GHz (a), 25GHz (b) ..... 55
48. Measured and simulated radiation patterns at 26GHz (a), 27GHz (b) ..... 56
49. Measured and simulated radiation patterns at 28GHz..... 56
50. Helical antenna with integrated coaxial line and radome (a), Radome dimensions (b), Helical antenna computational model (c). Dimensions in mm ..... 60
51. VSWR for the simulated antenna with no radome and with the radome.... 61
52. Realized broadside gain for a millimeter-wave helix with the radome ..... 62
53. Axial ratio with and without radome ..... 62
54. Radiation patterns at 24 GHz (a) and 26 GHz (b), Co- (solid) and cross- (dashed) polarized, black line without radome and red line with radome case ..... 63
55. Radiation patterns at 28 GHz (a) and 30 GHz (b), Co- (solid) and cross- (dashed) polarized, black line without radome and red line with radome case ..... 63
56. Radiation patterns at 30 GHz, Co- (solid) and cross- (dashed) polarized, black line without radome and red line with radome case ..... 64
57. Formlabs Form 3 printer (a) and Rise 3D printer ..... 65

58. Fabricated radomes in Tough V5 resin (a), Rigid 4k resin (b), PLA (c), and LDPE (d) ..... 65
59. Assembled antenna system and PLA radome ..... 66
60. VSWR measurements with FDM fabricated radomes ..... 67
61. VSWR measurements with SLA fabricated radomes ..... 67
62. Anechoic chamber setup ..... 68
63. SLA Fomlabs Tough V5 resin measured vs. simulated broadside gain ..... 69
64. SLA Formlabs Tough V5 resin measured vs. simulated axial ratio ..... 69
65. SLA Fomlabs Rigid 4k resin measured vs. simulated broadside gain ..... 70
66. SLA Formlabs 4k resin measured vs. simulated axial ratio ..... 70
67. FDM LLDPE measured vs. simulated broadside gain ..... 71
68. FDM LLDPE measured vs. simulated axial ratio ..... 71
69. FDM PLA measured vs. simulated broadside gain ..... 73
70. FDM PLA measured vs. simulated axial ratio ..... 73
71. Low permittivity study at broadside ..... 74
72. Low permittivity at theta angle 14˚ ..... 74
73. Radiation patterns at 24 GHz (a) and 26 GHz (b), Co- (solid) and cross- (dashed) polarized, red simulation and blue measurements with PLA material ..... 75
74. Radiation patterns at 28 GHz (a) and 30 GHz (b), Co- (solid) and cross- (dashed) polarized, red simulation and blue measurements with PLA material ..... 75
75. Radiation patterns at 28 GHz, Co- (solid) and cross- (dashed) polarized, red simulation and blue measurements with PLA material ..... 76
76. Thermo-electric element ..... 79
77. Thermo-electric pump efficiency diagram ..... 79
78. Thermal/Pressure chamber layout ..... 80
79. Custom adapter design ..... 81
80. Thermal system block diagram and fully assembled system ..... 81

81. Pressure system analysis ..... 82
82. Pressure system block diagram ..... 83
83. Thermal/Pressure measurement system layout ..... 83
84. Connecting and reconnecting test ..... 84
85. Cooling temperature measurement ..... 85
86. Vacuum/Pressure measurement ..... 86
87. Heating temperature measurements ..... 86
88. Measured VSWR for cooling and heating ..... 87
89. VSWR for vacuum and pressure condition at -22C° ..... 87
90. VSWR for vacuum and pressure condition at 50C° ..... 88

# CHAPTER I

# INTRODUCTION

## 1.1. Historical Background and Motivation

Manufacturing industries are constantly seeking better ways to improve fabrication tolerances, building volume, and capacity and, at the same time, reduce the cost, energy consumption, material usage, etc.

Traditional subtractive manufacturing relies on drilling, milling, grinding, or casting into molds. These methods allow high accuracy, good control of surface finishes, and a high production rate; however, material and energy consumption are not always in favor of subtractive techniques. This raises the question of future sustainability in the mentioned manufacturing areas.

On the other hand, adaptive manufacturing, one of the youngest manufacturing thicknesses, has been rapidly grooving since its introduction in the 1960s. That proliferation significantly expanded after additive manufacturing was commercialized in 1987. As mentioned in [1], the commercial life of additive manufacturing started with stereolithography (SLA) from 3D Systems, a process that solidifies thin layers of light-sensitive liquid polymer using an ultraviolet (UV) laser. [1]. Since the 2000s, in the additive manufacturing market, many companies have tried to push the limits in fabrication limits and bring AM closer to regular consumers, which has caused the production price and cost of hardware maintenance to decrease rapidly.

Stand-alone components [2] and integrated RF subsystems [3] and [4] have been demonstrated in transmission line configurations mainly revolving around rectangular and ridge waveguides due to their simplicity.

This work will try to answer whether it is possible to implement additive manufacturing, mainly direct metal laser sintering (DMLS), to design and fabricate millimeter-wave coaxial devices like air-filled coaxial transmission lines, quadrature hybrids, and helical antennas.

### 1.2. Additive Manufacturing Technology

Additive manufacturing is the process of making a three-dimensional solid object made out of 2D layers. The printing process is controlled through 3D printing software that generates the printing program for each geometry. The geometry is modeled in CAD modeling software, and typically it is converted into a digital STereoLithography (STL) file [5]. In general, two types of resolution define the printing process, specifically, layer thickness resolution in the z-axis direction and x-y plane resolution. The z-axis resolution can mainly be controlled by 3D printing software, while an x-y plane resolution is predefined by the printer manufacturer. Additive manufacturing is also considered distinct from traditional machining techniques, which mostly rely on the removal of material by methods such as cutting or drilling (subtractive processes).

In order to implement additive manufacturing for the millimeter-wave application first, it is necessary to make a brief overview of commercially available methods and compare their performances. In general, there are three categories:

- Polymer (dielectric) based additive manufacturing prints layers of polymer material either through extrusion, ultraviolet curing with laser, or laser fusion.

Typical advantages of the polymer additive manufacturing process are:

- high level of accuracy,
- high material diversity,
- lower manufacturing system cost.

The disadvantages are:

- metallization is needed for RF applications,

- lower material strength than metals.
- high loss in dielectric,
- limited availability of permittivity.

- Metal additive manufacturing technique fuses or melts layers of metallic powder material together. The powder material is metal alloys. Typically, the process is conducted inside an inert gas environment used to protect the process from oxygen in the atmosphere, which can cause a porous structure.

Advantages of metal 3D printing:

- complex geometries are available with little post-processing,
- a low-cost method in comparison with conventional methods of manufacturing,
- highly efficient usage of material.

Limits of metal 3D printing

- comparatively slow for regular objects,
- surface finishing is not on a level like conventional machining,
- thermal post-processing is needed,
- tolerance and precision are usually lower in comparison with CNC machining,
- design for metal 3D printing can be more complicated than other manufacturing methods.

- Hybrid 3D printing represents the combination of different additive manufacturing methods, which requires the specific post-processing of the fabricated parts in order for them to be used as final products [6].

Advantages of hybrid 3D printing:

- consisting of combination of different materials and processes,
- complex geometries with multi-material structures.

Disadvantages are:

- high manufacturing system complexity,
- high level of post-processing.

### 1.2.1. Polymer Additive Manufacturing

#### 1.2.1.1. Stereolithography

SLA, emerged in the mid-1980s and established itself as a staple of additive manufacturing (now known as 3D printing) over the next decade. Parts are built by curing tin layers of liquid photosensitive resin using an UV laser that draws on the surface of a resin, turning it from a liquid into a solid layer. Fresh, uncured resin is swept over the preceding layer as each layer is completed, and the process is repeated until the part is finished. The layer thickness is typically from 15 microns up to 50 microns depending on the resin type. A post-build process is required on SLA parts, which undergo a UV-curing cycle to fully solidify the outer surface of the part. The next step in post-processing is printing supports removal and improvement of the surface finish on the surfaces exposed to the supports by sanding or CNC machining if needed. The typical SLA process [7], [10] is presented in Fig. 1.

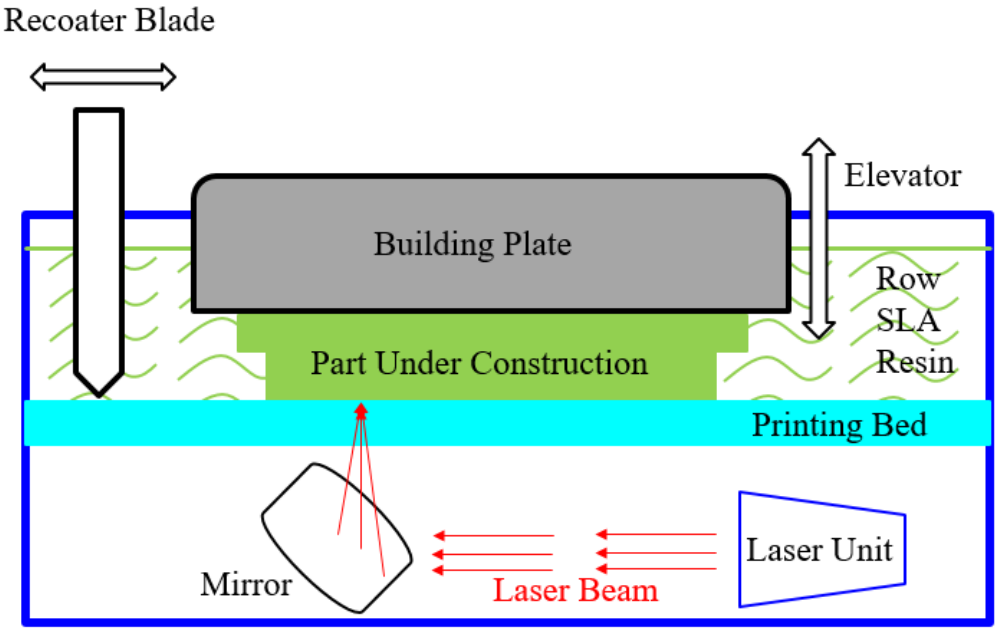


Fig. 1. Stereolithography process block diagram.

#### 1.2.1.2. Selective Laser Sintering

The selective laser sintering (SLS) process uses polymer-like powder as a building material. The powder [8], [10] is dispersed in a thin layer on a platform inside the build chamber. The printer preheats the powder to a temperature just below the melting point of the raw material. This makes it easier for the laser beam to raise the temperature of specific regions of the powder bed as it traces the layer of the model. After the laser passes, the area traces are solidified. This fuses the particles mechanically to create one solid part. The unfused powder supports the part during printing and eliminates dedicated support structures.

The build platform lowers by one layer into the build chamber, typically between 50 to 200 microns, and a recoater applies a new layer of powder material on top. The laser then scans the next layer of the model. A description of the SLS process is presented in Fig. 2. This process repeats for each layer until parts are complete, and the finished parts are left to cool down gradually inside the printer.

Once parts have cooled, the operator removes the build chamber from the printer and transfers it to a cleaning station, separating the printed parts and cleaning the excess powder.

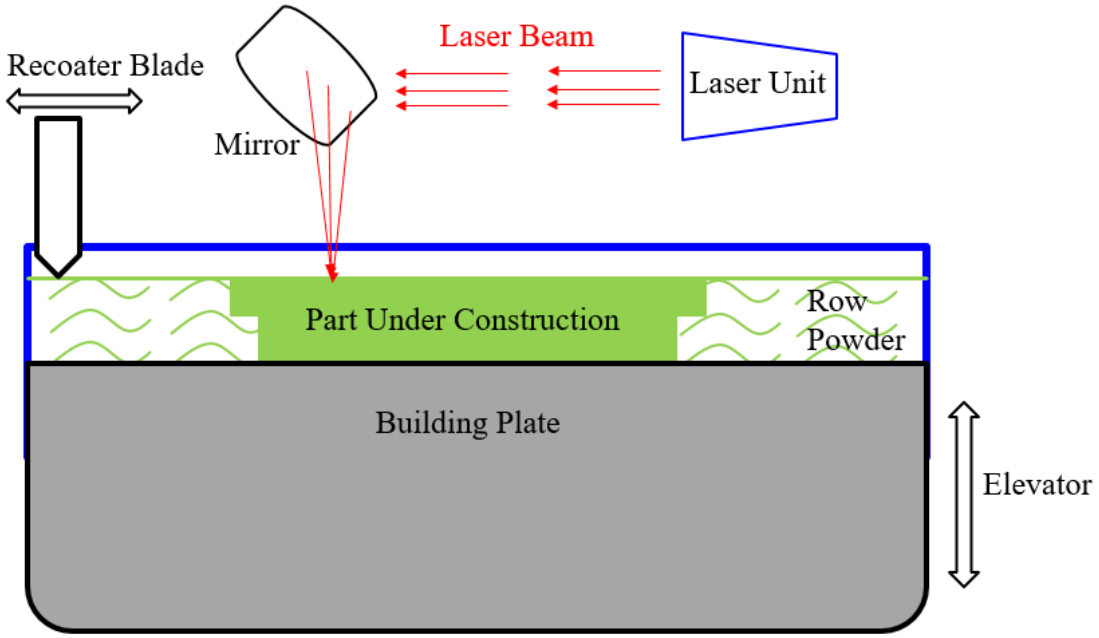


Fig. 2. Selective laser sintering process concept.

1.2.1.3. Fused Deposition Modeling

Fused deposition modeling (FDM) fabrication uses material extrusion to print items, where a feedstock material is pushed through an extruder. In most fused filament fabrication 3D printing machines, the feedstock material comes from a filament wound onto a spool [9], [10].

Extruders for these printers have a cold end and a hot end. The cold end pulls material from the spool, using gear- or roller-based torque and controlling the feed rate by employing a stepper motor. The cold end pushes feedstock into the hot end. The hot end consists of a heating chamber and a nozzle. The heating chamber hosts the liquefier, which converts the feedstock into a liquid state. It allows the molten material to exit from the small nozzle to form a thin bead of plastic that will adhere to the material it is laid on. The nozzle diameter is usually between 0.2 mm and 1.0 mm. Different types of nozzles and heating methods are used depending on the printed material. The typical FDM process is presented in Fig. 3.

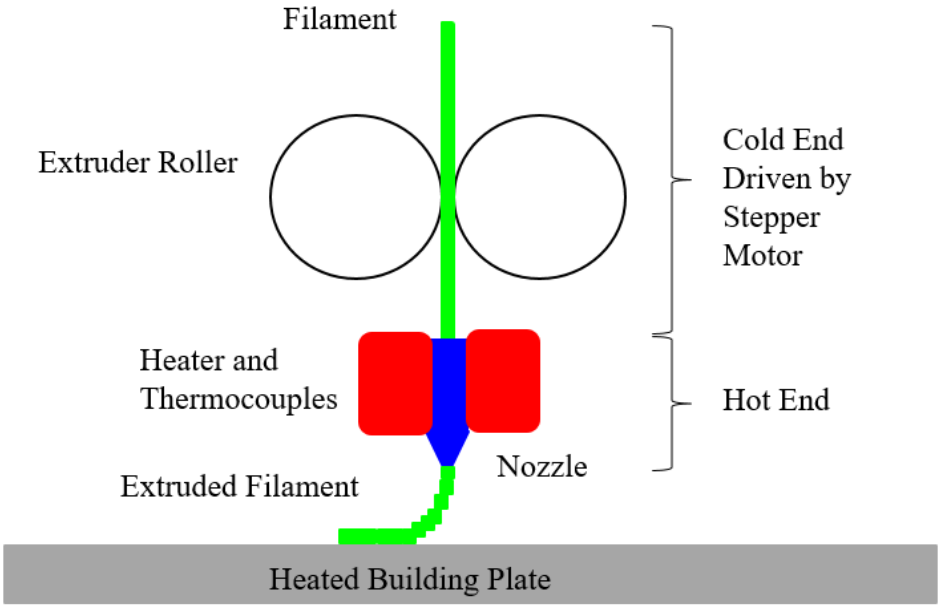


Fig. 3. Fused deposition modeling concept.

1.2.1.4. Multi-Jet Fusion

Multi-jet fusion is an industrial 3D printing process that produces functional nylon prototypes and end-use production parts [10]. Final parts exhibit quality surface finishes, fine feature resolution, and more consistent mechanical properties when compared to processes like selective laser sintering.

Multi Jet Fusion uses an inkjet array to apply to fuse selectively and detailing agents across a bed of nylon powder, which are then fused by heating elements into a solid layer. After each layer, the powder is distributed on top of the bed, and the process repeats until the part is complete.

When the build finishes, the entire powder bed with the encapsulated parts is moved to a processing station where an integrated vacuum removes most of the loose powder. Parts are then bead blasted to remove any remaining residual powder before ultimately reaching the finishing department, where they are dyed black to improve cosmetic appearance. Fig. 4 shows the basic concept of the multi-jet fusion process.

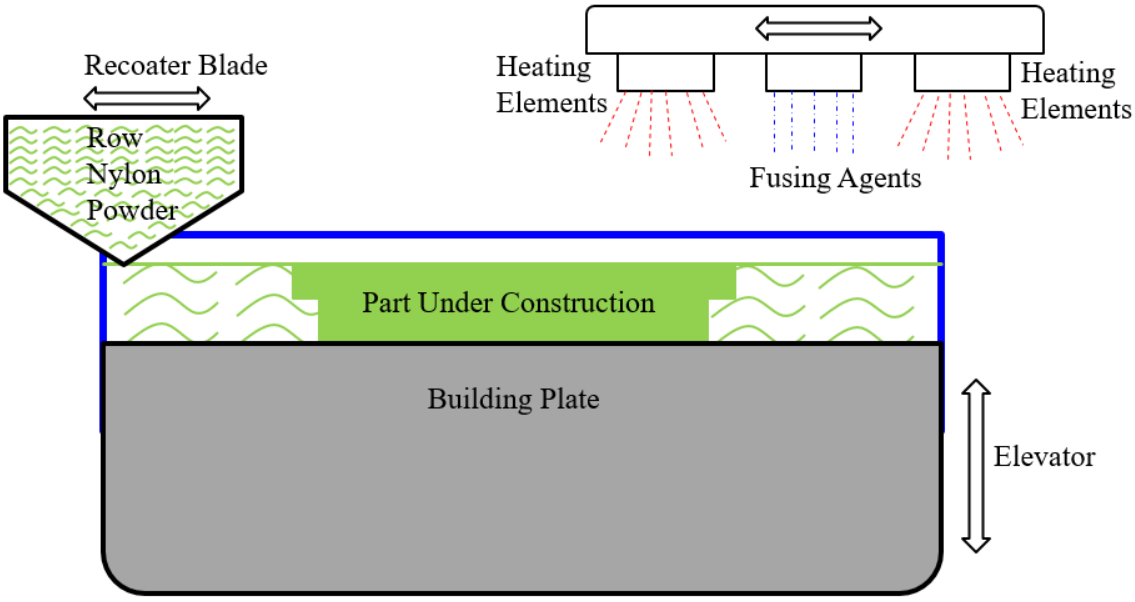


Fig. 4. Multi-jet fusion process concept.

1.2.1.5. Poly Jet

The poly jet process is one of the few industrial 3D printing technologies that allow multiple materials in a single part build [10]. It is one of the few technologies that can print these materials together in a single layer. In addition, different colors and hardness levels can be combined, again in a single layer just one-fourth the thickness of a sheet of printer paper. PolyJet uses a jetting process where tiny droplets of liquid photopolymer, called voxels, are sprayed from multiple jets onto a build platform and cured with layers that form elastomeric parts. This digital approach provides excellent accuracy and the ability to alter material properties in a way never before possible strategically. The poly jet was introduced in 2005 and is a mature, well-understood technology. As with other 3D printing processes, it builds parts from the bottom up, one layer at a time.

The poly jet uses a print head equipped with multiple jets to spray tiny droplets of liquid photopolymer 42 microns across, forming layers 30 microns thick. An ultraviolet light source then cures these layers. Support material is printed simultaneously. When the build is complete, the part gets a quick bath in a chemical

solution, dissolving the supports and leaving smooth surfaces. The poly jet process is presented in Fig. 5.

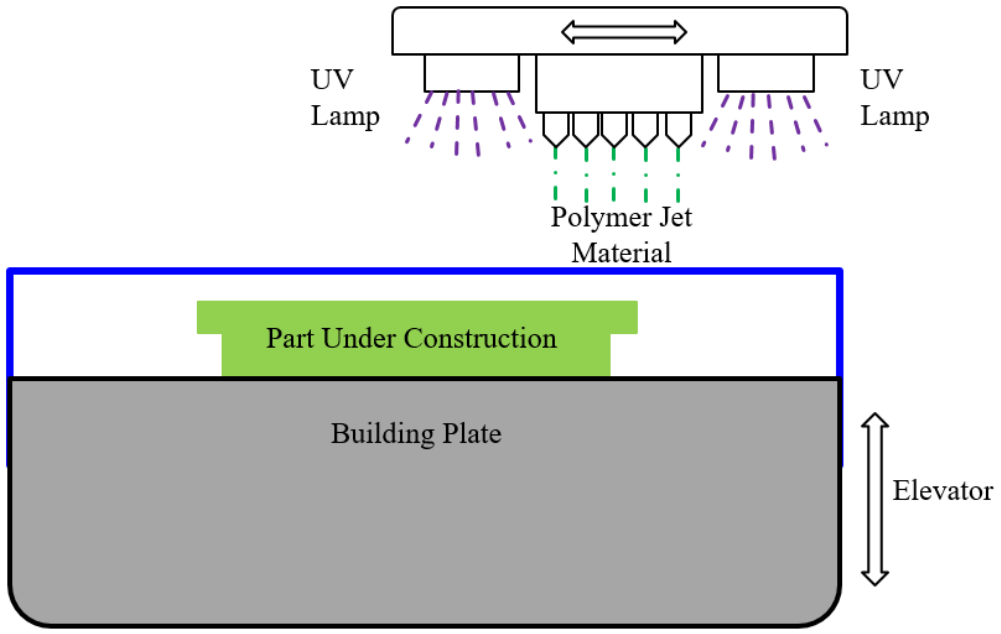


Fig. 5. Poly jet process concept.

1.2.1.6. Binder Jetting

The binder jetting process uses a powder-based material and a binder [11]. The binder is usually liquid, and the build material is in powder form. The binder acts as an adhesive by bonding the powder-like material in traces forming the sliced layer of a model. A print head moves horizontally along the x and y axes of the machine and deposits alternating layers of the build material and the binding material. After each layer, the printed object is lowered on its build platform. Due to the binding method, the material characteristics are not always suitable for structural parts. As with other powder-based manufacturing methods, the object being printed is self-supported within the powder bed and is removed from the unbound powder once completed. The technology is often referred to as 3DP technology and is copyrighted under this name. Fig. 6 represents the basic concept of binder jet printing.

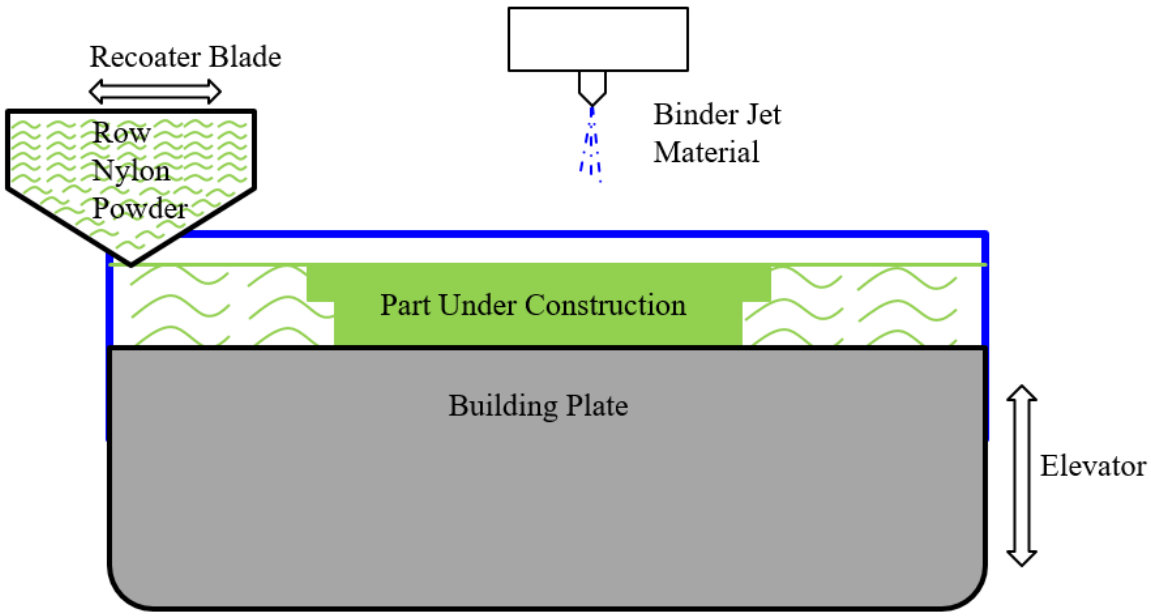


Fig. 6. Binder jetting concept.

1.2.1.7. Carbon Digital Light Synthesis

Carbon digital light synthesis (DLS) is an industrial 3D printing process that creates functional, end-use parts with mechanically isotropic properties and smooth surface finishes [10]. Carbon DLS uses continuous liquid interface production (CLIP) technology to produce parts through a photochemical process that balances light and oxygen. It works by projecting light through an oxygen-permeable window into a reservoir of UV-curable resin. The CLIP process core is a thin, liquid interface of uncured resin between the window and the printing part. Light passes through that area, curing the resin above it to form a solid part. Resin flows beneath the curing part as the print progresses, maintaining the continuous liquid interface that powers CLIP. Following the build, the 3D-printed part is baked in a forced-circulation oven where heat sets off a secondary chemical reaction that causes the materials to adapt and strengthen.

Table 1 gives an overview of the polymer additive manufacturing techniques and possible implementation for RF devices.

TABLE 1
Critical Polymer Additive Manufacturing Parameters of Interest for RF

| 3D Printing Technique | Tolerances | Layer Thickness | Minimum Feature Size | Materials | Material Options | Application to RF |
|---|---|---|---|---|---|---|
| Stereo-lithography (SLA) | +/-0.05mm plus 0.001 per each mm | 0.0254mm to 0.1016mm | About 0.5mm depending on aspect ratio | ABS-like PC-like PP-like | Single material at a time | Need Cu plating thus chemistry must be considered |
| Selective Laser Sintering (SLS) | +/-0.25mm plus 0.0015 per each mm | 0.1mm | 0.762mm | PA12 PA11 PA12 40% Glass-filled PA12 Mineral-filled TPU-70A | Single material at a time | Need Cu plating thus chemistry must be considered |
| Multi Jet Fusion | +/-0.3mm plus 0.002 per each mm | 0.08mm | 0.5mm | PA12 PA12 40% Glass-filed | Single material at a time | Need Cu plating thus chemistry must be considered |
| Poly Jet | +/-0.1mm plus 0.001 per each mm | 0.03mm | 0.3mm | Digital-Clear Digital-Black Digital-White | Multi - Material | Need Cu plating thus chemistry must be considered |
| Fused Deposition Modeling (FDM) | +/-0.2mm | 0.01mm | 0.2mm | PLA, ABS | Multi - Material | Need Cu plating thus chemistry must be considered |
| Carbon Digital light Synthesis (DLS) | +/-0.25mm plus 0.0015 per each mm | 0.1mm | 0.5mm | Carbon RPU 70 Carbon FPU 50 | Single Material at a time | Need Cu plating; thus chemistry must be considered |

### 1.2.2. Metal Additive Manufacturing Technology

#### 1.2.2.1. Direct Metal Laser Sintering

Direct metal laser sintering (DMLS) is an additive manufacturing method that builds prototypes using a laser to fuse fine metal powder selectively [10]. The keyword is fusing, meaning that powder material does not reach a melting temperature. DMLS parts need support structures for anchoring the part to the build plate, reducing or eliminating warping, and supporting overhanging geometry. Support structures are further required to support overhanging geometry because the spreading would move unsupported overhands. Examples of these geometry types are horizontal surfaces, large holes in the horizontal access, angled surfaces, arches, and overhangs. Fig. 7 represents the basic concept of the DMLS printing process.

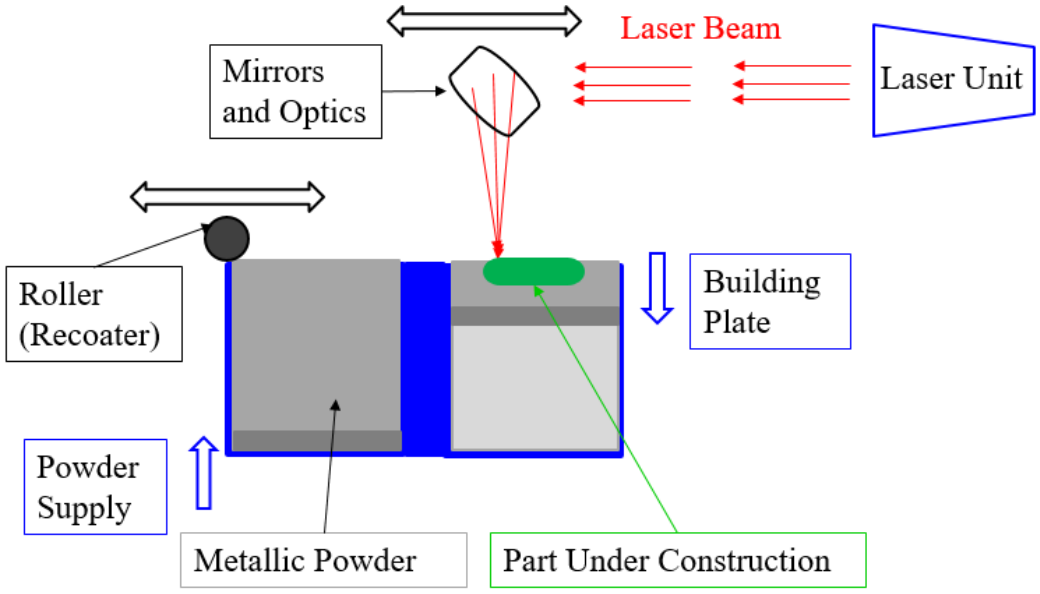


Fig. 7. Direct metal laser sintering system.

#### 1.2.2.2. Selective Laser Melting

The selective laser melting (SLM) additive manufacturing technique uses similar equipment like DMLS [12]. However, the temperature of the laser focal point at the surface of the powder metal alloy is above the melting temperature. 3D printing happens in an inert gas environment. Thanks to that, a 3D print has parameters close

to the one that was produced with casting. SLM is mainly used for manufacturing parts from titanium and aluminum.

#### 1.2.2.3. Electron Beam Melting

The electron beam melting (EBM) is similar to SLM; however, an electron beam is used instead of a laser. This technology is considered to be faster and more precise than laser-based printing, but the difference is not so significant. This technology is used mainly for manufacturing objects from titanium and cobalt.

#### 1.2.2.4. Directed Energy Deposition

Directed energy deposition (DED) covers a range of terminology: 'Laser engineered net shaping, directed light fabrication, direct metal deposition, 3D laser cladding. It is a more complex printing process commonly used to repair or add additional material to existing components [12].

A typical DED machine consists of a nozzle mounted on a multi-axis arm, which deposits melted material onto the specified surface, where it solidifies. The process is similar in principle to material extrusion, but the nozzle can move in multiple directions and is not fixed to a specific axis. The material, which can be deposited from any angle due to 4 and 5 axis machines, is melted upon deposition of the material with a laser or electron beam. The process can be used with polymers and ceramics but is typically used with metals in either powder or wire.

Typical applications include repairing and maintaining structural parts, and the basic concept is presented in Fig. 8.

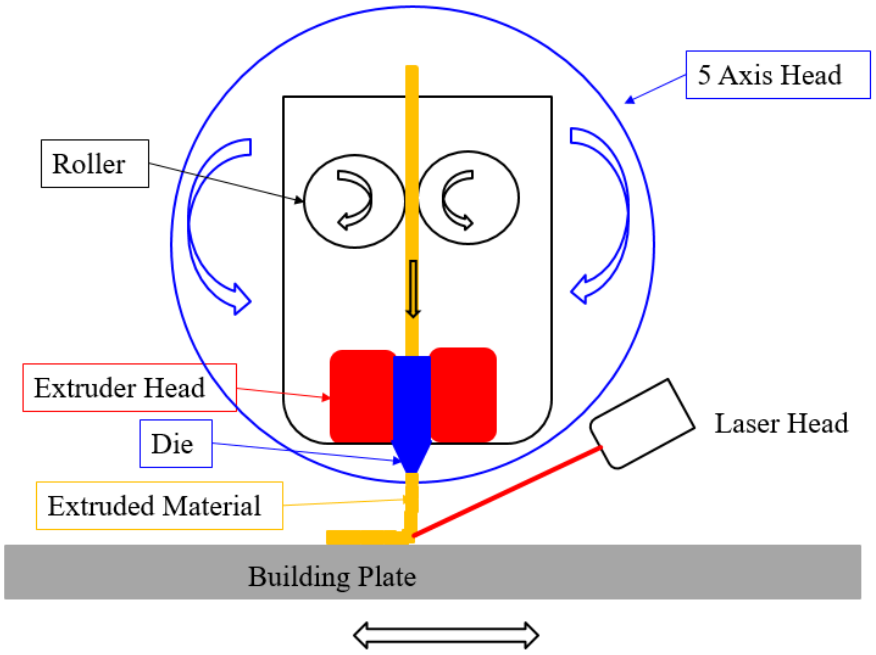


Fig. 8. Direct energy deposition concept.

Table 2 gives an overview of the metal additive manufacturing techniques and possible implementation for RF devices.

TABLE 2

Critical Metal Additive Manufacturing Parameters of Interest for RF

| 3D Printing Technique | Tolerances | Layer Thickness | Minimum Feature Size | Materials | Material Options | Application to RF |
|---|---|---|---|---|---|---|
| Direct Metal Laser Sintering (DMLS) | +/-0.076mm plus 0.001 per each mm | 0.02mm to 0.3mm | About 0.153mm to 0.381 | AlSi10Mg<br>Cobalt hrome<br>Inconel 718<br>SS 17-4 PH<br>SS 316L<br>Ti 6-4<br>CuNi2SiCr | Single material at a time | Applicable for monolithic Air Coax. Challenge is to keep >2mm long section w/o inner conductor' support |
| Direct Energy Deposition (DED) | +/-0.075mm plus 0.04 per each 25 mm | 0.089 to 0.203mm | 0.762mm | Titanium, Inconel 718, 625, Stainless Steel (300 series), Aluminum Alloys (2319, 4043), Zinc Alloys, Copper-Nickel Alloys | Single material at a time | Not applicable for air-filed coax, coaxial quadrature hybrid or helical antenna. More applicable for solid metal devices like horn antennas. |

### 1.2.3. Hybrid Additive Manufacturing Technology

#### 1.2.3.1. Powder Bed Fusion

The Powder Bed Fusion process includes the following commonly used printing techniques: DMLS, Electron beam melting (EBM), Selective heat sintering (SHS), SLM, and SLS, [13].

Powder bed fusion (PBF) methods use either a laser or electron beam to melt and fuse the powder. Electron beam melting (EBM) methods require a vacuum but can be used with metals and alloys to create functional parts. All PBF processes involve the spreading of the powder material over previous layers. Different mechanisms enable

this, including a roller or a blade. A hopper or a reservoir below the bed provides a fresh material supply. DMLS is the same as SLS, but with metals and not plastics. The process sinters the powder layer by layer. SHS differs from other processes by using a heated thermal print head to fuse powder material. As before, layers are added with a roller in between the fusion of layers. A platform lowers the model accordingly.

#### 1.2.3.2. Conductive Ink Printing

Conductive ink printing is a method where a numerically controlled machine controls the position of the inkjet printing head with conductive paint. It is making traces by extruding the paint and changing the position of the head. Typically is used on a substrate that can be previously 3D printed in any other additive manufacturing method, mainly SLA, SLS, and FDM, [14], [15]. However, it can apply conductive ink on PCB boards of any kind and CNC machined parts.

The advantage of this system is that it can create conductive traces of very high complexity, and it is not restricted to 2D planes like PCM printing. The disadvantages are that ink is not highly conductive. Also, it is necessary to have the base fabricated in other methods to get a 3D shape, which indicates that alignment can be challenging. An example of an antenna fabricated in conductive ink printing is presented in Fig. 9.

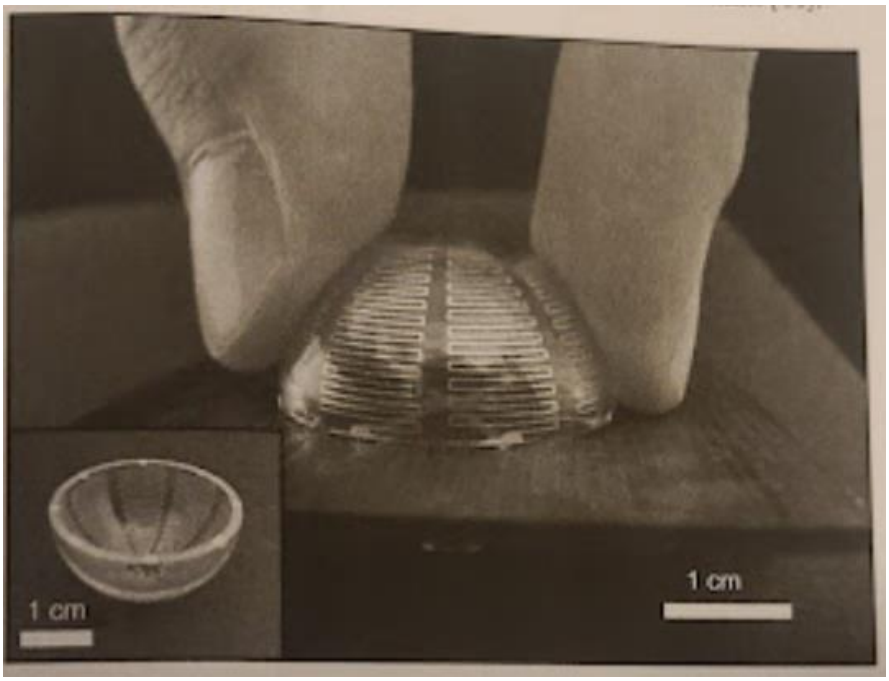


Fig. 9. Conductive ink printing [14].

1.2.3.3. Atomic Diffusion Additive Manufacturing

Atomic diffusion additive manufacturing (ADAM) is a process that uses a plastic-bound material powder formed into a 3D shape a layer at the time [16]. Material is deposited through the extruder. After the printing process, typically, the part is washed in a de-binding solution and sintered in a furnace. The sintering step burns off the plastic binder and causes the metal powder to diffuse.

Three-dimensional printing with ADAM technology can create metal parts with high accuracy, making it a valued contribution to the manufacturing of end-use parts, legacy parts, prototypes, and tooling. Most parts printed with ADAM are not fully solid -- they include triangular infill. This can be both an advantage and a disadvantage. It means lighter weight parts at the cost of total density. For small geometries, fully dense parts are printable.

Unlike most other metal printers, ADAM machines do not expose users to losing metal powder -- resulting in a safer, easier to use the system. The machines are usable

with a wide variety of materials that can be easily swapped out for one another. ADAM has the same geometric constraints as standard FDM printers.

Table 3 gives an overview of the hybrid additive manufacturing techniques and possible implementation for RF devices.

TABLE 3

Critical Hybrid Additive Manufacturing Parameters of Interest for RF

| 3D Printing Technique | Tolerances | Layer Thickness | Minimum Feature Size | Materials | Material Options | Application to RF |
|---|---|---|---|---|---|---|
| Atomic Diffusion Additive Manufacturing (ADAM) | +/-0.15mm for range of dimensions 30 to 50mm | 0.05mm to 0.125mm | Tested not below 1mm | 17-4PH Stainless Steel Copper Alloy H13 Tool Steel Inconel 625 A2 and D2 Tool Steel | Single material at a time | Applicable for monolithic air-coax, quadrature hybrid and helical antenna. Challenge is to control geometry after heat treatment |
| Conductive Inc Printing | 0.08mm to 0.115mm | 0.02mm to 0.75mm | 0.150mm | Silver based ink | Single material at a time | Not air-fled coax and helical antenna. It is applicable for other devices like printed beam forming network. |

## 1.3. Description Organization and Contributions

### 1.3.1. Organization

The data presented in this thesis are obtained from numerical simulations and measurements of fabricated articles. Ansys HFSS numerical simulation package is used in this research [17]. The thesis is organized as follows:

Chapter 2 introduces the air-filled RF anchor design and presents studies from mechanical and electrical perspective. The design and measurements results are presented to demonstrate the validity of the developed concepts.

Chapter 3 introduces the air-field coaxial quadrature hybrid design and measurements. Branch-line topology is built in DMLS and results are favorably compared with simulation.

Chapter 4 introduces the RF anchor integrated with the helical antenna operating over wide mmW bandwidth. The design and measurements results are presented.

Chapter 5 describes the approach for environmental protection and testing of antennas. Testing and measurements are conducted on an in-house designed and built test bench system which can control ambient temperature and pressure, emulating some in-flight conditions.

### 1.3.2. Contributions

This work introduces an approach for designing passive millimeter-wave coaxial components for additive manufacturing. The design process for air-filled transmission lines is developed from both, electrical, and mechanical perspective. The design approaches for an air-filled quadrature hybrid and helical antenna with an integrated coaxial anchor are also presented. Finally, the design of environmental protection for a helical antenna with a test-bed system for low altitude flying conditions testing is presented with results of temperature/pressure drifting effect on the VSWR antenna performances.

# CHAPTER II

# DESIGN OF THE RF ANCHOR

## 2. Introduction

This work demonstrates the potential for a circular coaxial line designed for DMLS fabrication to achieve good performance across a wide instantaneous bandwidth that is of interest for many contemporary applications.

Coaxial lines have several distinct advantages when used for RF applications. They feature wideband single (TEM) mode operation, low loss, low dispersion, dense packaging with low self-interference, and a wealth of designs for compatible components. In the last 15 years, coaxial line developments have been focused mainly on the realm of surface micromachining [18], [19]. Processes such as PolyStrata can achieve a high level of monolithic integration around a nearly-air-loaded rectangular coaxial line. This is done with unprecedented levels of high accuracy and low roughness, with monolithic integration on a wafer-scale and 3 to 4 vertical layers. However, technologies like this are not widely available and therefore expensive for both research and development as well as commercialization. This work shows the efficacy of 3D printing as a good alternative for the fast development of functional coaxial prototypes.

Coaxial lines have been demonstrated with additive manufacturing [20], [21]. Conventionally, the line is formed by filling the void in the center of a coaxial printed dielectric with liquid metal and coating the exterior to complete the RF coax. While this technique and similar works have shown some success in various applications, the challenge of post-processing steps, particularly ensuring correct filling with liquid metal conductors, begins to negate the benefit of AM. An alternative approach features a 3D printed coaxial filter geometry in stereolithography (SLA) or selective

laser sintering (SLS) that is first built in the split-block arrangement. Then, it is copper plated to achieve the required functionality [22]. Plagued with integration complexities, machine tolerances, and heavy-duty post-processing, this technique is somewhat limited in its widespread use for high-end components and systems.

This work proposes a short piece of air-loaded circular cross-section coaxial line as a fundamental building block of an all-metal coaxial RF subsystem, referred to as a coaxial anchor. The central conductor of the coax line is shorted to the outer conductor (walls) using quarter-wave stubs at prescribed locations (see Fig. 10-a). The increasing width toward the shorted end is an additional feature developed to support the fabrication process and enhance the mechanical strength for the component's further use. The RF performance is tuned by the selection of characteristic impedances, line lengths, and their shape. To allow for an un-sintered metal powder to be removed, escape holes (often referred to as release holes in surface micromachining) are used. Their size and positioning are chosen to minimize the negative impact on the anchor performance, including losses, reflections, and undesired radiation. Special attention is given to the transition to the 2.4 mm connectors, wherein the internal parameters are also accounted for in the RF performance of the anchor. The entire full-wave design was carried out having in mind the current requirements and limitations of the direct metal laser sintering (DMLS) process [13]. The anchor, shown in Fig.1, is built in a copper alloy with some features in Table 4 [10]. Tests of the 12 mm long component agree well with the simulations and show a low insertion loss of $< 0.4$ dB and return loss $> 20$ dB over the 20-39 GHz range. Controlled subtractive inspection is carried out to assess the quality of the fabrication (see Fig. 10-b), and the most relevant findings are discussed.

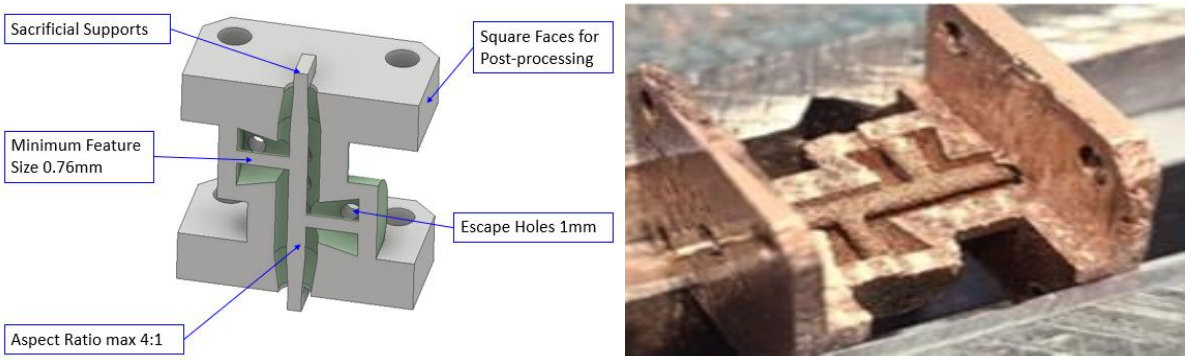


(a) (b)

Fig. 10. A 3D model of the half-coaxial anchor with its constitutive features (a), and photograph of the inspected component with subtractive method on a CNC machine post DMLS fabrication and characterization (b).

TABLE 4.
Critical DMLS Parameters of Interest for RF Anchor [10].

| DMLS Parameters and Printing Guidelines | |
|---|---|
| Tolerances | +/-0.076 mm plus 0.001 per mm |
| Layer Thickness | 20 to 30 µm |
| Minimum Feature Size | 0.153mm to 0.381mm |
| Powder Material | Copper / CuNi2SiCr |

2.1. Coaxial Anchor Design: Mechanical Perspective

The design and performance of individual parts constituting an RF component must be assessed from a mechanical point of view. For example, a traditional coaxial line has inner and outer conductors with a dielectric separating them, integrated with two connector assemblies. This is a total of five "individual parts." Clearly, fabrication challenges dictated by the process itself are accompanied by the assembly constraints needed to ensure proper RF connection. They both heavily depend on tolerances, fabrication challenges associated with the sample preparation, orientation within the building volume, and associated complexities which magnify if the low-cost is an

added requirement imposed on the component development or use. With AM technology becoming more pervasive, the question becomes if we can utilize its advantages by monolithically fabricating the RF components and avoiding some assembly. For example, combining the inner and outer conductor as a single part and replacing the dielectric support with air reduces the number of parts to three: a single air-loaded coax and two connectors' assemblies.

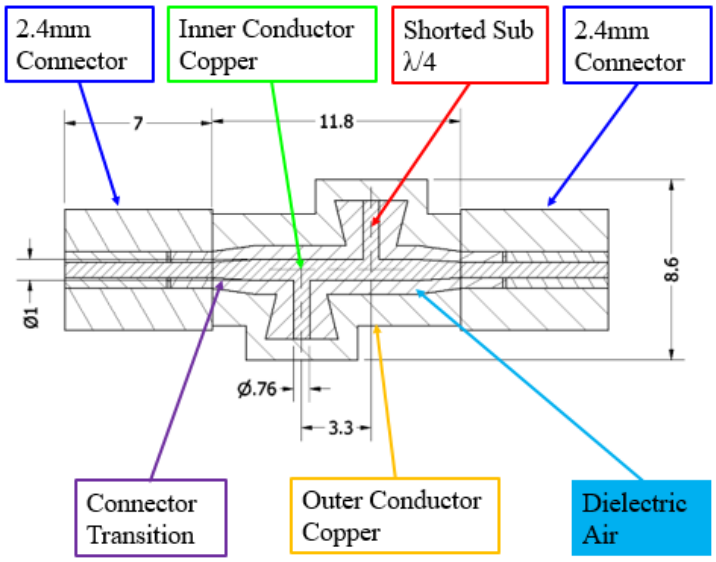


Fig. 11. Simplified mechanical drawing of the shorted stub coaxial approach as an anchoring block, all dimensions are in mm.

By connecting the inner and outer conductors with shorted quarter-wave stubs [23], a DMLS 3D printing approach can be used to fabricate a short coaxial transmission line block. These components can be used with minimal post-processing as a baseline mechanical integration anchor for the RF system. A simplified mechanical drawing of a shorted stub approach coaxial anchor with a 50 Ω nominal characteristic impedance is shown in Fig. 11. As seen, the two quarter-wave (at 27.5 GHz) stubs act as "anchors" for the structure. They provide mechanical stability and can help in the thermal domain by acting as thermal vias. Mechanical and thermal loading can be further increased by changing the diameter of the shorted subs. Figure

3 presents a static analysis for mechanical load calculation with a given material. Low-grade Stainless Steel is chosen as a comparison to Inconel 718. The acting force from the load is applied parallel to the vertical axis. Opposing forces are acting in the anchoring points in cross-sections x-x and y-y. These are the most critical points as the load has the longest distance and the smallest diameter.

To determine the maximum load in the anchor, the traditional analytical approach given in [24] is used. For a given material and safety factor, it is necessary to calculate the allowed tension inside the material. The next step is from the allowed tension and the diameter to calculate the maximum load for a given direction.

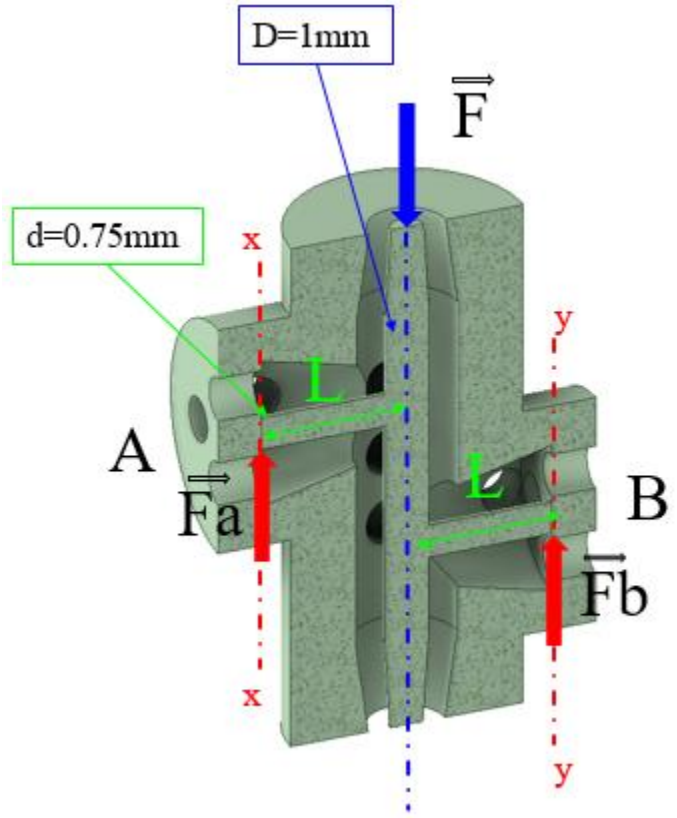


Fig. 12. Static diagram.

From the static diagram in Fig. 12, resistant forces in the shorting plane are calculated. To satisfy the static condition, all forces in a given plane must be equal to zero. Also, the sum of all "Moments" in a given plane must be equal to zero. Resistance forces are calculated from the given set of equations (Fa and Fb).

$$\sum_{i=1}^{n} \overrightarrow{Xi} = 0$$

$$\sum_{i=1}^{n} \overrightarrow{Yi} = 0$$

$$\overrightarrow{Fa} - \vec{F} + \overrightarrow{Fb} = 0 \rightarrow \overrightarrow{Fa} + \overrightarrow{Fb} = \vec{F}$$

$$\sum_{i=1}^{n} \overrightarrow{Mi} = 0$$

$$-\vec{F}L + \overrightarrow{Fb}2L = 0 \rightarrow \overrightarrow{Fb} = \frac{\vec{F}}{2}$$

$$M_{max} = \frac{LF}{2} \rightarrow F = \frac{2M_{max}}{L} \qquad (1)$$

The equation for Mmax (1) maximum load force can be calculated from the static diagram in Fig. 3. Furthermore, from the other side Mmax (2) and (3) can be calculated from the material condition. Material condition is defined from the material properties of dynamic normal stress and static normal stress conditions. Since bending is a predominant stress type, shear stress conditions can be neglected. The static and dynamic material condition is determined by ISO standardized procedure. The list of standards is in [25]. Also, as part of (2) and (3) of Mmax are coefficients Kd (sometimes labeled as Kt) [26], known as stress concertation factor, which improves the accuracy of the equation when the geometry of the component has a cross-section with different diameters, like stub diameter of 0.75mm and mainline 1mm diameter. This coefficient takes into account potential stress concentration at the plane of transition. In order to reduce the stress concentration, typically fillet is added. Depending on the filet dimension Kd coefficient is determined. The last coefficient that is used in this equation is S which is called the safety factor for shafts. The safety factor is determined for shafts from 1.5 to 2.5. This coefficient considers any hidden imperfections inside the fabricated parts that can cause fatigue or stress concentration inside the solid material [27]. Typically hidden stress concentrations are when components are fabricated in any form of 'hot"

processes such as metal 3D printing, casting, forging, etc. Typically, after any "hot" process of manufacturing heat treatment must be conducted to reduce hidden stress concentration. This process is called material normalization, and typically steel-like materials are subjected to temperatures between 870C° and 900C°. After heating, a component is gradually cooled down to room temperature [28].

In the end, the calculated load force mass m, is calculated when force is divided by gravity acceleration of 9.81m/s.

Input parameters:

- Typical low-grade stainless-steel parameters:

$$R_m = (500 - 600)\frac{N}{mm^2}$$

$$\sigma_{(-1)} = 220\frac{N}{mm^2}$$

$$\sigma_{(0)} = 350\frac{N}{mm^2}$$

- Geometrical input:

$$d = 0.75\ mm$$

$$D = 1\ mm$$

$$L = 3.3\ mm$$

$$W = \frac{d^3\pi}{32}\ Polar\ moment\ for\ circular\ cross-section.$$

- Geometrical and material input:

$$K_d = (1.5 - 2.1) for\ material\ with\ R_m < 700\frac{N}{mm^2}\ and\ for\ step\ in\ dimension\ from\ 1mm\ to\ 0.75mm$$

$$K_d = 1.5$$

- Safety factor input for a static condition:

$$S = (1.5 - 2.5)\ typicaly\ for\ shaft.\ For\ worst\ case\ scenario\ S = 1.5\ is\ chosen.$$

$$S = \frac{\sigma_{(0)}}{K_d \sigma_{static}} \rightarrow \sigma_{static} = \frac{\sigma_{(0)}}{K_d S}$$

$$S = \frac{\sigma_{(-1)}}{K_d \sigma_{dynamic}} \rightarrow \sigma_{dynamic} = \frac{\sigma_{(-1)}}{K_d S}$$

- Mechanical load calculation:

$$\sigma_{static} = \frac{M_{max}}{W} = \frac{\sigma_{(0)}}{K_d S} \rightarrow M_{max.static} = W \frac{\sigma_{(0)}}{K_d S} \quad (2)$$

$$\sigma_{dynamic} = \frac{M_{max}}{W} = \frac{\sigma_{(-1)}}{K_d S} \rightarrow M_{max.dynamic} = W \frac{\sigma_{(-1)}}{K_d S} \quad (3)$$

$$F_{static} = \frac{2M_{max.static}}{L} = 2\ N$$

$$F_{dynamic} = \frac{2M_{max.dynamic}}{L} = 1.25\ N$$

$$m_{static} = \frac{F_{static}}{g} = \frac{2}{9.81} = 0.204\ kg$$

$$m_{dynamic} = \frac{F_{static}}{g} = \frac{1.25}{9.81} = 0.127\ kg$$

From mechanical load analysis, it is calculated that for an anchor with two 0.75 mm diameter stubs and a 1 mm diameter mainline, low-grade stainless steel can sustain a load of 0.2 kg for the static material condition (2) and 0.127 kg for dynamic material condition (3).

### 2.2. Coaxial Anchor Design: Electrical Perspective

The baseline coaxial line in the anchor shown in Fig. 11 has the next higher-order mode turn-on at 57 GHz in the mainline, and in the stub line, two cross-sections are present. The first is in transition between the mainline and the stub area, where the diameter of the inner conductor is 0.75mm, and the outer diameter is 2.35mm higher-order mode turn-on after 62GHz. The second cross-section is at the end of the stub (at shorting plane) since the outer conductor has a tapered shape, the inner conductor diameter is 0.75mm, and the outer diameter is 3.45mm, which gives a next higher-order mode to turn on after 45GHz. This was found to be a sufficient safety margin to develop an anchor that works over parts of K- and Ka-bands, as desired for this

design. Considering current DMLS limitations, a single shorted quarter-wave stub can be designed to achieve about 16% bandwidth with return loss > 20 dB. By adding a second stub, we provide better mechanical support and an additional line segment for further cancellation of reflections, increasing bandwidth. Circuit simulations show that up to 2 octaves of bandwidth may be theoretically achieved. Full-wave simulations were conducted to design and study different aspects of the anchor performance, including tolerances and escape holes. Here we focus only on the escape holes.

To allow for un-sintered alloy powder to be removed from the interior of the coax, escape holes are added in the outer conductor of the coaxial anchor. Their impact can be critical for both the RF performance and the accuracy/integrity of the build. If too large, they can allow for the guided wave within the coax to leak, producing undesired self-interference and increased loss. If too small, their impact on manufacturing is insignificant and may also be damaging due to clogging. Thus, their careful design is very important. Shown in Fig. 13 and Fig. 14 are model and HFSS simulation results, respectively. Also shown in Fig. 14 is the impact on the anchor's S-parameters. Without the holes, the 11.8 mm long, the smooth anchor has a return loss > 20 dB and insertion loss < 0.15 dB over 20-39 GHz range. As seen in the same figure, the escape holes have some negative impact on the anchor's performance. For the designed device, the computed radiation losses of 1 mm, 1.1 mm, and 1.3 mm diameter holes are between 0.012dB and 0.038dB. Note that all the studies were carried out with the 2.4mm connectors in place, which also contributes to the presence of the third resonances in an ideal case. Spacing between release holes does not impact the RF performance dramatically, and the minimum wall thickness is maintained to be 0.75 mm for manufacturing purposes. The total number of escape holes is 18.

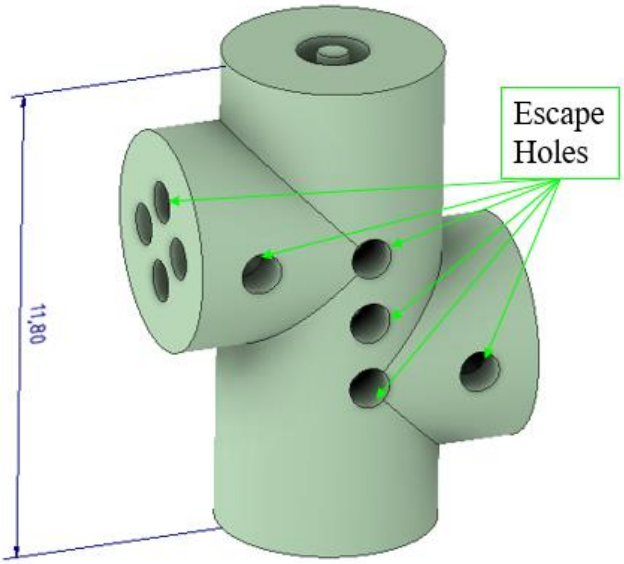


Fig. 13. The RF anchor with escape holes.

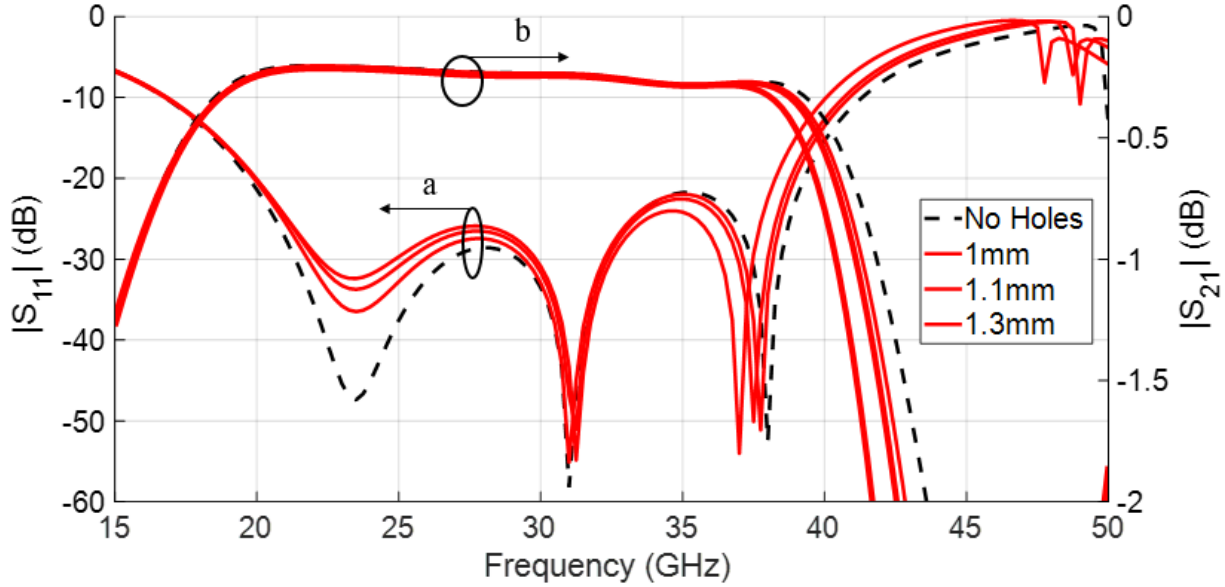


Fig. 14. Simulated effects of the escape holes on anchor's S-parameters; a) reflection coefficient, b) transmission coefficient.

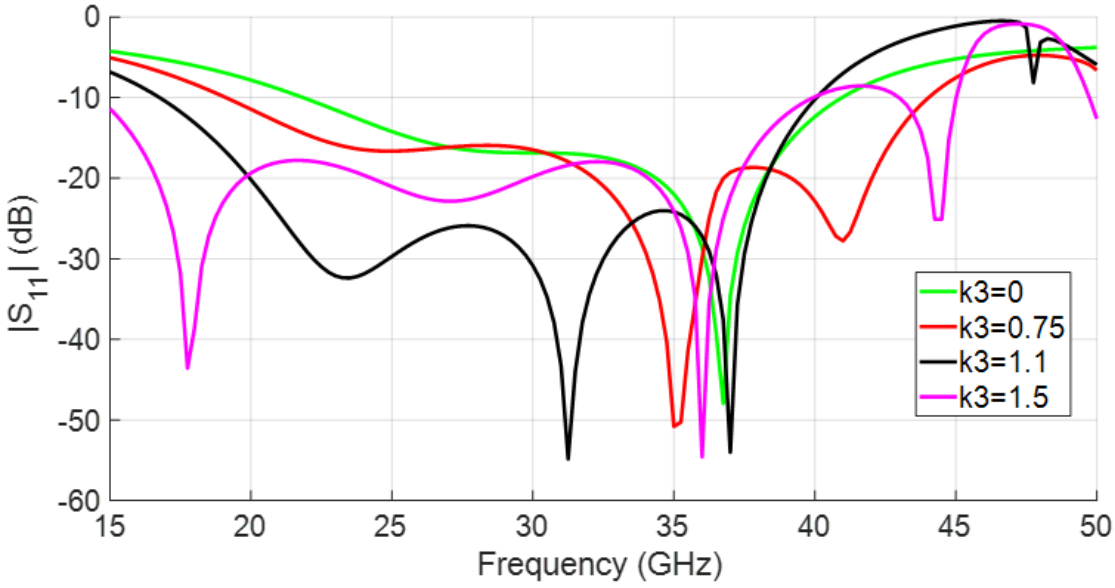


Fig. 15. Simulated effects of the different stubs spacing.

In the Fig. 15 effect of stub spacing ("k3") is presented. For k3=0, there is no spacing between stubs meaning that only one resonance is present (green line). The black line represents the stub spacing with the widest S11 < -20 dB bandwidth. The magenta line is the biggest spacing considered in this study, and it shows the resonances further separated; however, the mid-band between the resonances is not well matched.

### 2.3. Fabrication and Measurements

The anchor discussed in the previous two sections has all DMLS manufacturing guidelines carried out in the design for manufacturing (DFM) model shown in Fig. 10-a). The square flange is used to attach a 2.4 mm connector for easier post-processing alignment. Sacrificial tabs are included as additional support and insurance that the inner conductor will survive the fabrication. The minimum feature size is 0.76 mm, and the maximum aspect ratio is 4:1. Escape holes of 1 mm diameter are included, as clearly shown in the fabricated device in Fig. 16.

Fig. 16 also shows the anchor after post-processing that includes removal of (if any) trapped powder from the interior, drilling of 0.51 mm holes for connector pin

attachment, removal of sacrificial supports, and sanding of interfaces for the connector attachment. The assembly consists of soldering the connector pin and attaching the 2.4 mm connectors using four #2-56 screws. To investigate the interior of the device, the destructive inspection was conducted on a CNC milling machine with a fine step down used to ensure the inner conductor was left intact. Results indicate a solid mechanical connection, good integrity of cross-sections, and noticeable surface roughness on the walls and inner conductor (part of future studies).

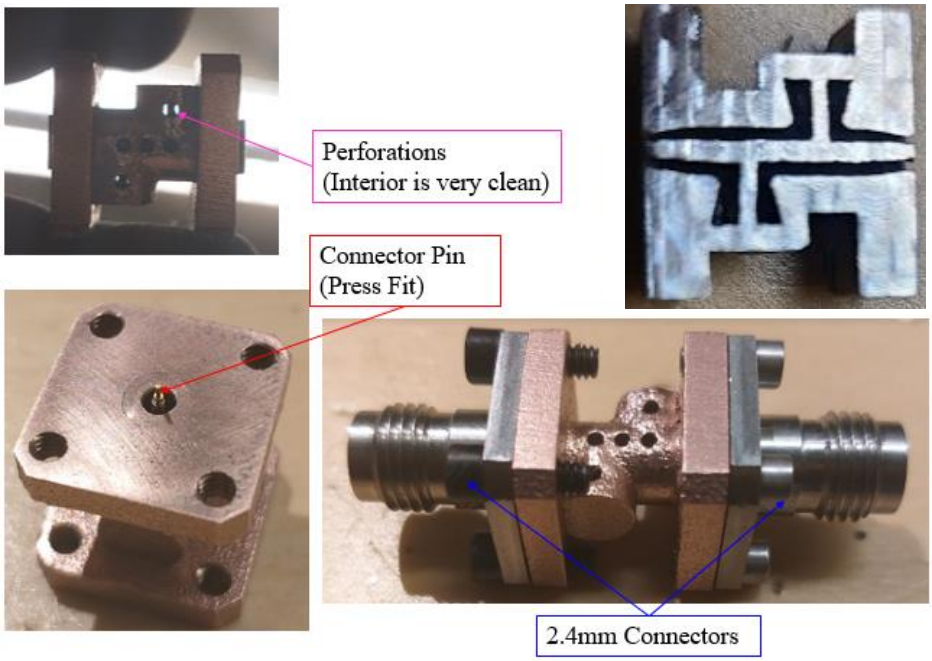


Fig. 16. Post-processing and assembling of the designed anchor. Also shown is one of the excavated models, further indicating good mechanical contact and line integrity across the length of the device.

Measured and simulated results of reflection coefficient and VSWR for the fabricated device are shown in Fig. 17 and Fig. 18, respectively. As seen, the full-wave model predicts the measured response with the main difference in loss attributed to the fabrication imperfections and effect of surface roughness. The slight shift in the resonances is attributed to the imperfections with the calibration and the contact

between the line and the 2.4mm connector. Nevertheless, the measured performance is good, with a return loss > 20dB over the 20-39GHz range. The measured insertion loss of < 0.35dB is slightly higher than what can be achieved with the same length surface micromachined recta-coax line but will/can improve with further maturing of DMLS and other 3D AM technologies. Group delay is nearly flat over the operating bandwidth. The relative bandwidth can be improved with the addition of stubs or quarter-wave sections in between them.

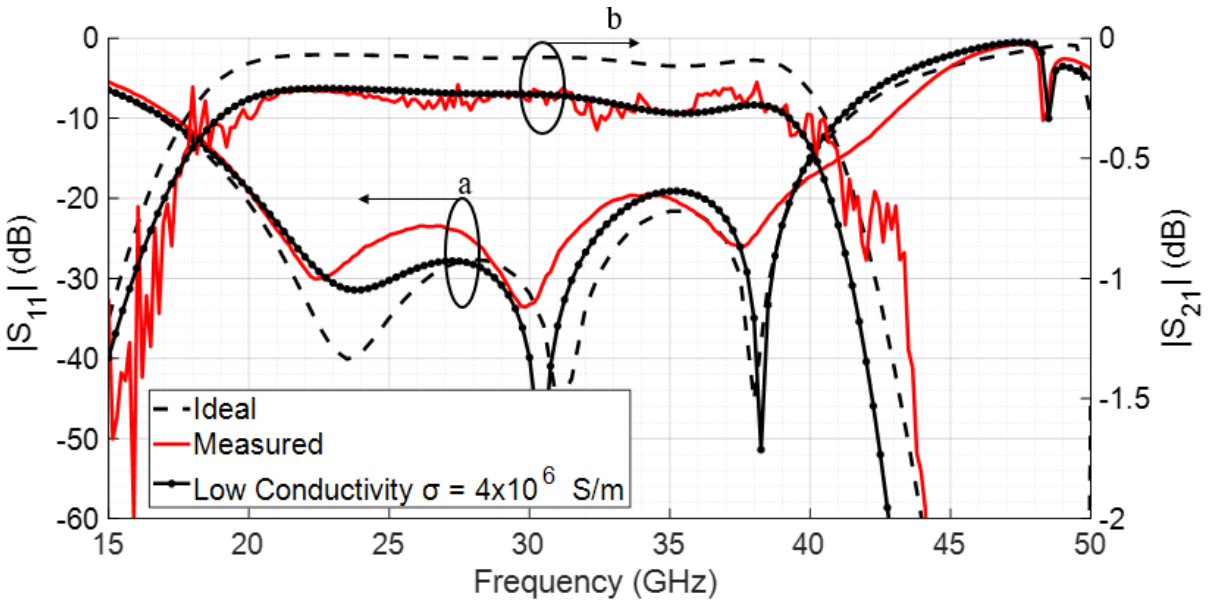


Fig. 17. Simulated and measured S-parameters of fabricated device, a) reflection coefficient, b) transmission coefficient.

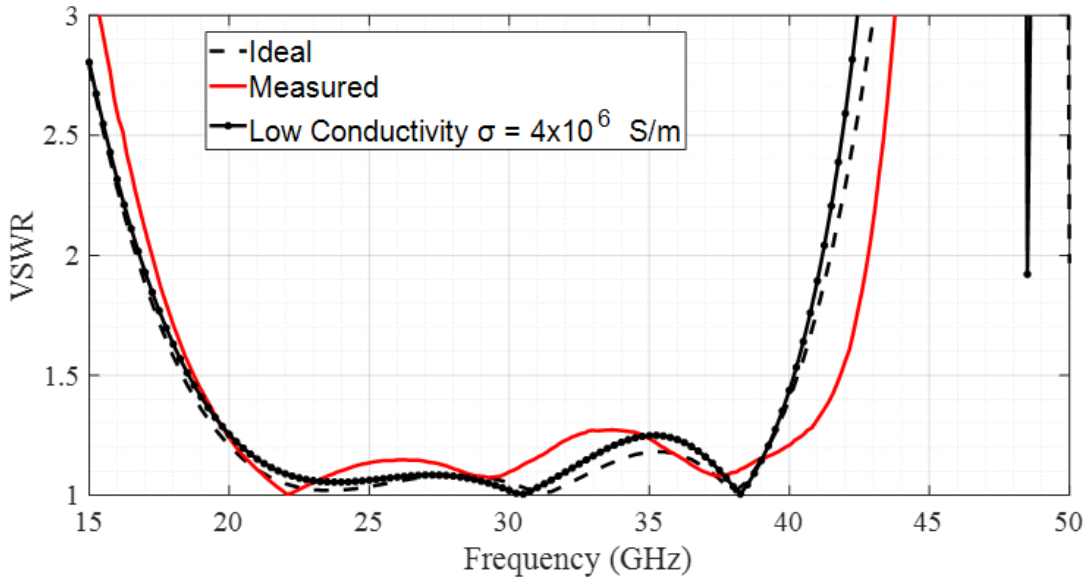


Fig. 18. Simulated and measured VSWR of the two fabricated devices.

## 2.4. Conclusion

The all-metal circular coaxial transmission line is designed for operation in K/Ka bands. The DMLS fabrication process-guided design for manufacturing yielded an 11.8 mm long line segment that works over 20-39GHz bandwidth with insertion loss < 0.35 dB and returns loss > 20 dB. The element is intended to be used as a mechanical anchor for other components and subsystems prototyped with 3D printing. Excavation and post-fabrication autopsy have shown good integrity of the device contacts and physical structure. In addition, from a mechanical perspective, it is calculated that for an anchor with two stabs, a diameter of 0.75 mm and a mainline of 1 mm in diameter, low-grade material stainless steel can sustain a load of 0.2 kg for the static material condition and 0.127 kg for dynamic material condition.

Impact of surface roughness and other imperfections, bandwidth increase, as well as integration with RF devices are all part of future studies. This work is published, and the full text is in [32].

# CHAPTER III

# DESIGN OF THE COAXIAL QUADRATURE HYBRID

## 3. Introduction

Quadrature hybrids (Fig. 19) are 3dB directional couplers with a 90˚ phase difference in the output ports (port 2 and port 3) [29]. The hybrid consists of four ports. The convention adopted has numbering ports in a clockwise direction, as indicated in Fig. 19. The impedances and line lengths are also denoted. The quaterwave length is with respect to the center design frequency. Traditionally, this hybrid type is made in a microstrip line or stripline configuration [20]. However, this method requires a multi-material configuration (substrate and copper cladding), which could be challenging for manufacturing and assembling. Additionally, substrate pricing must be considered as well.

As mentioned in Chapter I, additive manufacturing is gaining popularity in the RF industry for many different applications. This chapter introduces the coaxial quadrature hybrid designed for additive manufacturing, namely for Direct Metal Laser Sintering (DMLS).

In other work, the SLA manufacturing technique is implemented along with copper plating or liquid metal plating in [20], a branch line hybrid is presented and fabricated using SLA and metalized afterward.

Some of the benefits of DMLS compared with SLA and platting are allowing for structures to be all metal, which reduces the dielectric losses. Also, the structure is not multi-material which helps from a thermal expansion perspective. Also, due to the 3D nature of the printing technique, complex geometries are possible.

This work explores the possibility of utilizing the DMLS process for fabricating the coaxial quadrature hybrid at the 20GHz central frequency with as reduced phase and amplitude imbalances as possible.

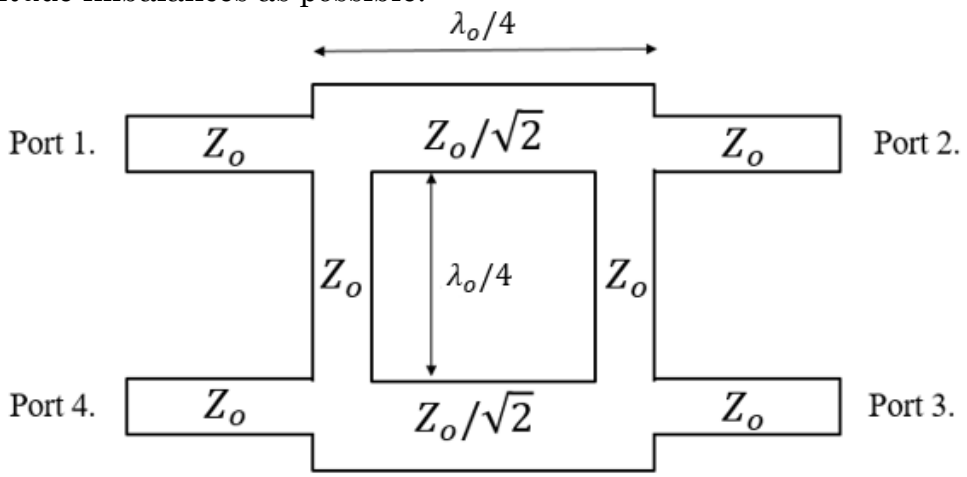


Fig. 19. The geometry of the quadrature hybrid for microstrip configuration.

### 3.1. Quadrature Coaxial Hybrid Design

The concept of the coaxial quadrature hybrid is presented in Fig. 20. The hybrid consists of the central conductor (red), outer conductor (blue), and quarter branch lines connected through a junction. The junction is designed in a "Y" geometry to better transition the two different impedances and improve fabrication. Separation of the central and outer conductor is achieved with a spacer made out of Teflon, which also serves as a mechanical anchor.

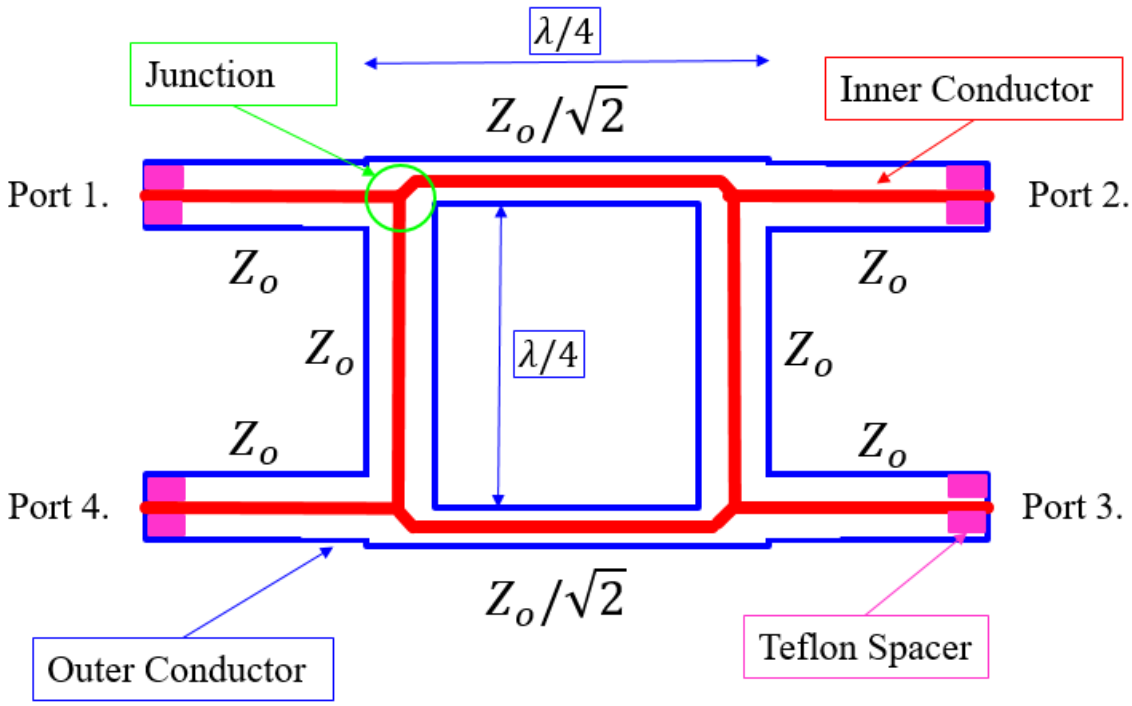


Fig. 20. Layout of the coaxial quadrature hybrid.

The EM modeling is carried out using ANSYS HFSS, and the design with the dimensions is presented in Fig. 20. The maximum dimensions of the hybrid are 12mmx12mmx11.26mm. The central conductor diameter is 0.75mm, which is the minimum feature size available in the DMLS method. The chosen central conductor has a constant diameter to improve the fabrication and $Z_o/\sqrt{2}$ impedance sections are achieved by shrinking the outer conductor diameter. The junction is modeled in a "Y" shape configuration in order to reduce the parasitic and imbalances by improving the transition between two coaxial cross-sections. The geometry has also been designed in such a way to enhance the printability when printed in the direction indicated in Fig. 21.

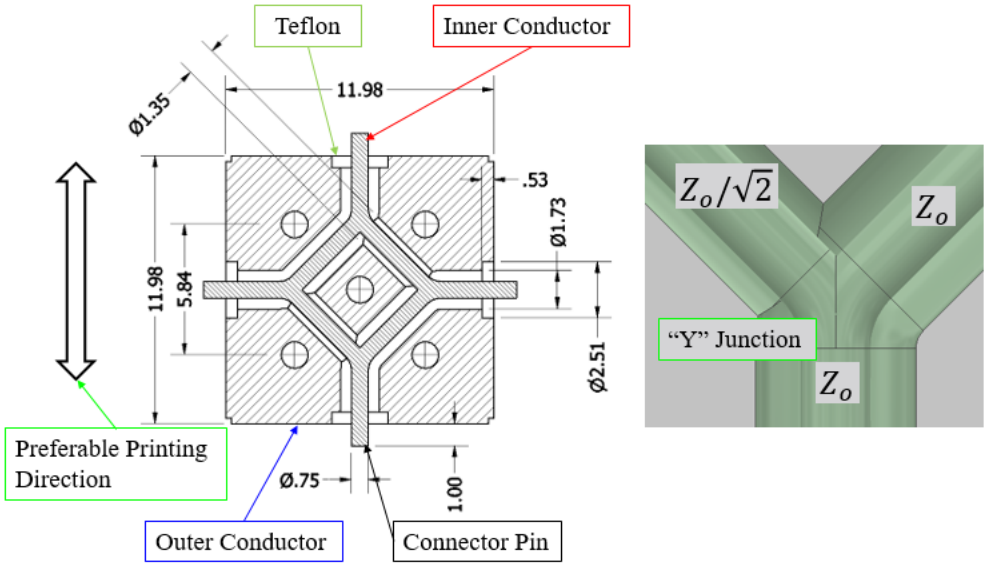


Fig. 21. Coaxial quadrature hybrid geometry.

Since the gap in $Z_o/\sqrt{2}$ impedance section is about 300 microns, and there is a high possibility of clogging. To mitigate this, an initial fabrication concept of a split block is chosen. In the split block configuration, fabrication consists of 3 parts: the two halves of the outer conductor and the central conductor. All three parts are printed separately. The split-block configuration is shown in Fig.22. Teflon supports are fabricated using CNC, and the diameter of the outer conductor has been adjusted accordingly for required impedance since Teflon is used instead of air.

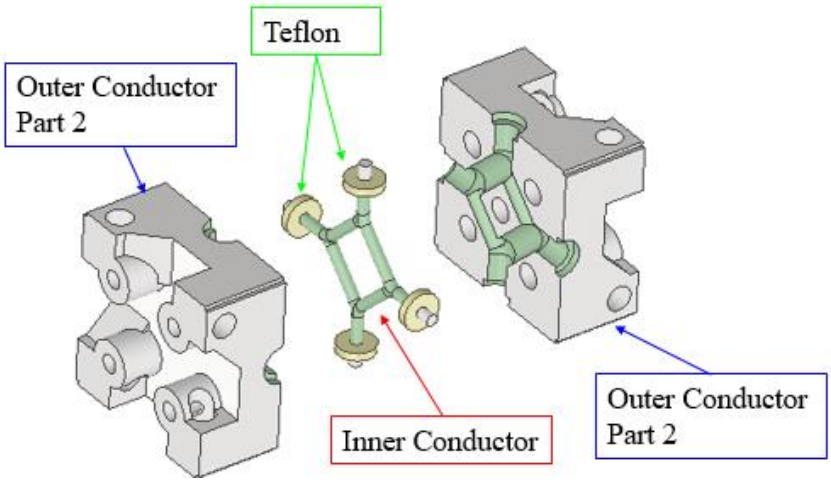


Fig. 22. Designed components in a split block configuration.

Computational results are presented in Fig. 23 to Fig. 25. The design frequency is 20GHz, and low amplitude and phase imbalances were achieved between 18.5GHz and 20.5GHz.

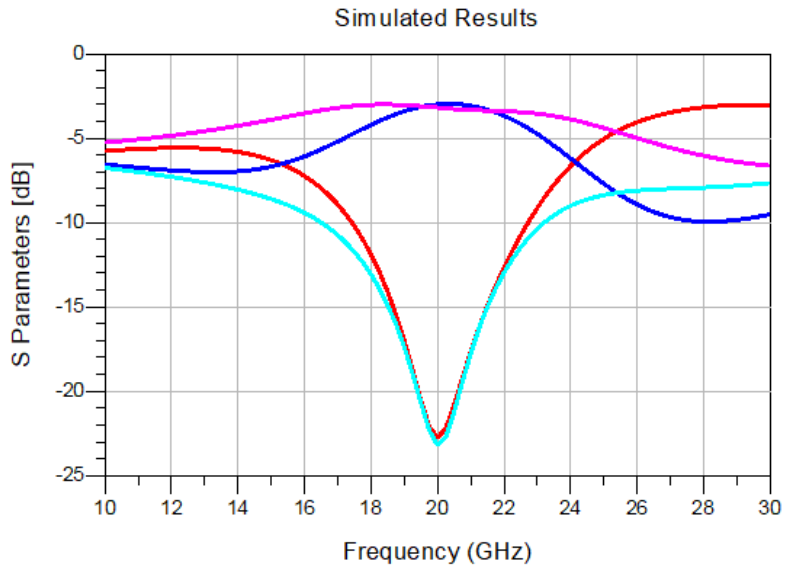


Fig. 23. S parameters simulation results.

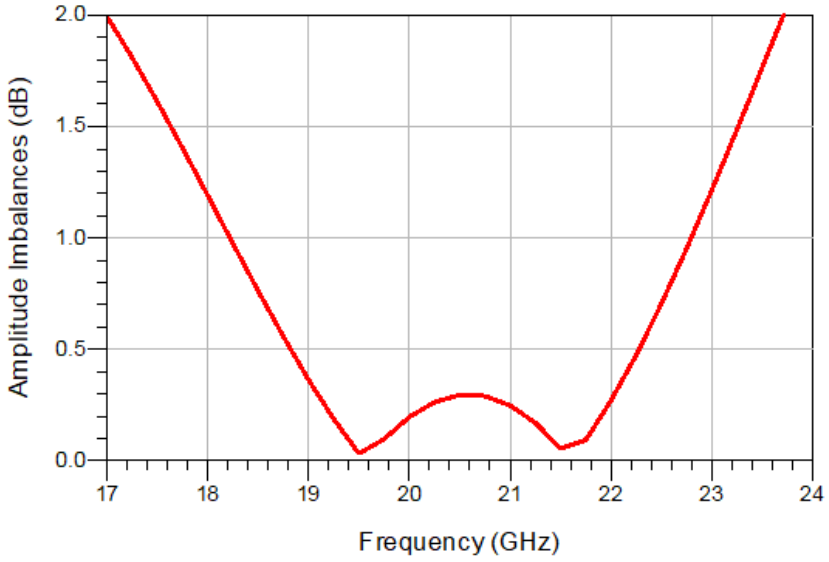


Fig. 24. Simulated results for amplitude imbalances.

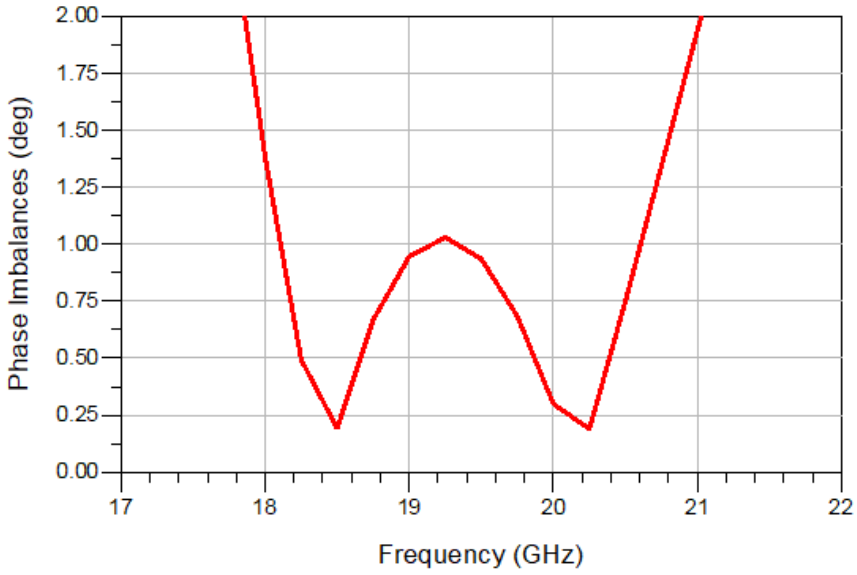


Fig. 25. Simulated results for phase imbalances.

### 3.2. Quadrature Coaxial Hybrid Fabrication and Measurements

The fabrication of the coaxial quadrature hybrid is carried out in the DMLS technique, using aluminum alloy. The printing resolution used in this fabrication is 20microns layer thickness. Fabrication was done by Protolabs [10]. In Fig. 26, fabricated components are presented: the two halves of the outer conductor (a) and (b), respectively. The central conductor is presented in Fig. 26 (c), and the marking on the right branch is used for orientation. In Fig. 26 (d), one of the channels of the outer conductor is presented where a high level of roughness and imperfections on the inner wall is observed. In Fig. 26 (e), the central conductor with Teflon inserted in one of the halves of the outer conductor is presented. The complete alignment is achieved after the second half of the outer conductor is added. Finally, in Fig. 26 (f), the fully assembled hybrid is presented with 2.4mm connectors. The four ends of the central conductor are filed in order to mate with the connector pin. Also, faces in a splitting plane of the two halves of the outer conductor are sanded in order to achieve flush contact.

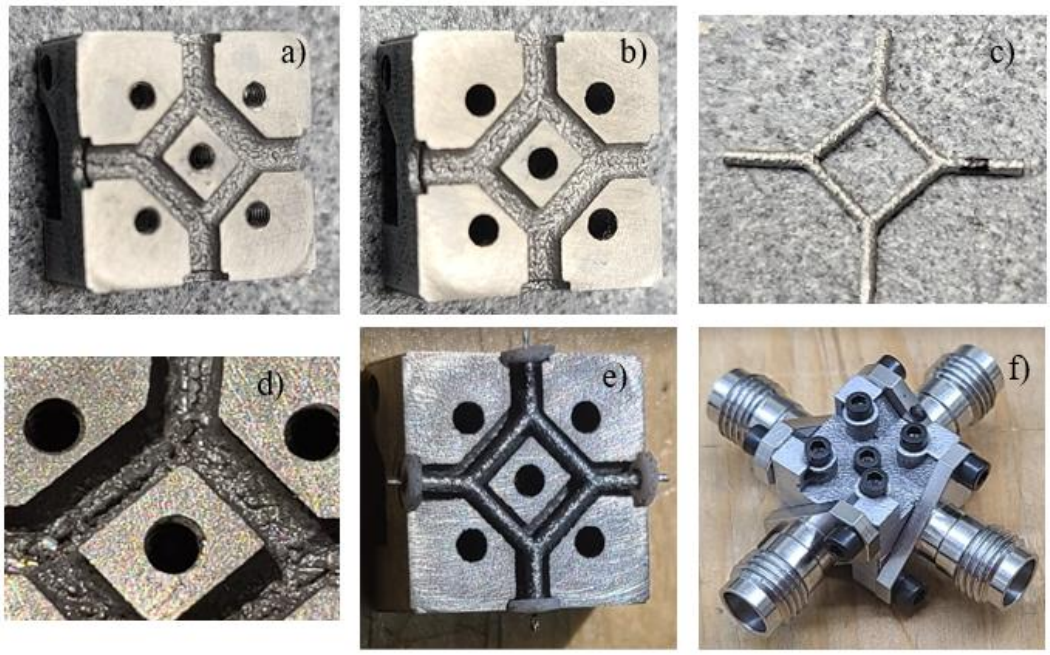


Fig. 26. Fabrication and assembly.

In Fig. 27, measured S-parameters are presented where a slight deviation is observed around the center frequency, which is likely due to a mismatch between the connector and the hybrid, mainly due to fabrication imperfections on the hybrid side. The port cross-section dimensions varied from 2.4mm (in the plane of splitting) to 2.8mm (orthogonal to a plane of splitting). The nominal is 2.51mm. Since 2.8mm was orthogonal to the plane of splitting, the issue was partially mitigated by sending the two halves. In Fig 28, measured vs. simulated amplitude imbalances are presented. Between 19.5GHz and 20.2GHz, with the imbalance around 0.5dB. From 18.5GHz to 23.2GHz, amplitude imbalances are below 1dB. In Fig. 29. Phase imbalances are presented with less than 0.3˚ imbalances observed between 18.5GHz to 20.5GHz.

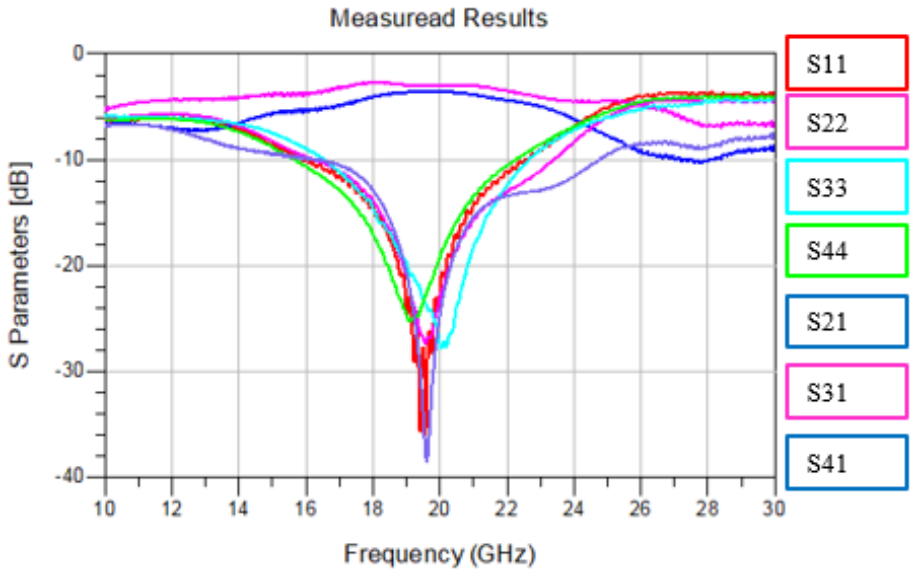


Fig. 27. Measured S parameters.

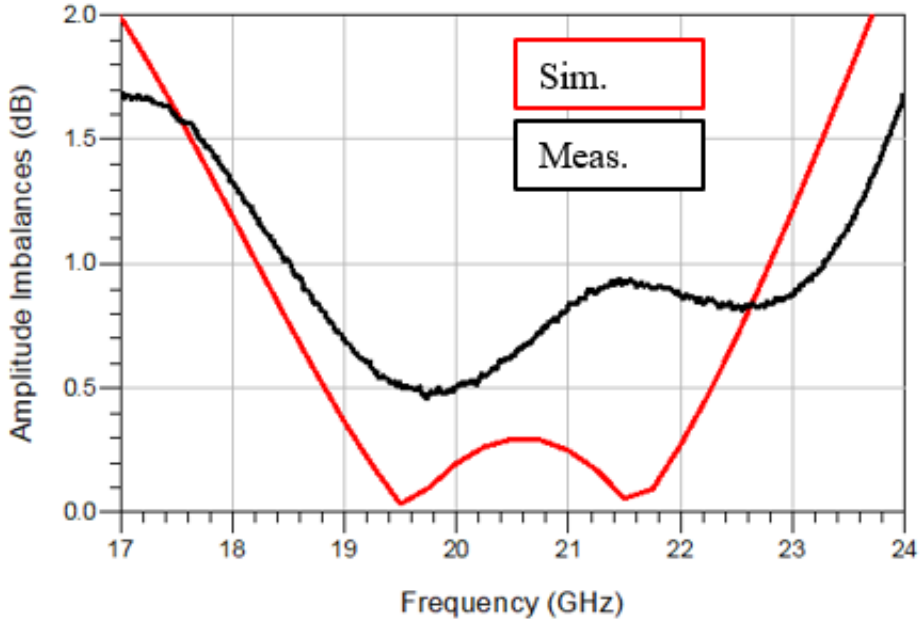


Fig. 28. Measured vs. simulated amplitude imbalances.

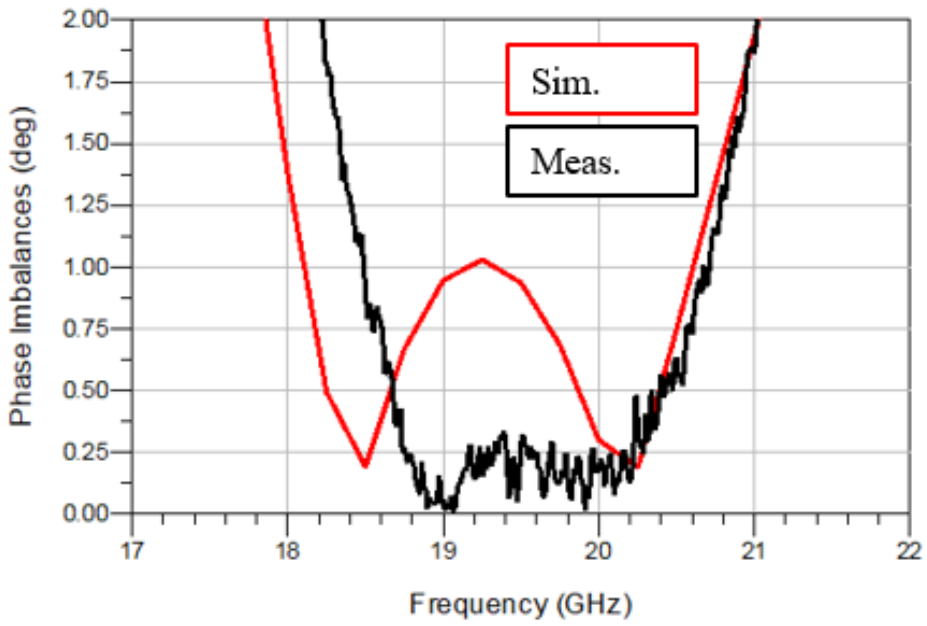


Fig. 29. Measured vs. simulated phase imbalances.

### 3.3. Conclusion

The coaxial quadrature hybrid is demonstrated in the DMLS additive manufacturing technique. The fabrication is conducted in a split block configuration, and for conectorization, 2.4mm connectors were used. From the fabrication side, the primary constraint is the minimum feature size of 0.75mm, keeping in mind the DMLS process and aluminum alloy as a material and direction of printing. The central operating frequency is 20GHz, and the amplitude and phase imbalances are less than 1dB and 0.3˚, respectively, from 18.5GHz to 20.5GHz. One of the main emphases of future work includes increasing the operating bandwidth and reducing the number of fabricated components. Ideally, monolithic fabrication is preferable.

# CHAPTER IV

# DESIGN AND CHARACTERIZATION OF A 3D PRINTED HELICAL ANTENNA MONOLITHICALLY INTEGRATED AND FED BY AN AIR-LOADED COAXIAL LINE

## 4. Introduction

This chapter demonstrates that the monolithic integration of a helical antenna [30] (with a ground plane) and a circular coaxial feed line is feasible in Direct Metal Laser Sintering (DMLS). In doing so, one can achieve good performance across a wide, instantaneous bandwidth of interest for many modern RF applications.

Helical antennas are simple and popular for many applications in both the terrestrial and space domains. Single-antenna, as well as arrayed designs operating over narrower bandwidths, have been demonstrated from VHF through microwave frequencies. A metallic conductor is wound in the form of a helix to form this antenna, as shown in Fig. 30-a. The helix is usually connected to the center conductor of a transmission line at the feed point, with the outer conductor of the line attached to the ground plane. The diameter of the ground plane should be at least $3\lambda/4$ [31]. Sometimes, the ground plane is shaped in the form of a cylindrical cavity. In this paper, a flat, circular ground plane is considered.

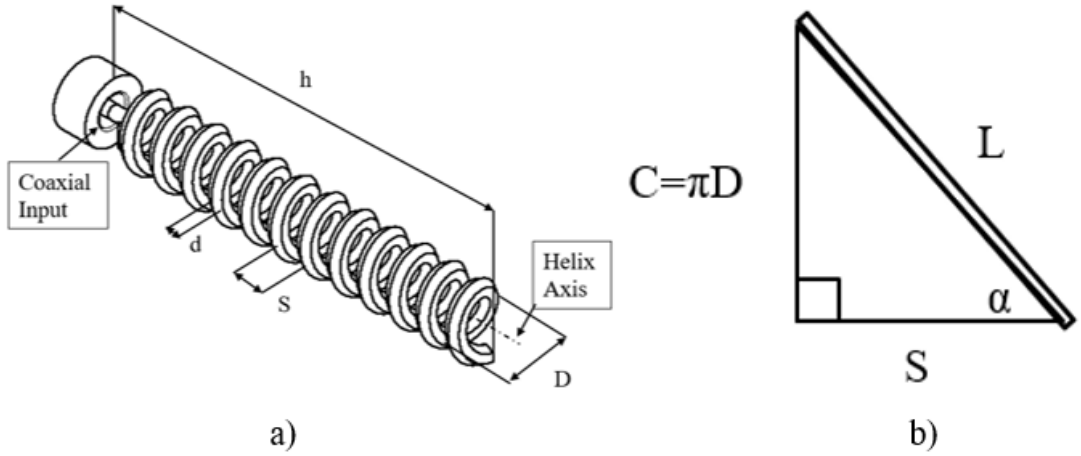


Fig. 30. Helical antenna configuration (a), and illustration of helix parameters (b).

The geometrical configuration usually consists of N turns with turn diameter D, and turn spacing S. The total length of the antenna is $L = NS$ while the total length of the wire is $L_n = N\sqrt{S^2 + C^2}$ where C is the circumference of the helix; $C = \pi D$. Another important parameter is the pitch angle α, which is the angle formed by a line tangent to the helix and a plane perpendicular to the helix axis; $\alpha = tan^{-1}\left(\frac{S}{\pi D}\right)$. The case of $\alpha = 0^{\circ}$ corresponds to no turn spacing (flat winding), and the helix reduces to a loop. On the other hand, when $\alpha = 90^{\circ}$, then a helix becomes a linear wire. When $0^{\circ} < \alpha < 90^{\circ}$, then a true helix is formed with a circumference greater than zero but less than the circumference of when the helix is reduced to a loop [31]. Fundamental helix parameters are presented in Fig. 30-b. The radiation characteristics of the antenna can be varied by controlling the size of its geometrical properties compared to the wavelength. Input impedance is critically dependent upon the pitch angle and the size of the conducting wire, especially near the feed point, and it can be adjusted by controlling their values. The general polarization of the antenna is elliptical. The helical antenna can operate in two primary modes of operation: the normal mode and the axial mode [30,31]. Whereas the former is often used to achieve an electrically small antenna, the latter is deployed for more conventional use in satellite communications. To excite the axial mode (operation mode for this paper) and achieve

circular polarization in the main lobe, the circumference, C, of the antenna must be $\frac{3}{4} < \frac{C}{\lambda_o} < \frac{4}{3}$ , [5] whereas the pitch angle is $11^o < \alpha < 12^o$. Helical antennas are often directly connectorized to conventional SMA or N-type connectors, followed by a coaxial transmission line. The coaxial line offers some desirable features for RF applications, including wideband single TEM mode operation, low loss and dispersion, dense packaging with low self-interference, and a wealth of designs for compatible components. In recent years, the monolithic integration of coaxial lines and corresponding components has been demonstrated using surface micromachining [18], [19]. One such process, PolyStrata [18], can achieve a high level of monolithic integration around a nearly air-loaded rectangular coaxial line. High accuracy, low roughness, and a wafer-scale monolithic integration of 4 and more coaxial layers are demonstrated. However, technologies like this are not widely available and, therefore, are expensive for prototyping and research purposes. This work shows that 3D printing is a good alternative for the fast development of functional coaxial prototypes.

This chapter introduces a helical antenna whose filament is supported by a short piece of air-loaded circular cross-section coaxial line, previously demonstrated in Chapter 2 and integrated with the ground plane. The helix, ground plane, and air-loaded coax are all designed for single-piece manufacturing in DMLS. The designed coaxial line can be used as an integral part of more complex RF systems and therefore is termed a "coaxial anchor."

### 4.1. Helical Antenna Design

This section explores a helical antenna design (with additive manufacturing in mind) and its potential for the n258 band (24.25 - 27.5GHz) and beyond.

Initially, a stand-alone antenna was modeled on a ground plane. In order to increase the bandwidth of the antenna, the wire diameter was increased, and study

results are presented in Fig. 31, where the solid black line is the 1mm diameter also suitable for fabrication and helps the antenna performance.

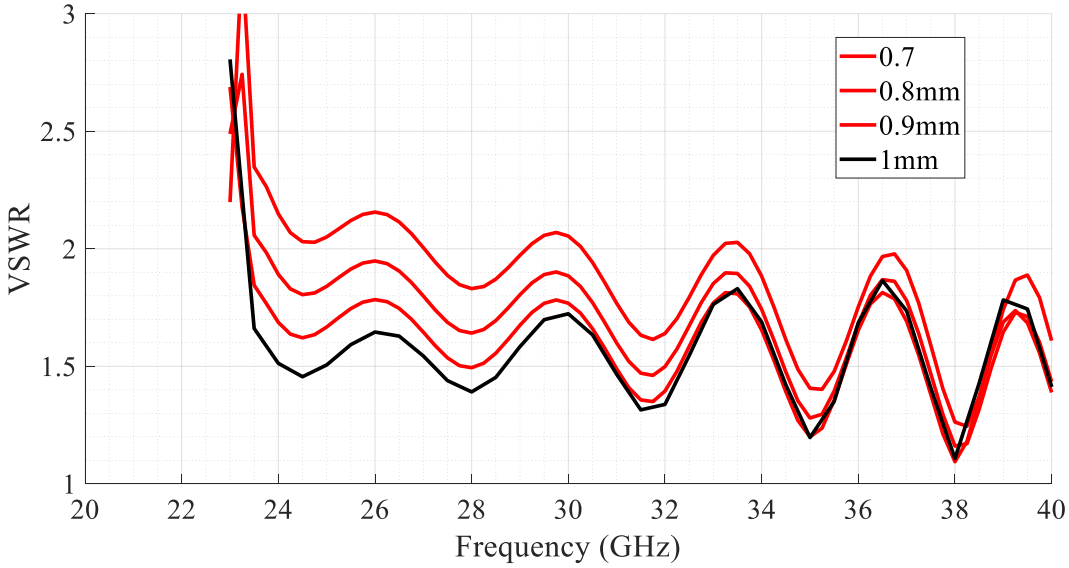


Fig. 31. Helical antenna diameter impact on a bandwidth.

In the next step of the design process, the previously discussed coaxial anchor (used as a mechanical support and an integral RF constituent (see Fig. 32) is integrated with the circular ground plane and the antenna. The antenna parameters shown in Table 5 lead to ANSYS HFSS obtained results presented in Fig. 33 to Fig. 39. With respect to the impedance match, the antenna works well over the desired band. It is noted that when compared with the stand-alone antenna, the upper portion of the band is reduced, mainly due to the operational range of the coaxial anchor. Far-field results indicate adequate performance over the same range.

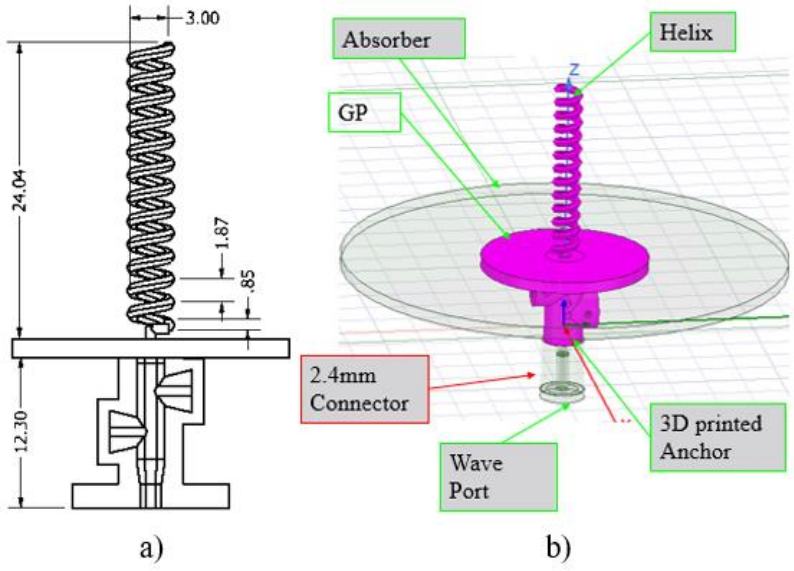


Fig. 32. A cross-section of the designed helical antenna with an integrated coaxial anchor (a), Simulation setup in ANSYS HFSS with annotated structural parts of this system (b).

TABLE 5.
Parameters of the Helical Antenna with Integrated Coaxial Anchor.

| Parameter | Value |
|---|---|
| Helix Circumference<br>$\frac{3}{4} < \frac{C}{\lambda_o} < \frac{4}{3}$ | C=9.42mm<br>0.75<0.86<1.33 |
| Helix Diameter | D=3mm |
| Spacing | S=1.87mm |
| Pitch Angle<br>$11^o < \alpha < 12^o$ | α=11.23˚ |
| Turn Length | Lo=9.6mm |
| Number of Turns | N=12 |
| Helix Height | H=24mm |
| Conductor Diameter | 2a=0.85mm |

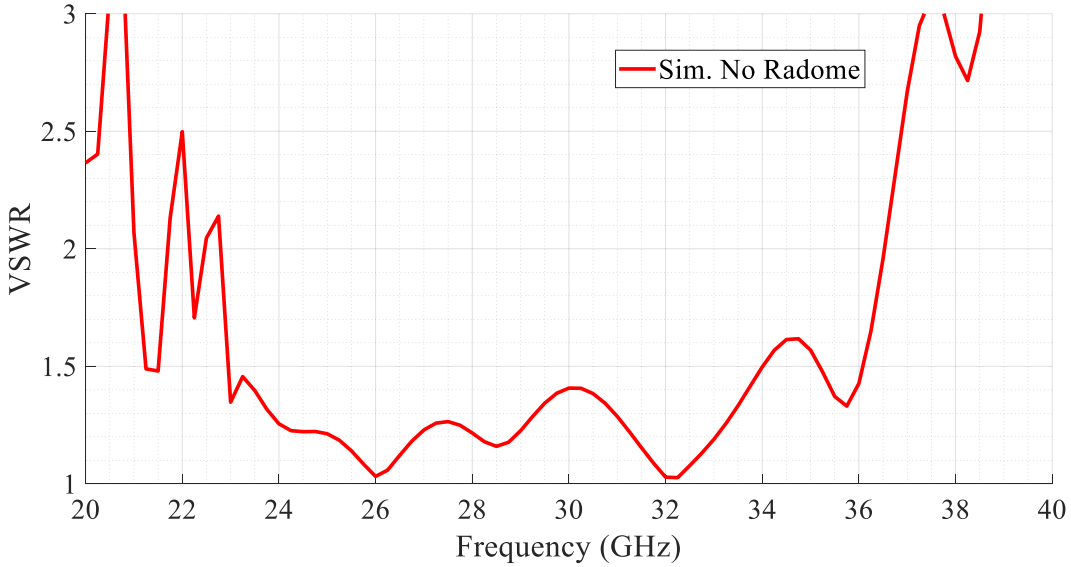


Fig. 33. Simulated VSWR for antenna with integrated coaxial feed.

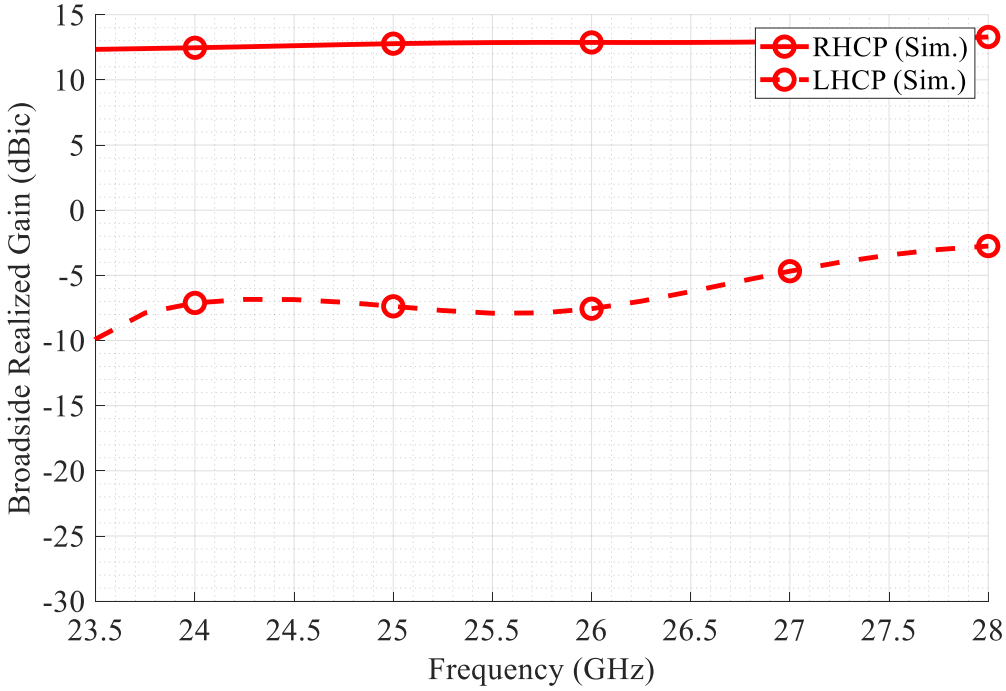


Fig. 34. Broadside realized co- and cross-polarized gains.

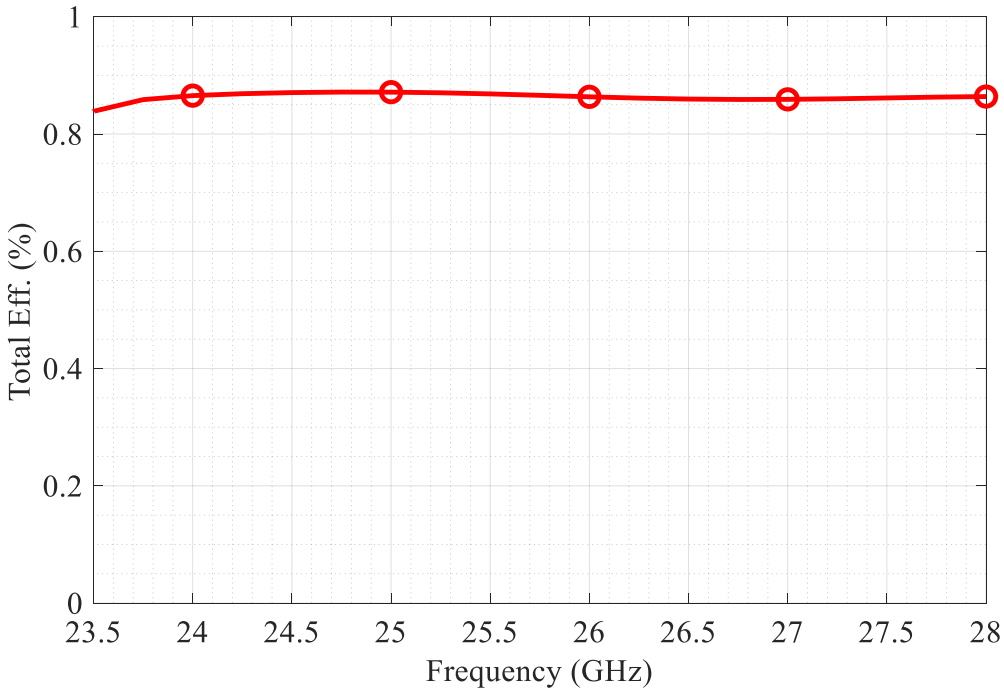


Fig. 35. Total efficiency.

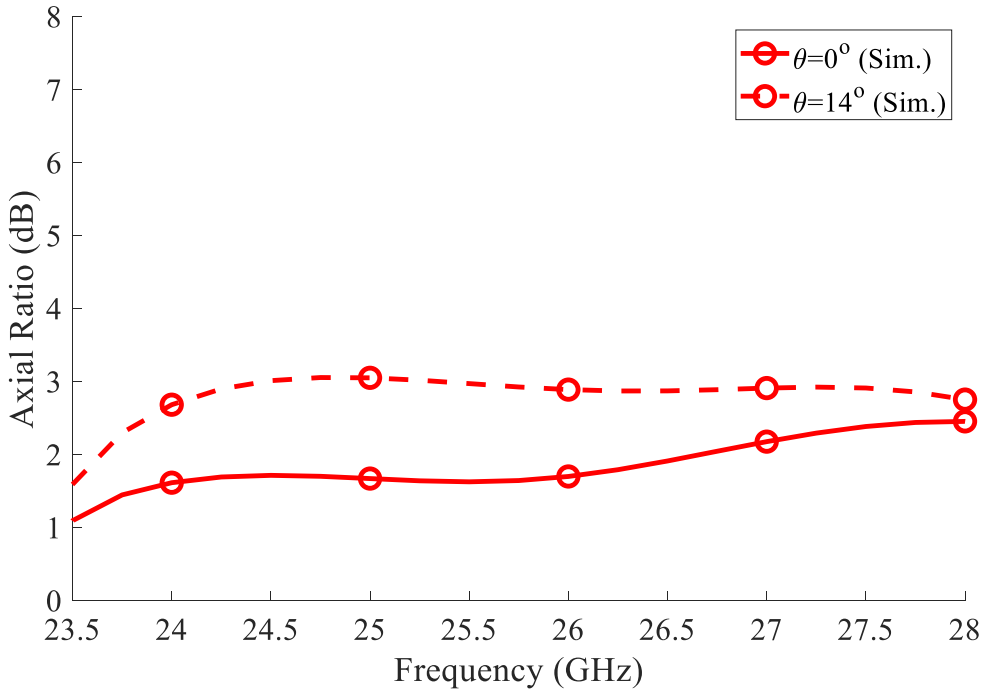


Fig. 36. Axial ratio at broadside. The designed elevation cone for this antenna is 14°.

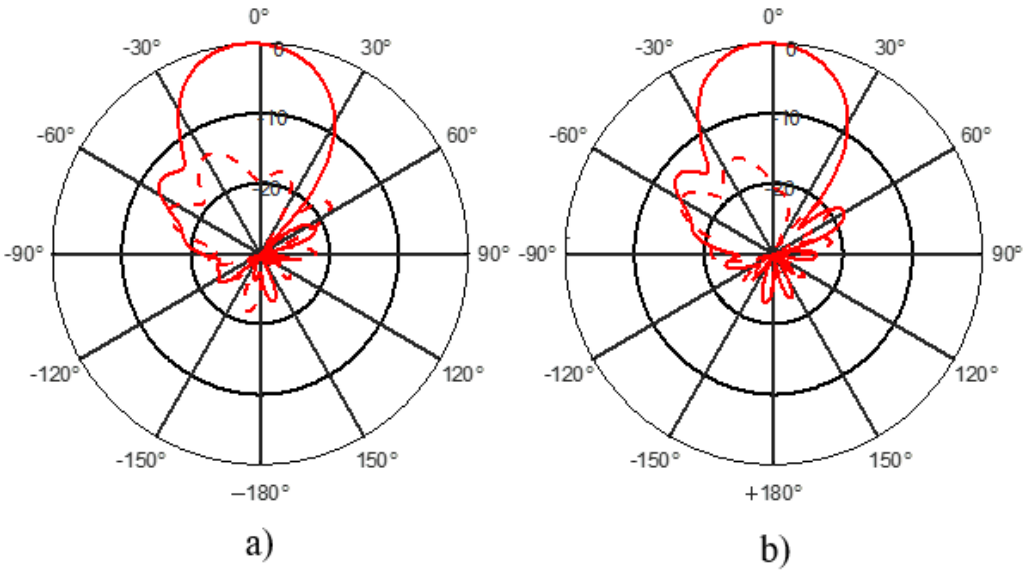


Fig. 37. Normalized radiation patterns at 24GHz (a), 25GHz (b).

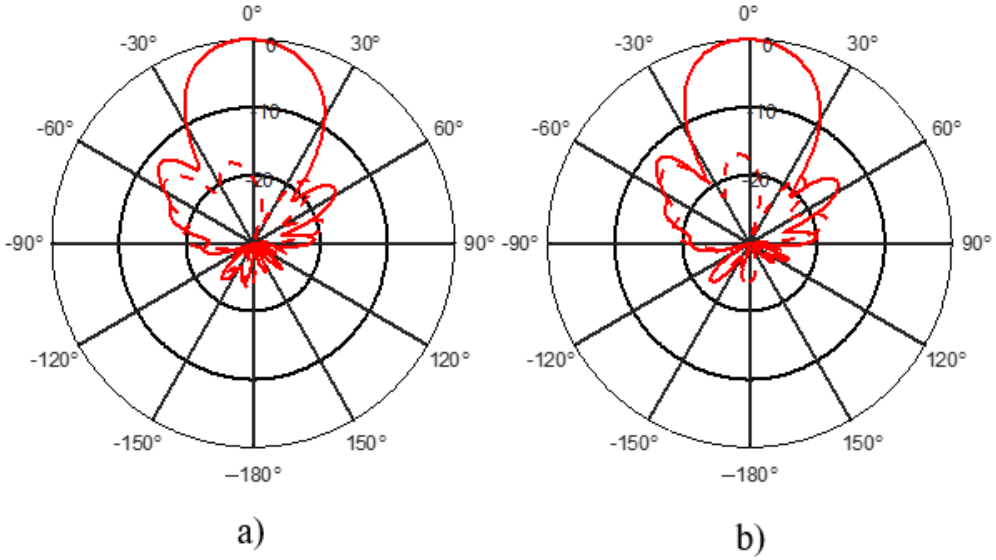


Fig. 38. Normalized radiation patterns at 26GHz (a), 27GHz (b).

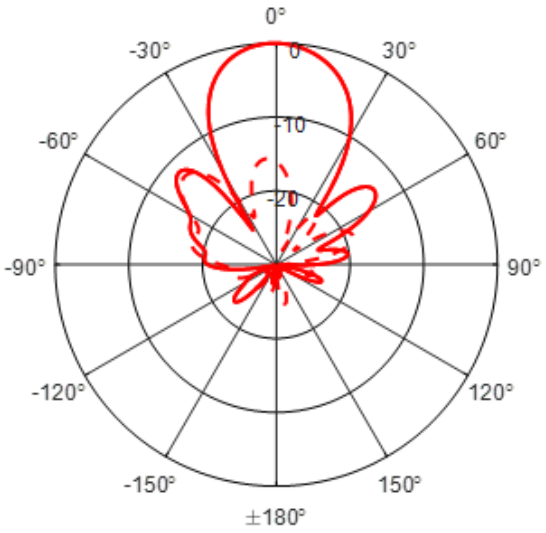


Fig. 39. Normalized radiation patterns at 28GHz.

### 4.2. Helical Antenna with Integrated Coaxial Anchor: Fabrication and Measurements

The designs are fabricated in SLA and DMLS processes, as shown in Fig 40. and Fig. 41, respectively. SLA articles are printed with the Form 3 Printer in Tough V5 resin [7] available from the printer manufacturer, Formlabs. After printing, parts are subjected to cleaning in 99% isopropyl alcohol for 20 minutes in four, 5-minute intervals. Between the cleaning cycles, alcohol was injected into the internal cavities of the coaxial anchor to ensure the uncured resin was fully evacuated. After 60 minutes of preheating to 60℃, the UV curing was carried out for 60 minutes. The copper plating of the SLA devices is outsourced to a third-party company. The SLA printing was used as proof of concept for fabrication. Since the fabrication was reasonably accurate from a mechanical perspective, the next step was to fabricate the same device in the DMLS process in order to assess RF performances as well.

Measured and simulated VSWR results are shown in Fig. 42. and the DMLS fabricated device (in Inconel 718) agrees well with simulations.

Fig. 40. Helical antenna proof of concept fabrication in SLA process.

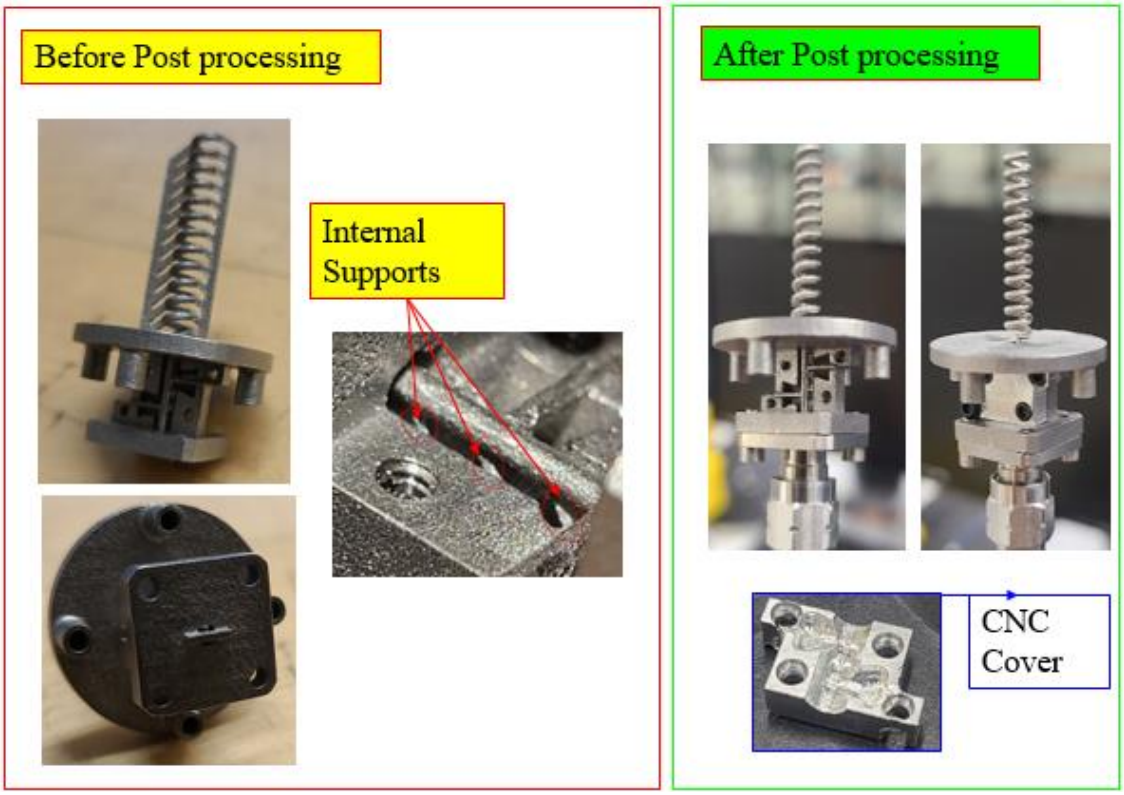


Fig. 41. Helical antenna as fabricated in DMLS and deployed post-processing steps.

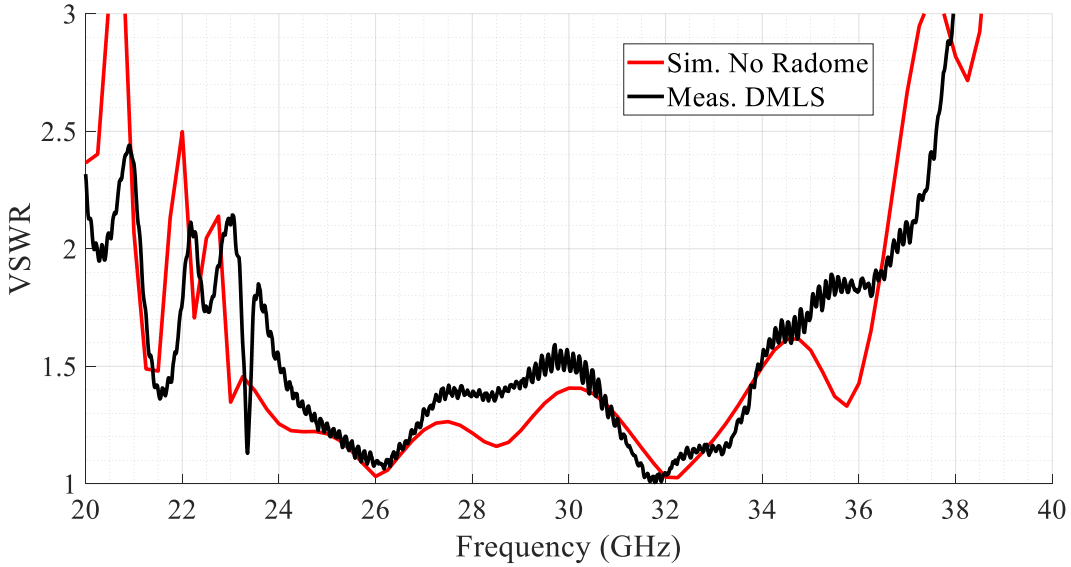


Fig. 42. VSWR results. Redline simulation, solid black DMLS, and black dashed SLA measurements results.

The pattern measurement setup is shown in Fig. 43. To mitigate the scattering effect from the mount, an absorber is placed around the ground plane. The far-field results plotted with simulations are shown in Fig. 44-49, indicating good agreement with the simulation. Lower radiation efficiency is expected due to both Inconel's ohmic losses and the proximity of the absorber. The latter contributes to a slightly better axial ratio.

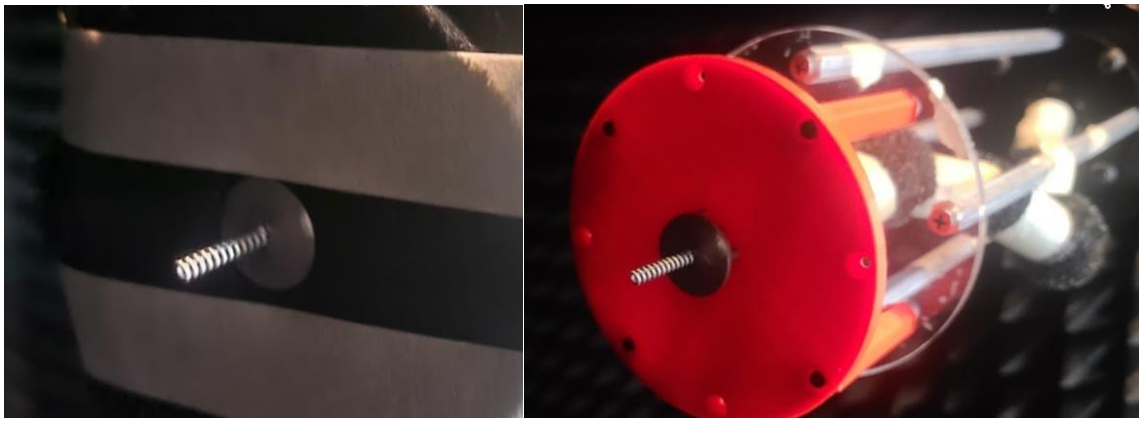

Fig. 43. Photographs of the antenna inside the chamber with the absorber placed around it (left) and without absorber (right).

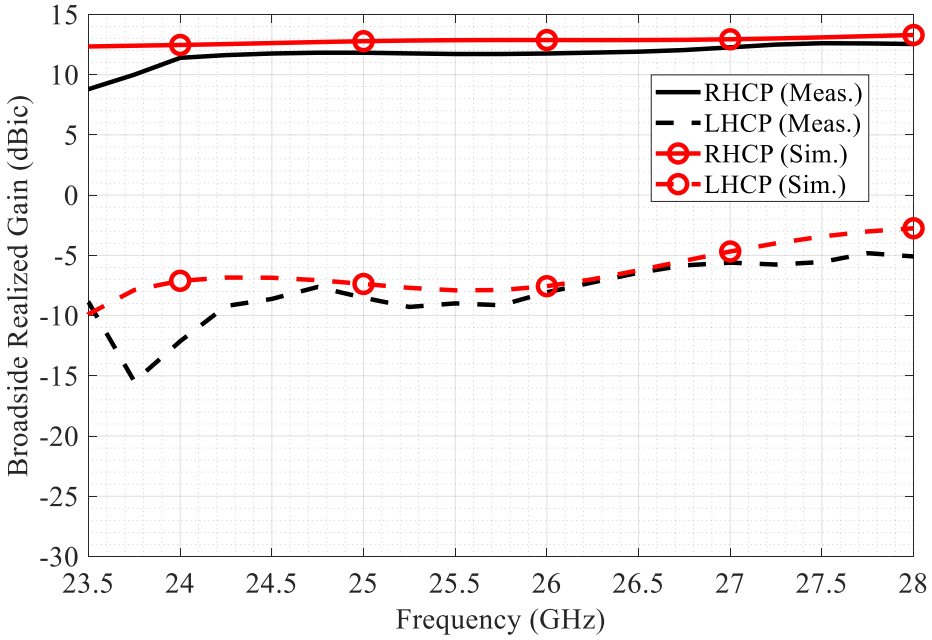


Fig. 44. Measured and simulated broadside (co- and cross-polarized) gains.

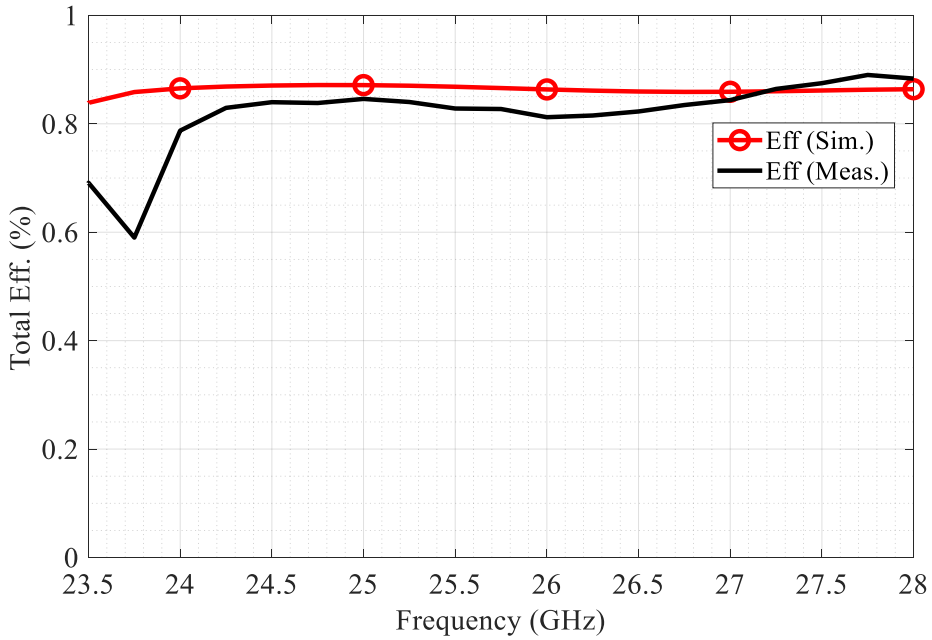


Fig. 45. Measured and simulated efficiency (taken as the ratio of realized gain and directivity).

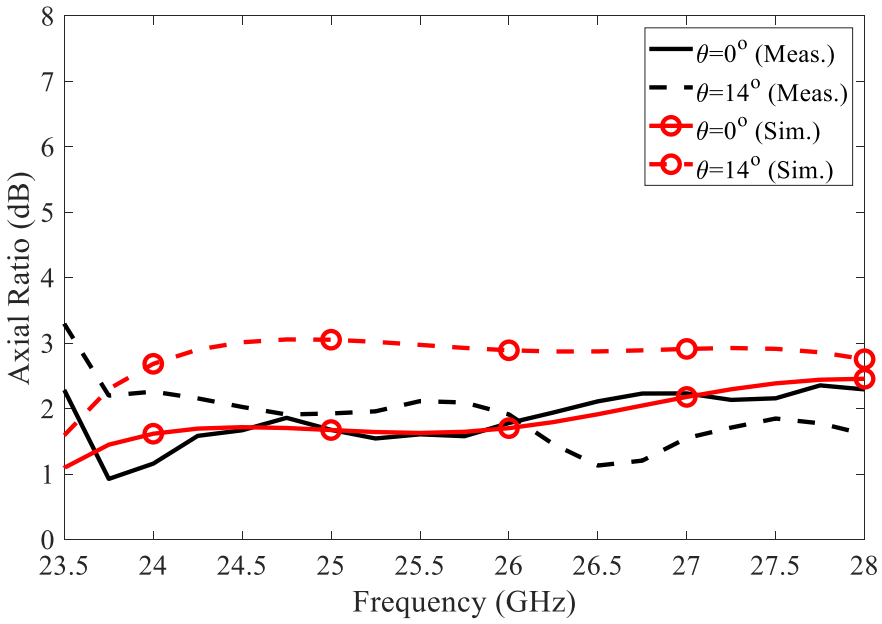


Fig. 46. Measured and simulated axial ratios at broadside and 14° elevation.

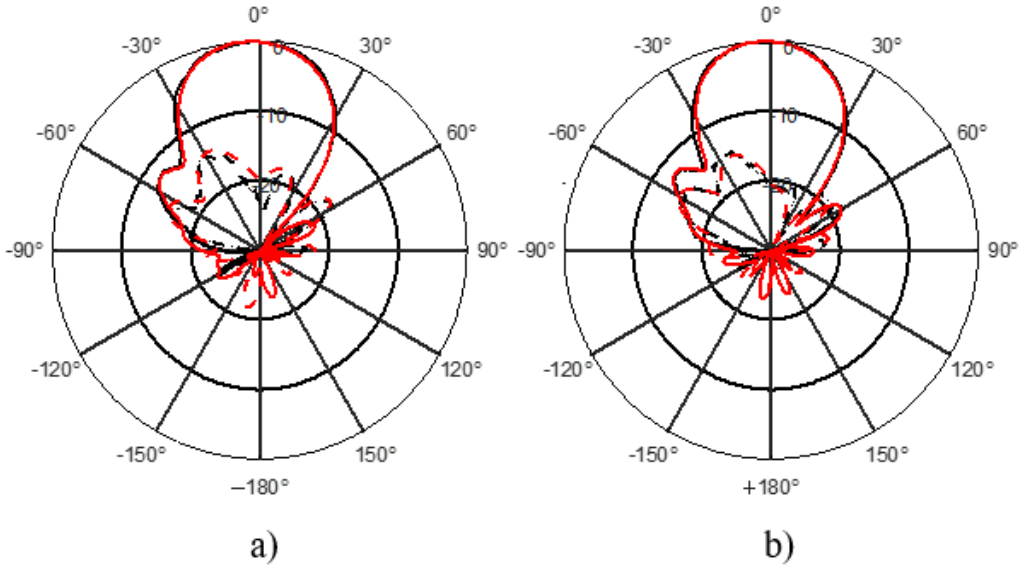


Fig. 47. Measured and simulated radiation patterns at 24GHz (a), 25GHz (b)

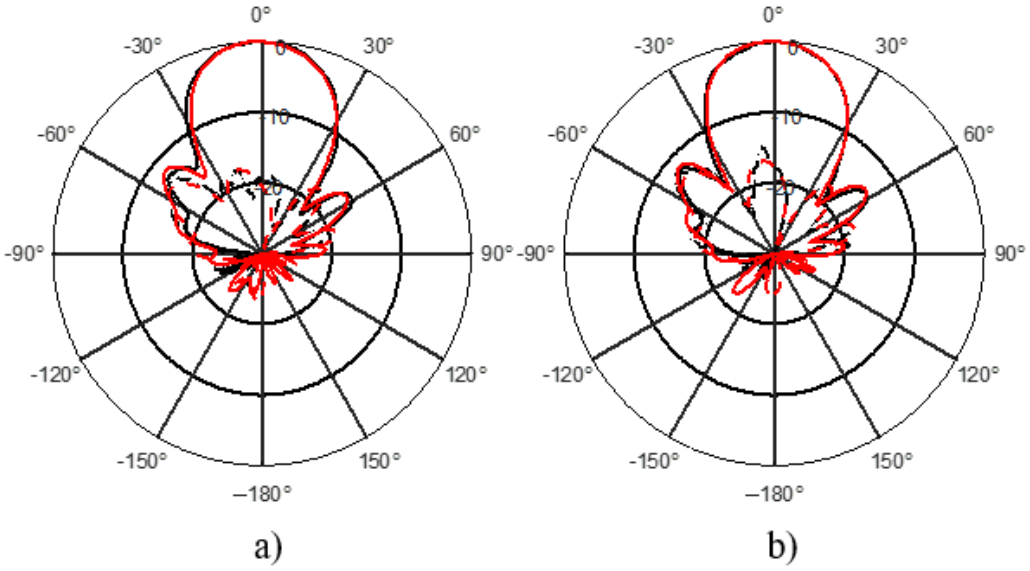


Fig. 48. Measured and simulated radiation patterns at 26GHz (a), 27GHz (b)

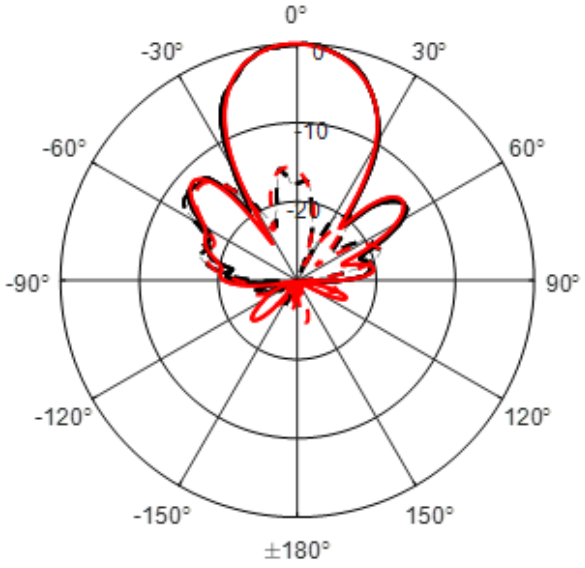


Fig. 49. Measured and simulated radiation patterns at 28GHz.

## 4.3. Conclusion

A helical antenna with integrated circular coaxial transmission line anchoring support and the ground plane is designed for operation in K/Ka bands. The design for manufacturing in present-day additive manufacturing processes, specifically Direct Metal Laser Sintering and Stereolithography, is carried out. A 36.3mm tall antenna system that works over 23.5-28GHz bandwidth is demonstrated. Post-processing steps are discussed for both processes. The successful experimental demonstration of

impedance and pattern measurements showcases the suitability of all-metal additive manufacturing for prototyping devices of this and similar kinds. Improvement in Stereolithography fabrication design will be part of future works. This chapter is published in [33].

# CHAPTER V

# 3D PRINTED RADOME DESIGN FOR MILLIMETER-WAVE HELICAL ANTENNA AND ENVIRONMENTAL TESTING

## 5. Introduction

Antennas on airborne platforms are subject to harsh environmental conditions such as rain and hail as well as a wide range of pressure and temperature conditions. This chapter proposes an improvement on the helical antenna system in [33] by enclosing the antenna with a radome tuned for both the SLA/FDM printing process and its RF performance to enhance the antenna's environmental protection. A low-cost thermal/pressure tabletop chamber is developed for antenna system testing in different environmental scenarios. The helical antenna's specific geometry makes it difficult to include the radome with minimum effect on antenna radiation parameters. This is accentuated when material diversity is limited. Some of the fabrication parameters and limitations for DMLS and SLA are shown in Table 6.

TABLE 6.

DMLS and SLA Parameters [4].

| Typical DMLS parameters | | Typical SLA parameters |
|---|---|---|
| Tolerances | +/-0.076mm plus 0.001 per each mm | +/-0.05mm plus 0.001 per each mm |
| Layer thickness | 20 to 30µm | 50 to 100µm |
| Minimum feature size | 0.75mm | 0.5mm |
| Material | Inconel 718 | Formlabs resin tough V5 (dk=2.6 and tanδ=0.025) |

The material properties of SLA Formlabs resin listed in Table 6 represent the assumed (given) values. Later in the chapter, measurements will determine the

validity of those values. Helical antennas are simple and popular for many terrestrial and space applications [30]. Stand-alone configurations and arrayed designs, operating over narrower bandwidths, have been demonstrated from VHF through microwave frequencies. The helix is usually connected to the center conductor of a transmission line at the feed point, with the outer conductor of the line attached to the ground plane. The basic parameters of the helical antenna considered in this paper are presented in Table II [30]. The helical antenna covers the frequency from 23.5GHz to 28GHz and is therefore of interest for many contemporary applications, such as 5G communications. Moreover, this work will present antenna performance on a broader frequency band up to 32 GHz.

TABLE 7.

Helical Antenna Parameters

| Parameter | Value |
|---|---|
| Helix Circumference, C | 9.42 mm |
| Helix Diameter, D | 3 mm |
| Turn Length, L0 | 9.6 mm |
| Helix Hight, H | 24 mm |
| Number of Turns, N | 12 |
| Conductor Diameter, 2a | 0.85 mm |

For antennas operating in harsh conditions, radomes are often used for their protection. However, the presence of dielectric material in the nearfield of the antenna can distort the radiation patterns, introduce reflections at the antenna input port, and yield additional ohmic losses. This motivates the adoption of thin radomes. However, the thin monolithic radome structure may cause potential mechanical instability [35]. To address this, sandwich radomes are often considered since they have broader bandwidth and a higher strength-to-weight ratio [34]. These structures rely on a unique fabrication process with correspondingly increased cost, thickness, and manufacturing time. This paper considers a monolithic 3D printed radome

advantageous for fabrication and cost considerations with minimal impact on antenna performances.

### 5.1. Radome Design and Results

The design of the radome is carried out in the context of a baseline fabricated-and-tested helical antenna with an integrated coaxial feeding network (coaxial anchor). The antenna system is connectorized with a 2.4mm connector made from Inconel 718. The material used for the radome study is Formlabs Tough Resin V5, with properties are given in Table I. The antenna and radome final geometry are shown in Fig. 50. The cylindrical shape was selected as a base geometry that naturally conforms around the helical antenna. However, studies show that tapered sidewalls significantly reduce the radome's impact on antenna performance, with a top diameter of about 1.7 times the bottom diameter for a given height of 25mm. The top thickness is constrained by the minimum dimension achievable for an in-house available Formlabs Form 3 SLA printer [7]. The system's overall dimensions are presented in Fig. 50. The modeled permittivity of the material is 2.6, with a loss tangent of 0.025.

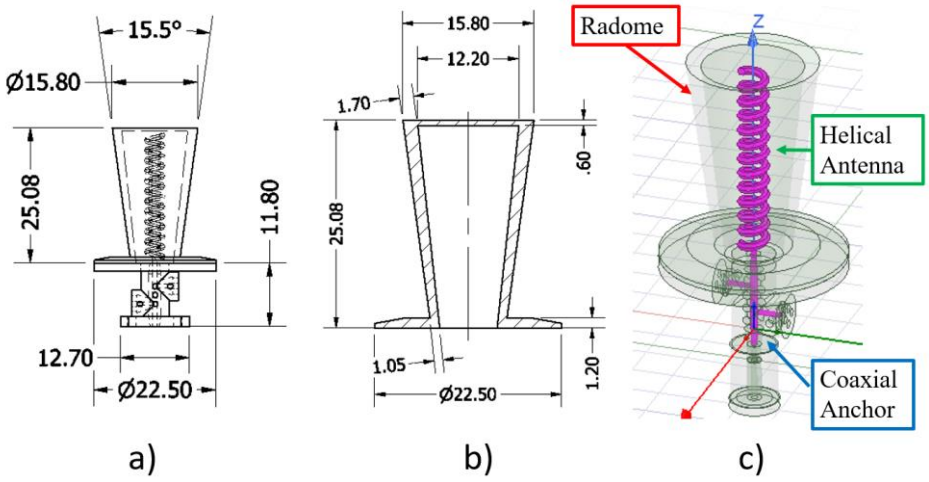


Fig. 50. Helical antenna with integrated coaxial line and radome (a), Radome dimensions (b), Helical antenna computational model (c). Dimensions in mm.

The analysis is conducted in Ansys HFSS full-wave solver, and VSWR results are presented in Fig. 51. The baseline (radome-less) antenna is also simulated, and good agreement with simulations is obtained. As seen, the addition of the radome does not induce a significant change in the impedance match of the antenna.

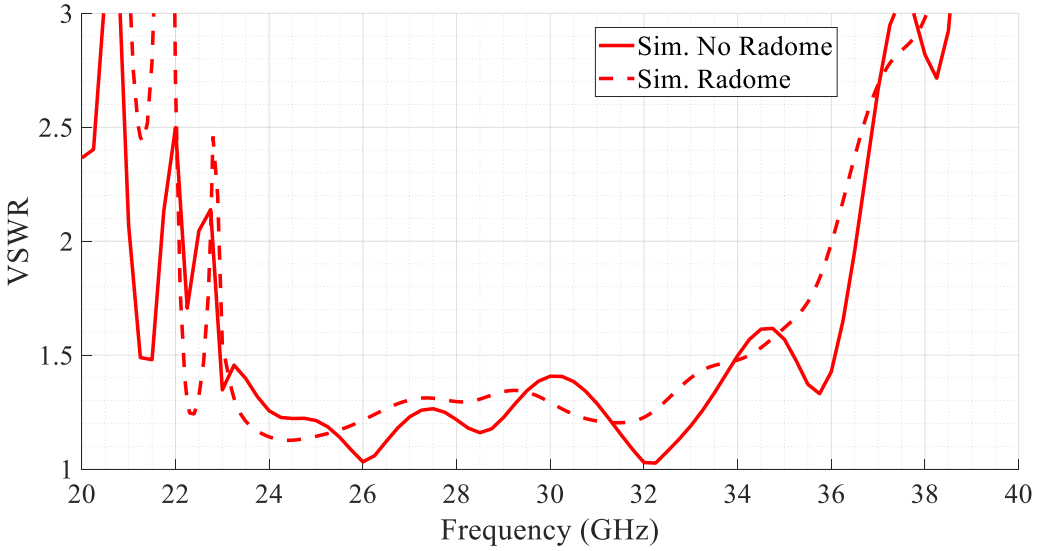


Fig. 51. VSWR for the simulated antenna with no radome and with the radome.

The realized gain and axial ratio are shown in Fig. 52. A minimum gain of ~14 dBic is achieved across the bandwidth. The axial ratio is presented in Fig. 4, with values < 3 dB in 0° to 14° elevation cones from 23 GHz to 30 GHz. However, from 30 GHz to 32 GHz, the AR is elevated above 3 dB. The performances obtained from the simulation are based on the radome material properties assumption presented in Table 6.

Radiation patterns at 24 GHz, 26 GHz, 28 GHz, 30 GHz, and 32 GHz are seen in Fig. 54 to Fig. 56, respectively. Cross-polarized radiation levels at boresight are demonstrated to be more than 20 dB down. Moderate sidelobe level suppression is also seen, with the highest lobe occurring around 13 dB down from boresight.

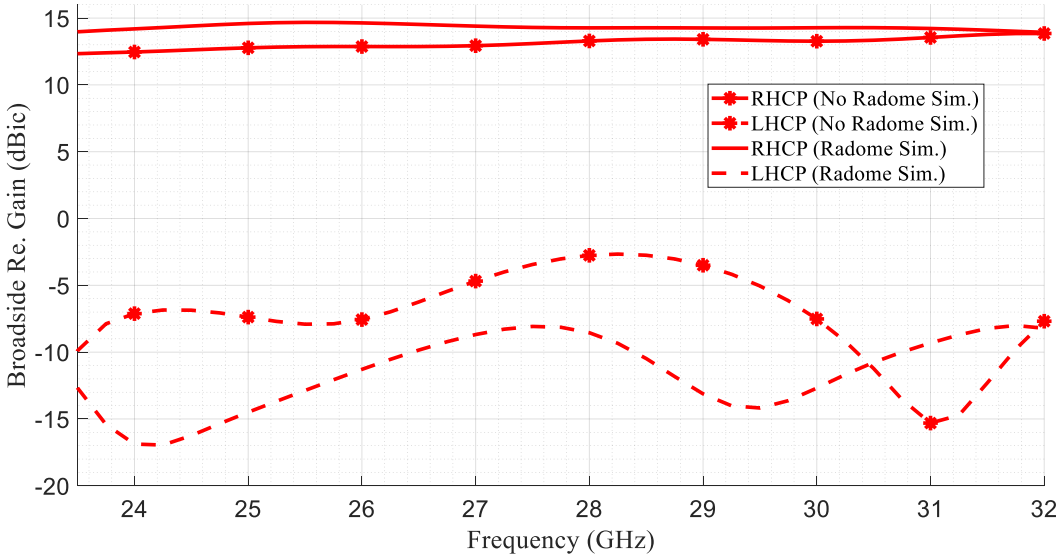


Fig. 52. Realized broadside gain for a millimeter wave helix with the radome.

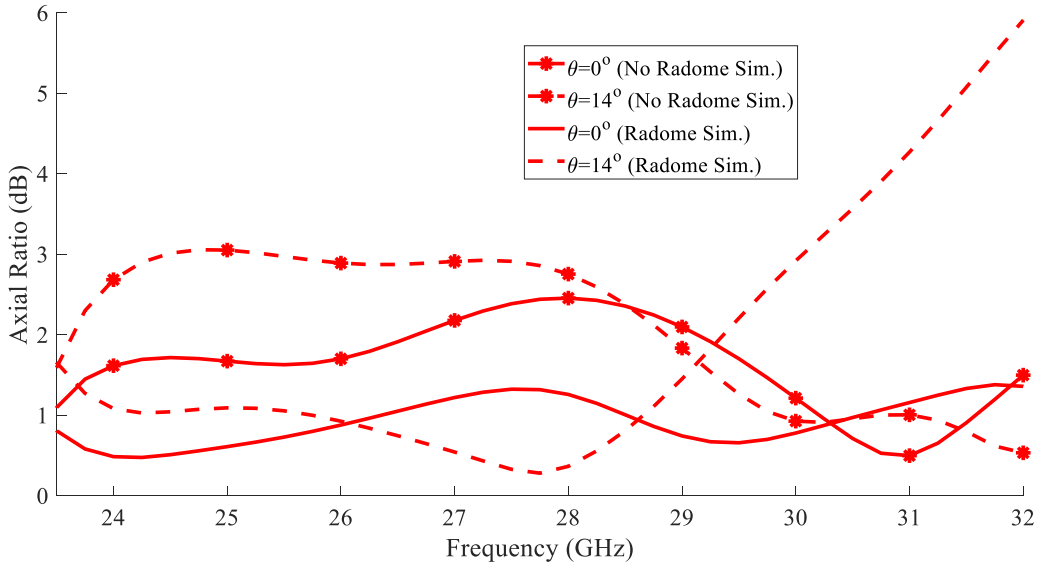


Fig. 53. Axial ratio with and without radome.

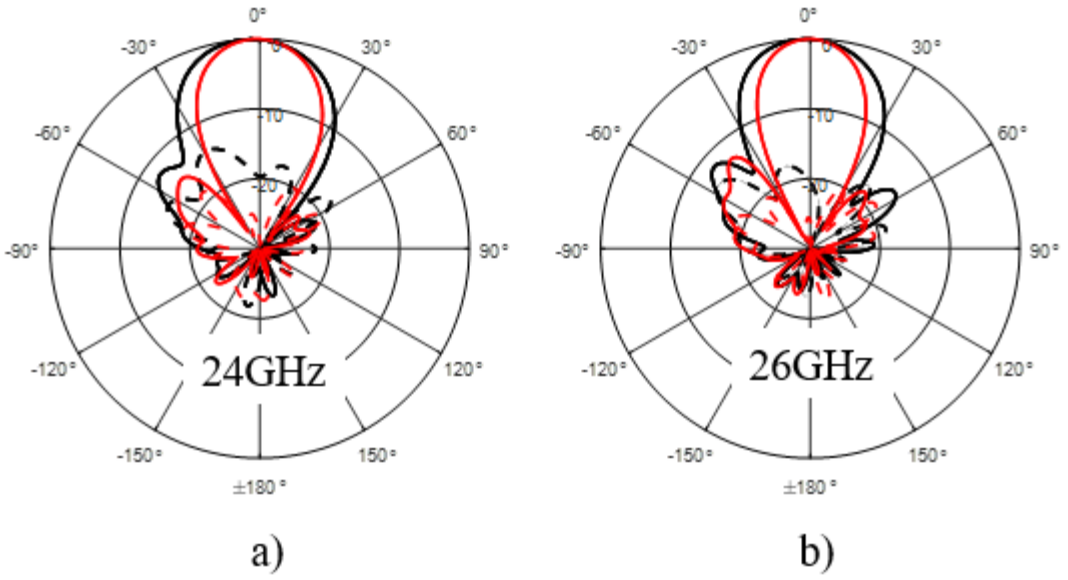


Fig. 54. Radiation patterns at 24 GHz (a) and 26 GHz (b), Co- (solid) and cross- (dashed) polarized, black line without radome and red line with radome case.

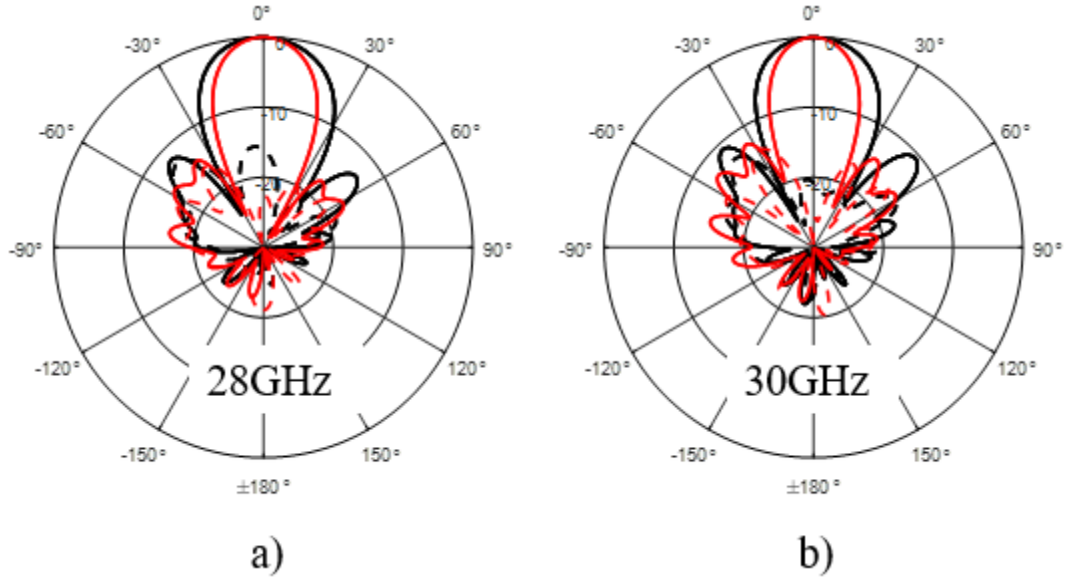


Fig. 55. Radiation patterns at 28 GHz (a) and 30 GHz (b), Co- (solid) and cross- (dashed) polarized, black line without radome and red line with radome case.

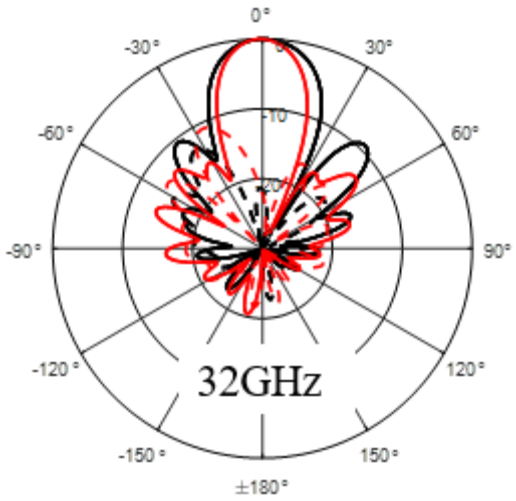


Fig. 56. Radiation patterns at 30 GHz, Co- (solid) and cross- (dashed) polarized, black line without radome and red line with radome case.

## 5.2. Helical Antenna Radome Fabrication and Measurements Results

For radome fabrication, Stereolithography and Fused Deposition Modeling are considered fabrication techniques. These two techniques are chosen based on in-house fabrication capabilities. For SLA fabrication, Formlabs Form 3 printer (Fig. 57a) is utilized with two types of resin, Tough V5 (Fig. 9a) and Rigid 4k (Fig. 57b). For FDM fabrication, the Rise 3D PRO2 printer (Fig. 8b) is used with two types of material as well, PLA (Fig. 9c) and LDPE (Fig. 9d). The fabricated radomes are shown in Fig. 58.

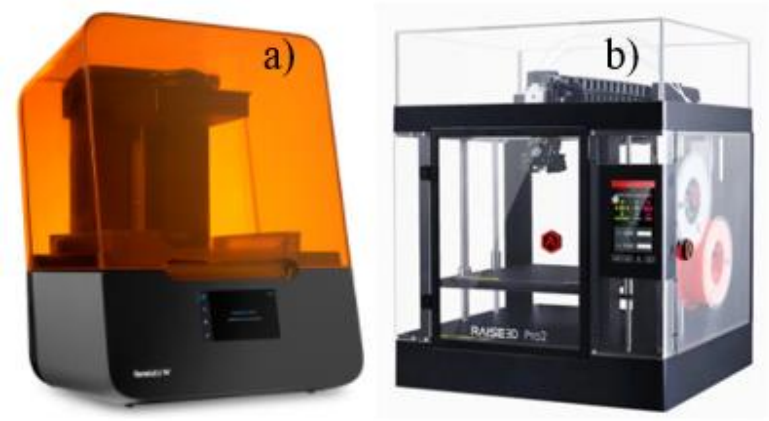


Fig. 57. Formlabs Form 3 printer (a) and Rise 3D printer.

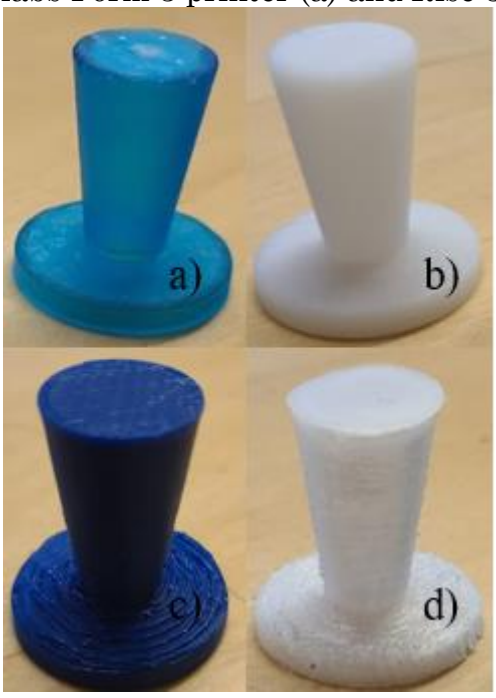


Fig. 58. Fabricated radomes in Tough V5 resin (a), Rigid 4k resin (b), PLA (c) and LDPE (d).

As presented in Fig. 58. Radomes in Tough V5, Rigid 4k, and PLA are fabricated with a high dimensional and geometrical accuracy. However, the radome fabricated in LDPE is not fabricated with satisfactory quality and shows signs of poor structural integrity.

In Fig. 59, the assembled antenna system is presented with a radome fabricated in PLA material, where the radome is attached to the ground plane on the outside surface using the press-fit. The same approach was used for all fabricated radomes.

Fig. 59. Assembled antenna system and PLA radome.

In Fig. 60, VSWR results are presented for FDM printed radomes, and in Fig. 61, VSWR results for SLA printed radomes. The two FDM printed radomes (PLA and LLDPE) perfume slightly differently, mainly due to poor fabrication of the LLDPE radome. The SLA printed radomes performed in much closer agreement. However, all tested radomes perfume well inside the bandwidth of interest, and anechoic chamber testing is needed to determine the best performing radome. Results for the case with and without the radome are presented to observe the radome design's impact on antenna system performance. Results indicate a minor impact on antenna performances. Moreover, in some areas improves performance.

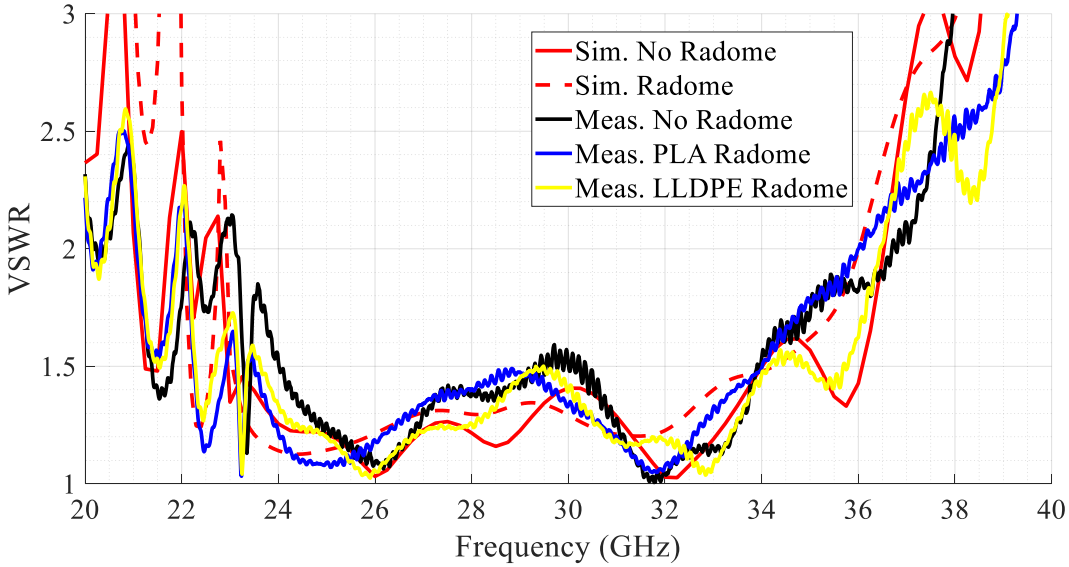


Fig. 60. VSWR measurements with FDM fabricated radomes.

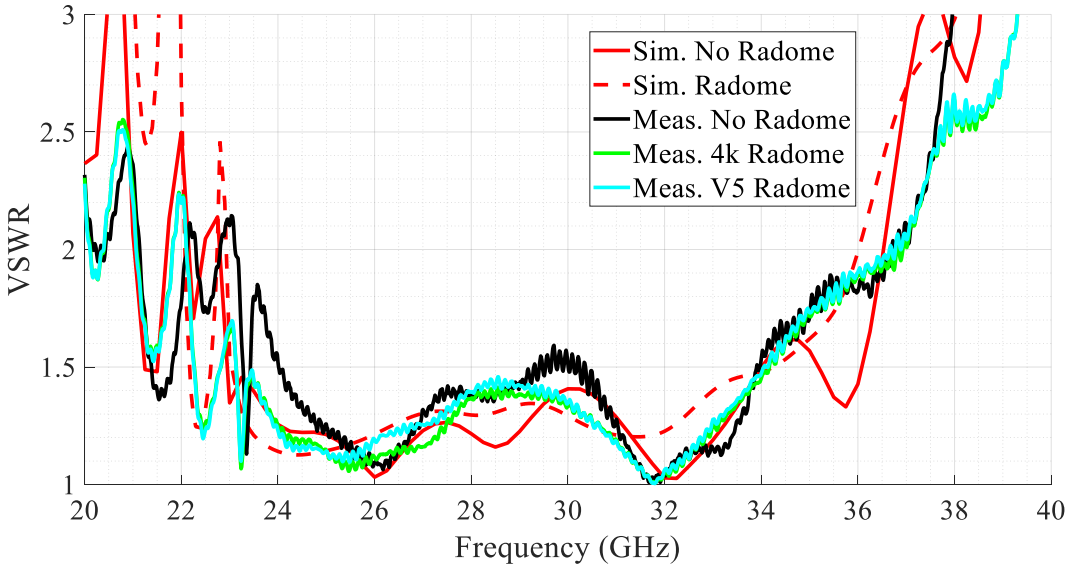


Fig. 61. VSWR measurements with SLA fabricated radomes.

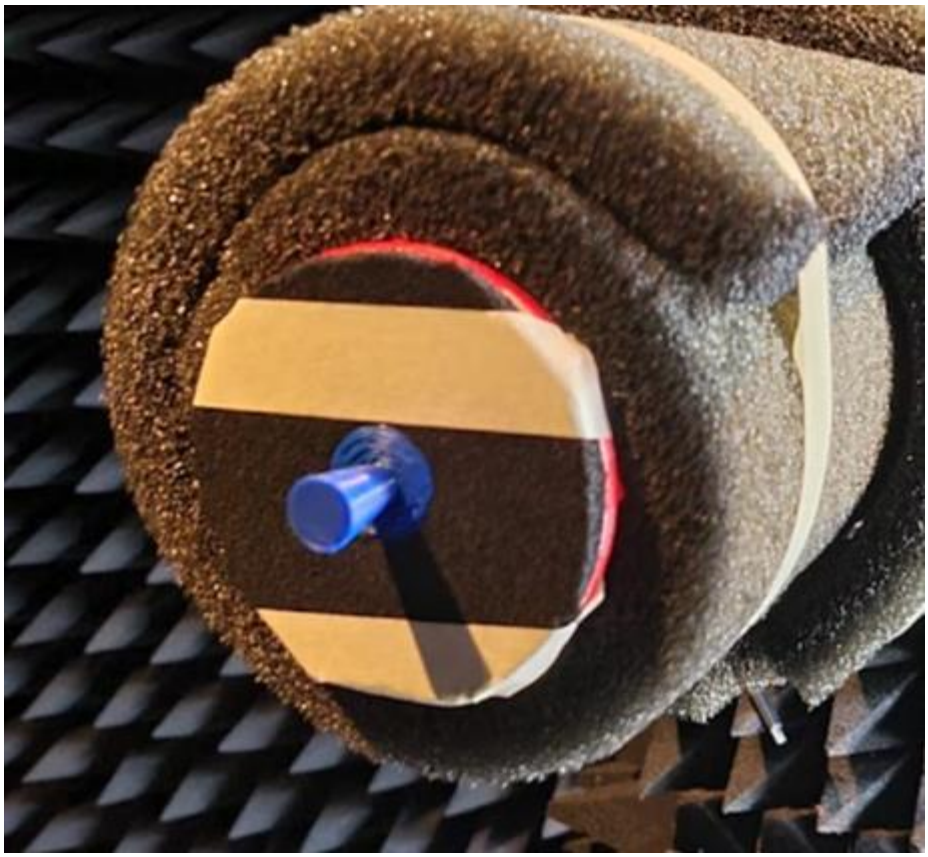

Fig. 62. Anechoic chamber setup.

The next step is antenna measurements in the anechoic chamber to observe the radome's impact on the far-field of the antenna system (Fig. 62). For all materials used in fabrication, measured results are presented for broadside realized gain (RHCP and LHCP) and axial ratio in Fig. 63 to Fig. 70. The best performances are observed for FDM PLA and FDM LDPE material, with the lowest impact on broadside gain and axial ratio. The SLA Rigid 4k and SLA tough V5 resin measurement results indicate higher dielectric loss and permittivity than expected. For the next step in the testing process (thermal/pressure testing), FDM PLA material is chosen since FDM LDPE material did not pass the fabrication test in terms of geometrical accuracy and structural integrity.

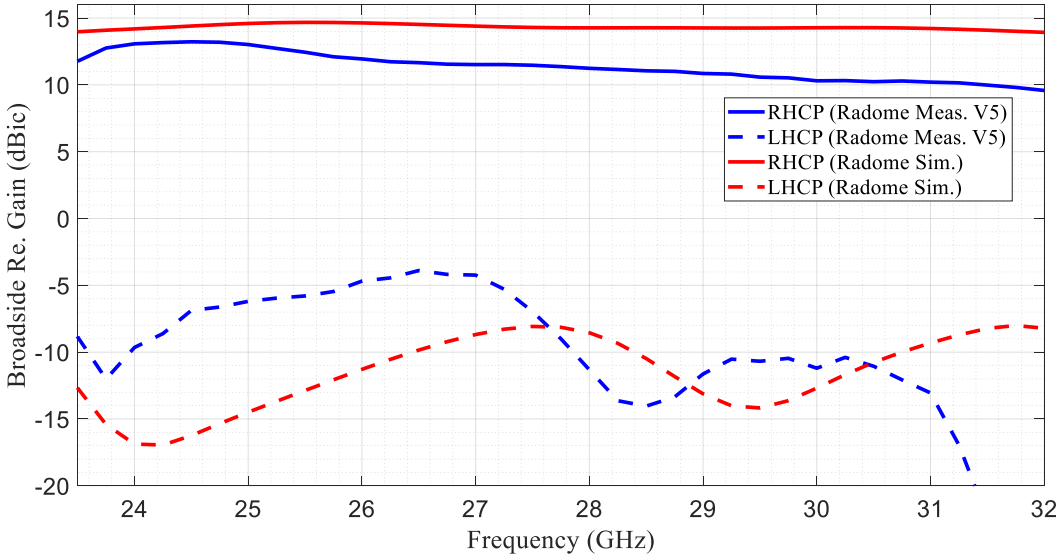


Fig. 63. SLA Fomlabs Tough V5 resin measured vs. simulated boreside gain.

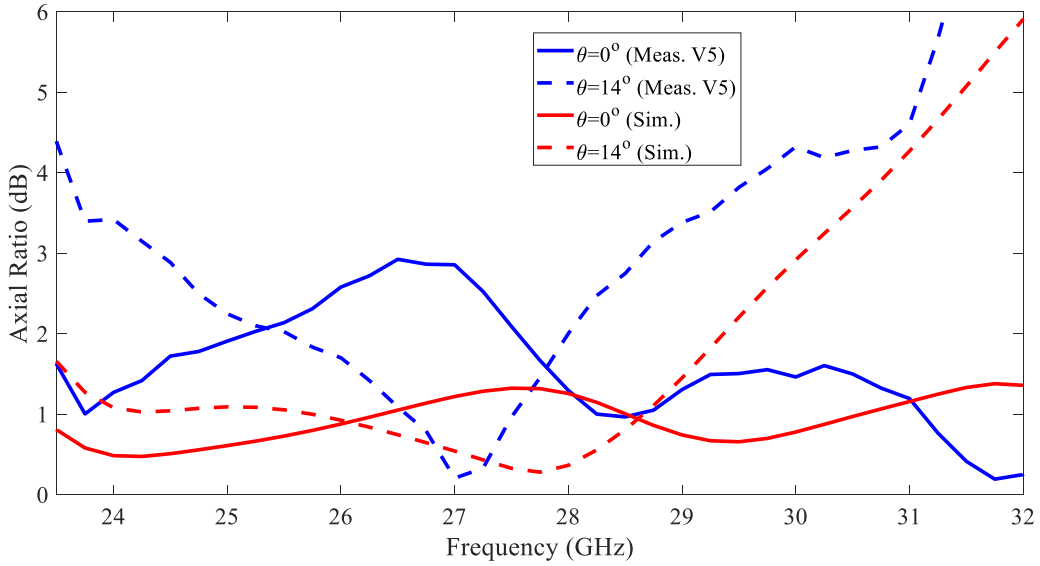


Fig. 64. SLA Formlabs Tough V5 resin measured vs. simulated axial ratio.

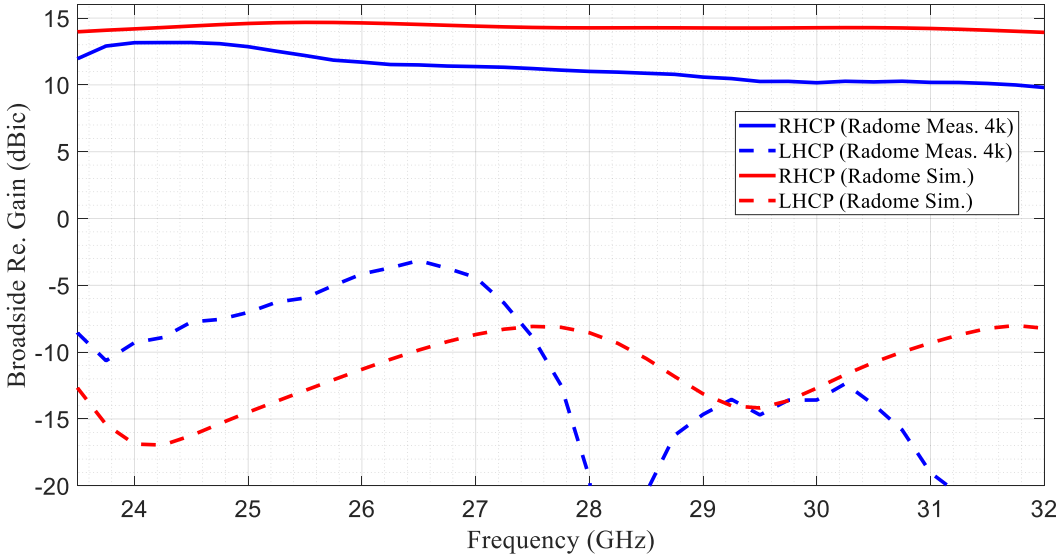


Fig. 65. SLA Fomlabs Rigid 4k resin measured vs. simulated boreside gain.

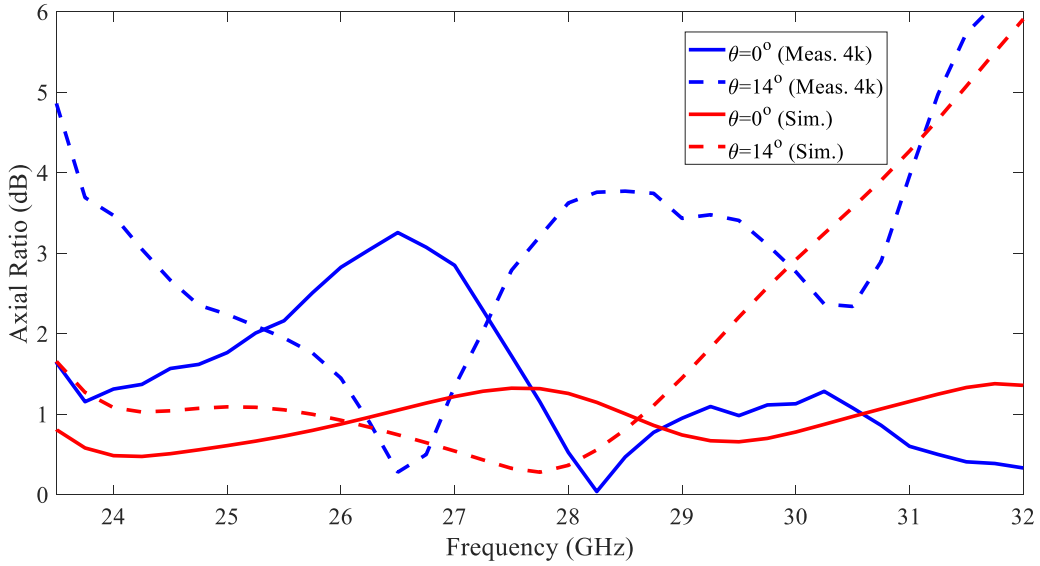


Fig. 66. SLA Formlabs 4k resin measured vs. simulated axial ratio.

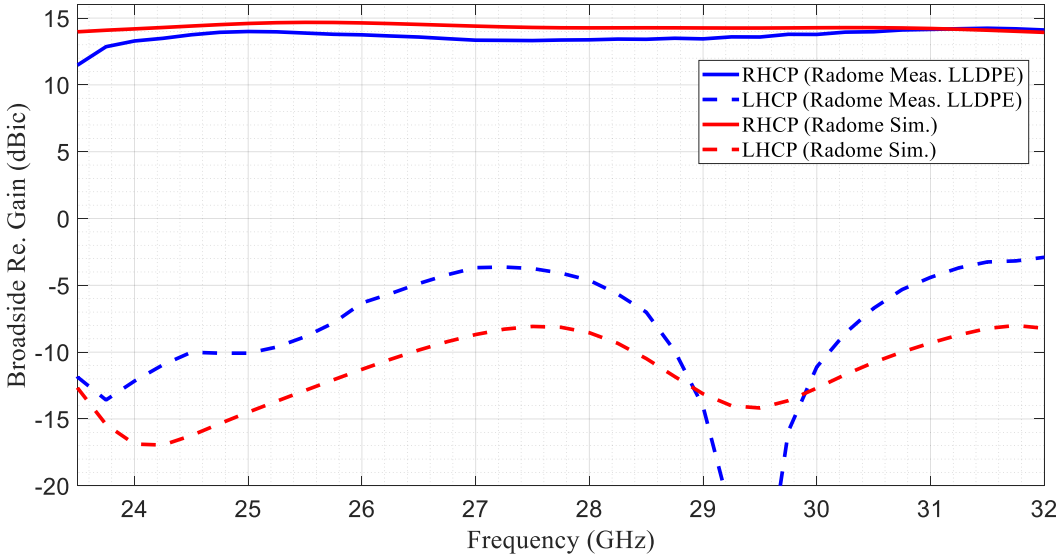


Fig. 67. FDM LLDPE measured vs. simulated brodeside gain.

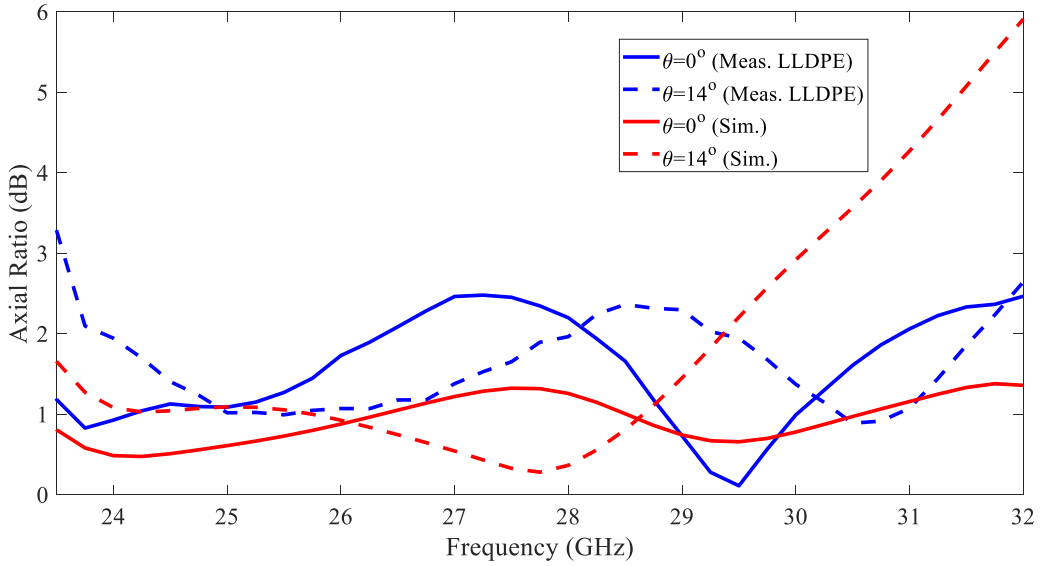


Fig. 68. FDM LLDPE measured vs. simulated axial ratio.

The results for FDM PLA material are presented in Fig. 69 to Fig. 70. The solid red line represents RHCP simulated results. The dashed red line of LHCP simulated results, the solid blue line represents measured RHCP, and the dashed blue line measured LHCP. It is noticed that FDM PLA material performs better than simulation between 30GHz and 32GHz regarding the axial ratio. This result indicates that the original assumption for permittivity of 2.6 was over-estimated and additional

simulation with lower permittivity material indicates that possibly PLA material is not homogeneous, meaning that a mixture of air and solid material is present, which reduces the effective permittivity. In Fig. 71 and Fig. 72, a permittivity study is presented for permittivities of 1.5, 1.8, 2, and 2.2 with respect to axial ratio impact. In Fig. 71, permittivity study for broadside direction and in Fig. 72 for an angle of 14˚ from broadside. The results of low permittivity impact are mainly noticed on the axial ratio for higher elevation angles (14˚) and less impact on a broadside, meaning that fabrication imperfections are mainly impacting broadside measured results. The lower permittivity is a good indicator from an RF perspective since lower permittivity helps the antenna perform well. However, from the mechanical perspective, this means that the structural integrity could be compromised inside the radome material since it is not homogeneous. This potential indicator is one more reason to use FDM PLA material for environmental testing since it has a higher chance of failure than homogeneous materials.

In Fig. 73 to Fig. 75, radiation patterns are presented for 24 GHz, 26 GHz, 28 GHz, 30 GHz, and 32 GHz, respectively. High agreement with simulations is observed in radiation patterns results for FDM PLA radome, particularly in the main lobe area. Also, minor deviations are observed regarding the sidelobe level.

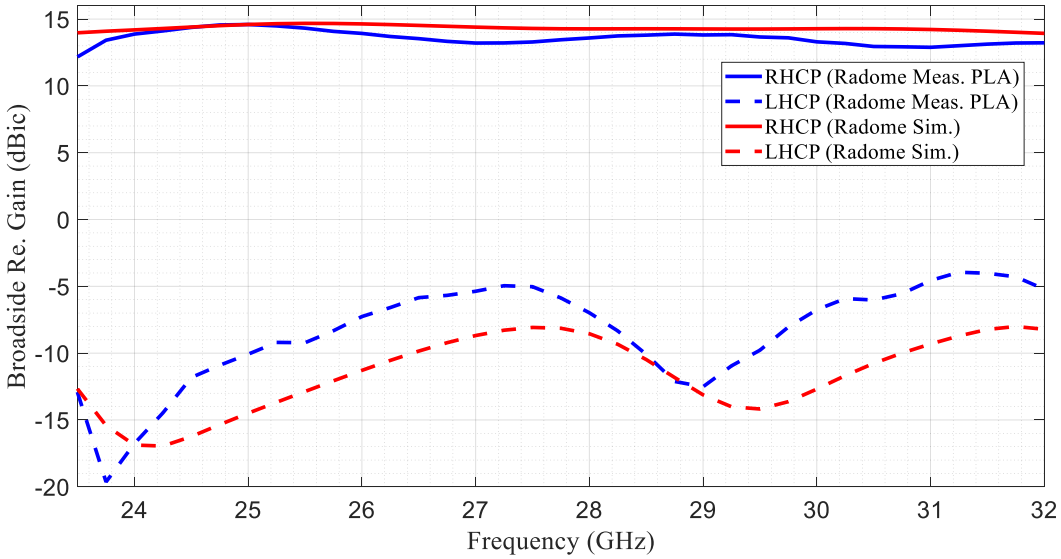


Fig. 69. FDM PLA measured vs. simulated broadside gain.

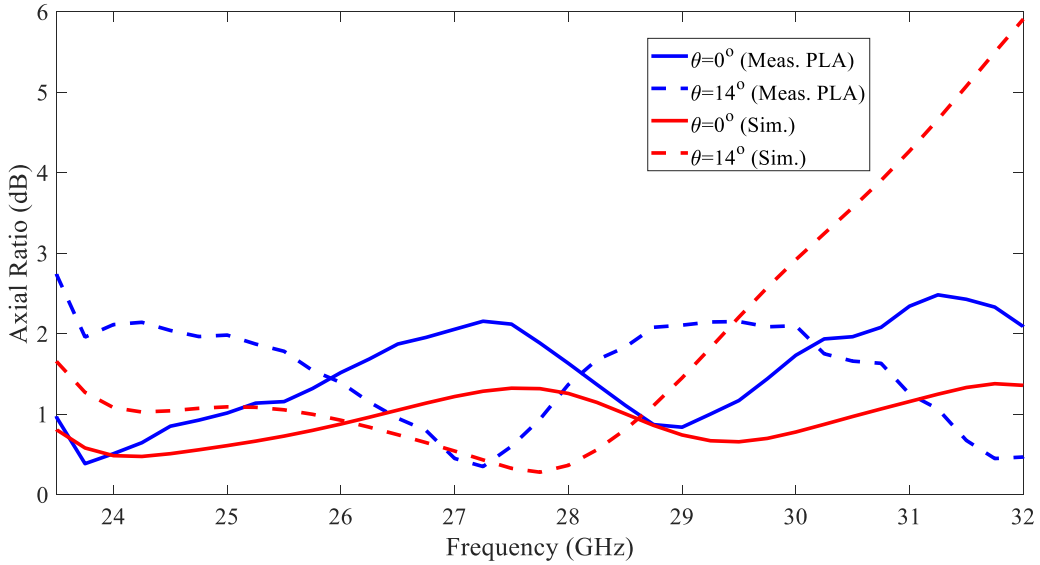


Fig. 70. FDM PLA measured vs. simulated axial ratio.

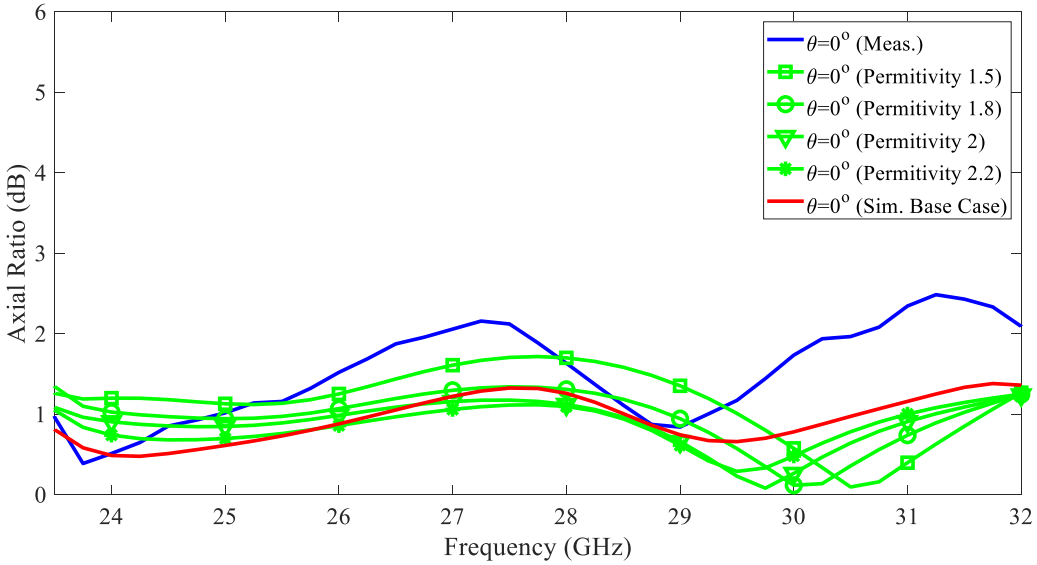


Fig. 71. Low permittivity study at broadside.

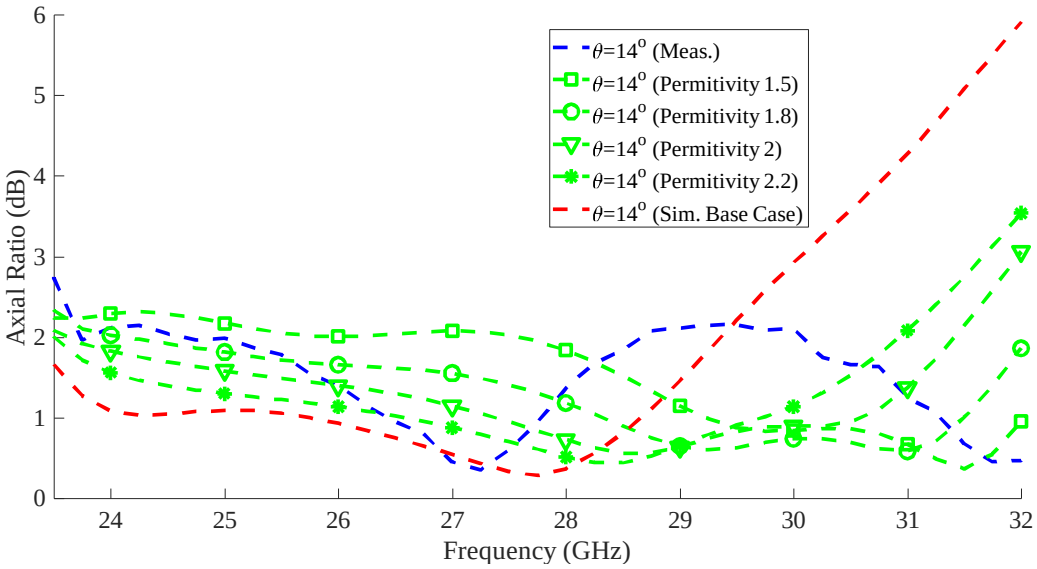


Fig. 72. Low permittivity at theta angle 14˚.

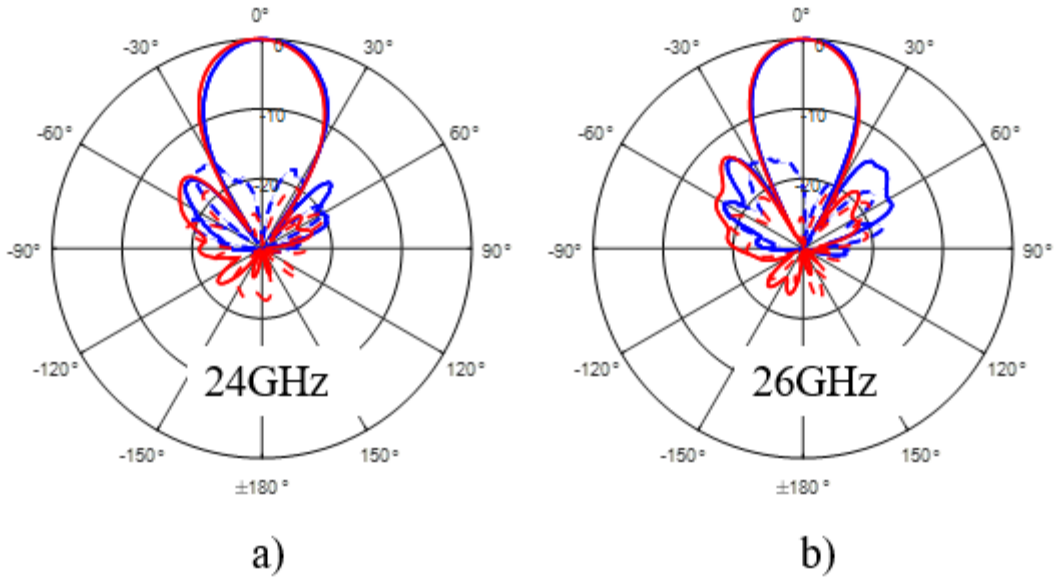


Fig. 73. Radiation patterns at 24 GHz (a) and 26 GHz (b), Co- (solid) and cross- (dashed) polarized, red simulation and blue measurments with PLA material.

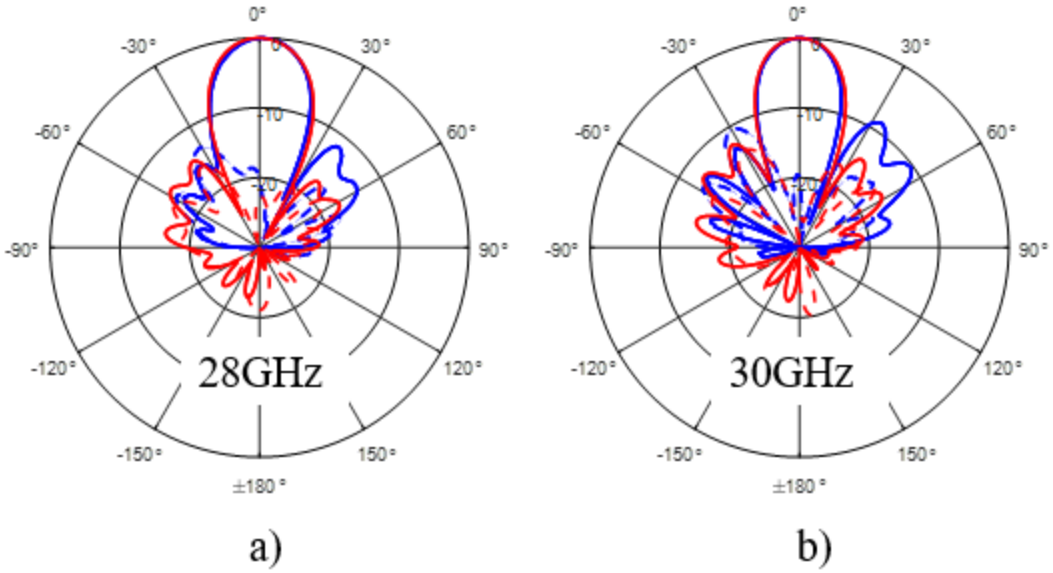


Fig. 74. Radiation patterns at 28 GHz (a) and 30 GHz (b), Co- (solid) and cross- (dashed) polarized, red simulation and blue measurements with PLA material.

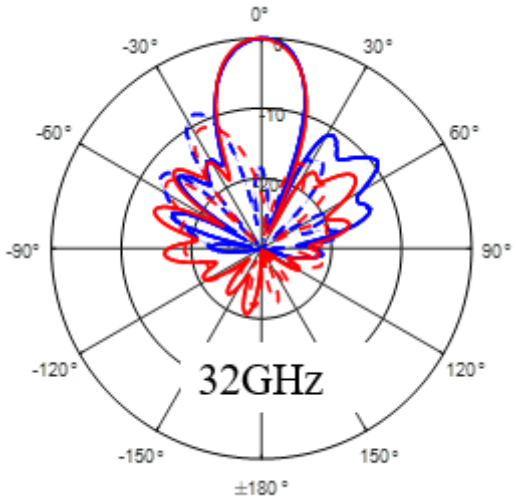


Fig. 75. Radiation patterns at 28 GHz, Co- (solid) and cross- (dashed) polarized, red simulation and blue measurements with PLA material.

## 5.3. Radome Measurements Results in Thermal/Pressure Chamber

As stated previously, the antennas on airborne platforms are subject to harsh environmental conditions such as rain and hail and a wide range of pressure and temperature conditions. Assessment of their ability to survive those conditions is typically done in expensive in-flight tests [39].

In this chapter design of a low-cost environmental test-bench is introduced. The main goal is to assess the survivability of the antenna under test (AUT). In this case it is a helical antenna with an integrated coaxial line and radome. Along with temperature drifting due to altitude change [36], airborne antennas will undergo two possible pressure conditions, specifically open and closed [35]. The open scenario assumes that the interior of the antenna is exposed to the ambient pressure level. In this case, a force acting on the radome is a dynamic wind load from the airspeed outside the antenna parallel to the speed vector. The typical airspeed of low altitude filing UAVs is around 200m/s. In the closed case, the antenna has internal pressure that acts on the radome from inside at the higher altitudes and the outside wind load

due to the airspeed. Also, at higher altitudes, the temperature can drop to -30˚C (-20 ˚C for 20,000 ft altitude), whereas it can be as high as 50˚C or more at low altitudes. Therefore, the structure needs to maintain its high-quality performance over the 80˚C temperature gradient.

Note that both pressure and temperature can affect the antenna performance due to the drift of tolerances. To ensure proper operation, it is necessary to test the antenna when it is subjected to the aforementioned conditions.

Commercially environmental chambers available on the market may have high initial and maintenance costs and occupy large space [40]. This work proposes a simple, cost-effective combined pressure and temperature test bench for the antenna performance while emulating being airborne.

The engineered test-beds are mainly made of commercial off-the-shelf parts and in-house-made frames with all components integrated into one assembly. The system is developed for antennas with diameters and lengths of 125 mm and 200 mm, respectively, occupying a relatively small volume. Moreover, it does not require unique skills for operation or high maintenance costs. The antenna under test (AUT) is enclosed in a specifically designed radome discussed earlier in this chapter.

For purposes of the thermal/pressure chamber design, it is necessary to assess the thermal properties of the material used for the chamber design. The list of materials used for antenna and chamber design is presented in Table 8. Those properties are later used in the equation below to calculate the power budget for the chamber.

TABLE 8.

Thermal/Pressure Chamber Material Properties.

| Parameter | Value |
|---|---|
| c = 897 J/kg C | Specific heat capacity Aluminum |
| c = 1012 J/kg C | Specific heat capacity Air |
| m al= rV =3.13 kg | Mass Aluminum |
| m air = rV =0.006 kg | Mass Air |
| W =$cm\Delta T$=11.3kJ | Energy |
| r = 2700 kg/m3 | Aluminum density |
| V =1.15e-4 m3 | Core volume |
| t = 300 sec | Cooling time |

$$Q_c = Efficiency\ xP_{el} = 21W$$

$$P = \frac{W}{t} = cm\Delta T/t = 400W$$

$$N = ceil(P/Q_c) = 20$$

The power budget is necessary to calculate the power supply design and to determine the number of thermoelectric elements needed for the required chamber operation. The number of elements is chosen from the diagram presented in Fig. 77. The highlighted curve represents the element's efficiency for the required difference between the hot and cool sides of the thermoelectric element. $P_{el}$ is the power consumption of the element (60W) specified by the manufacturer. With efficiency for the required difference between the hot and cold side of 45%, the calculated heat power per element is 21W. For the given volume, specific heat capacity (Table 8), and time for cooling (5 minutes) in ideal conditions (meaning no heat transfer with the environment around the system), the total heat power required is about 400W. From there, we can obtain the minimal number of elements, 20. The preferred number of elements for the geometrical symmetry is 24 (6 rows with four elements). Total power consumption, in this case, is 1440W. In Fig. 76, a basic schematic of the thermoelectric element is presented.

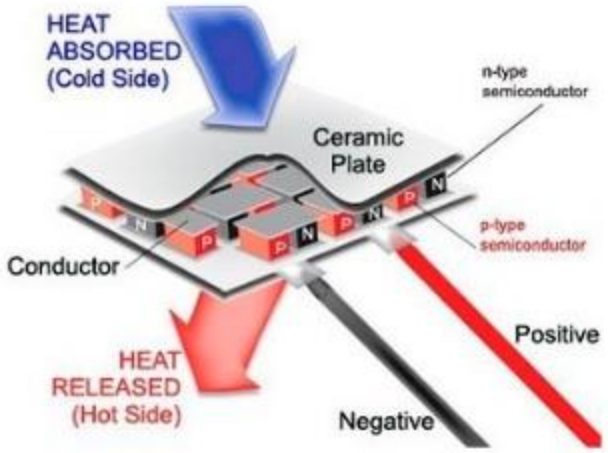


Fig. 76. Thermo-electric element [37].

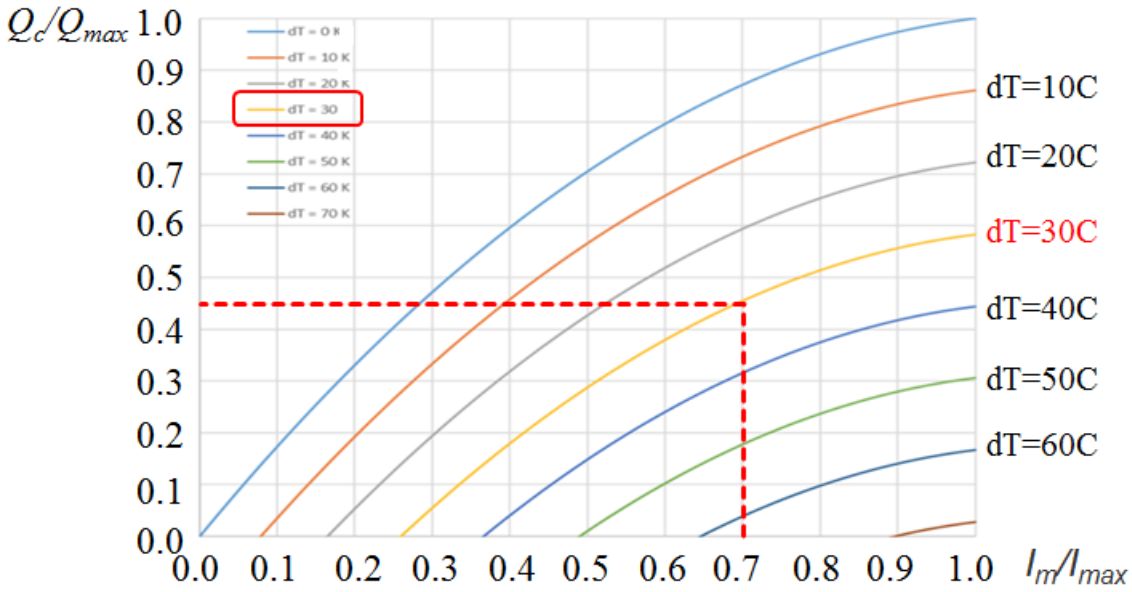


Fig. 77. Thermo-electric pump efficiency diagram [38].

In Fig. 78, the thermal/pressure chamber design is presented with Computational Fluid Dynamics simulation results (CFD) [41]. An ambient temperature of 22˚C surrounds the model. Film coefficient boundary condition is applied (heat transfer coefficient). The value of the film coefficient is 10 W/m^2K. The results show the uniform temperature distribution through the volume.

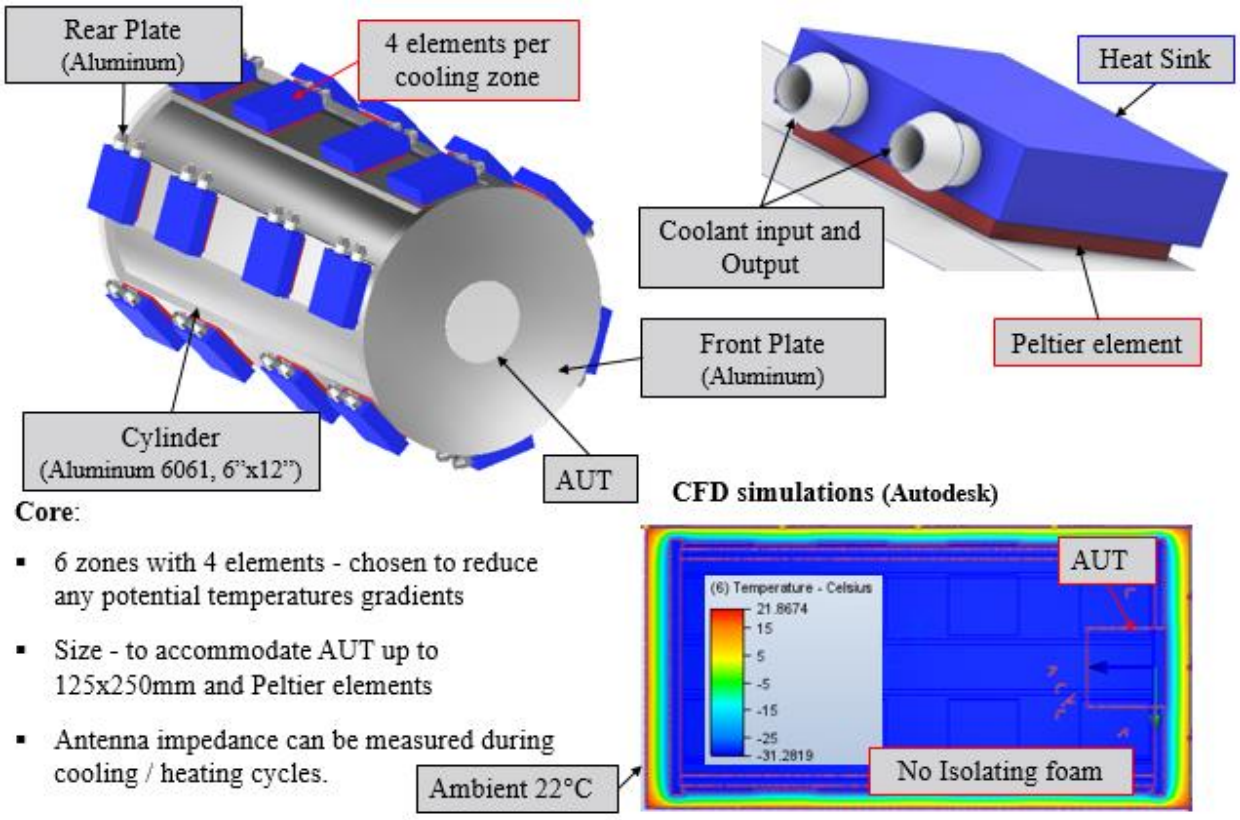


Fig. 78. Thermal/Pressure chamber layout.

Since it is necessary to control the temperature on the hot side of the thermoelectric element, a heat sink is introduced, and coolant water is used. To further reduce the temperature of the hot side of the thermoelectric element, ice is added to water, meaning that the hot side is about 4˚C, enabling about -24˚C overall, having in mind that from Fig. 77, the expected temperature difference is going to be at least 30˚C.

To increase system flexibility, the front flange is made to be the adapter for different AUTs. In Fig. 79, the adapter for the helical antenna system is presented. The material is aluminum for maximum conductivity. Between all components, thermo-conductive epoxy is used.

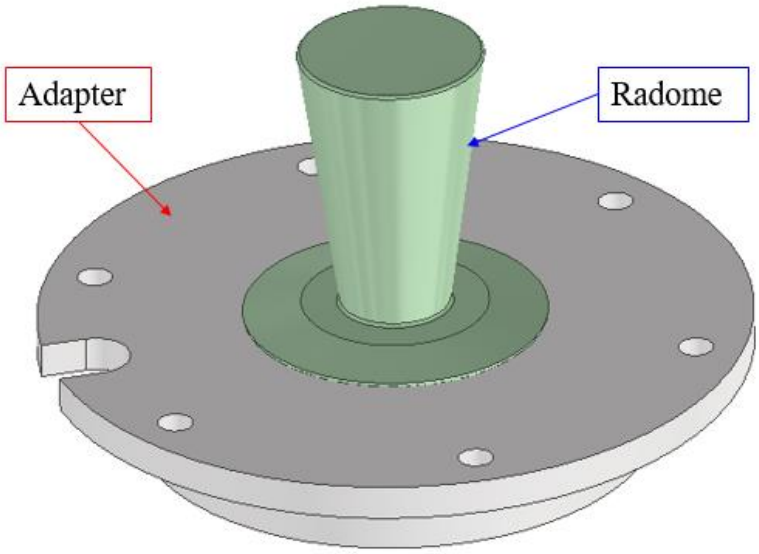


Fig. 79. Custom adapter design.

The simplified block diagram and fully assembled Thermo/pressure system is presented in Fig. 80. The system enables the change of the temperature below -20 ˚C and monitors the reflection coefficients in real-time.

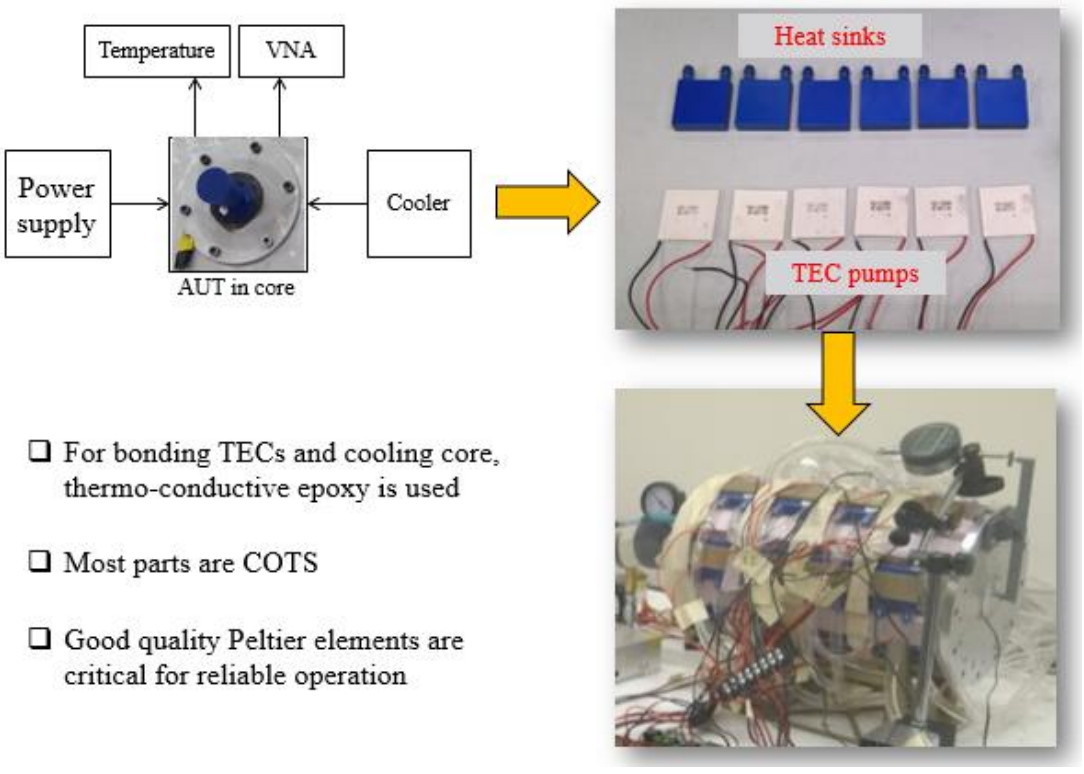


Fig. 80. Thermal system block diagram and fully assembled system.

The system also has a pressure control system. Typical flying conditions for low-altitude UAVs go up to 20,000 ft. Here two scenarios are considered, open and closed. The force distribution for two cases is presented in Fig. 81. From the analysis for an object flying up to 20,000 ft in height, with an airspeed up to 400 knots, and with a diameter of the AUT up to 50 mm, the anticipated pressure on the radome (open case worst-case scenario) is about 6.5 psi. The block diagram of the pressure system and the fabricated system is presented in Fig. 82. The system can operate simultaneously with the thermal system described earlier to monitor the reflection coefficient response in real-time. The system is capable of testing the antennas systems for vacuum as well, and it is capable of achieving 80% of vacuum.

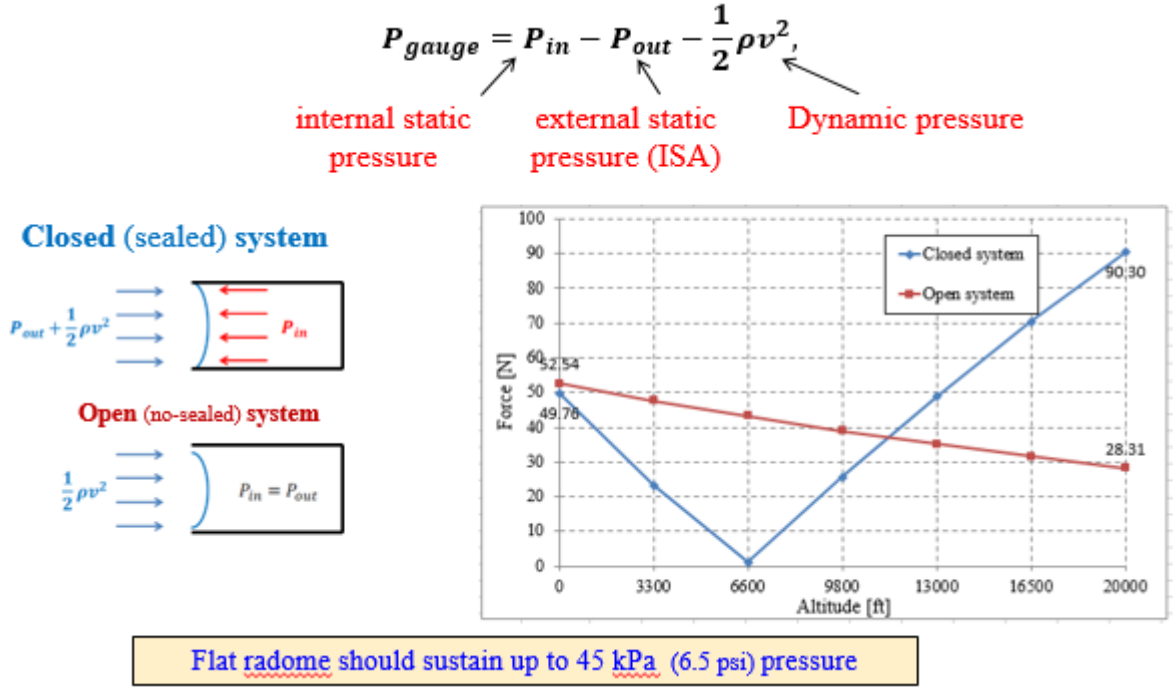


Fig. 81. Pressure system analysis.

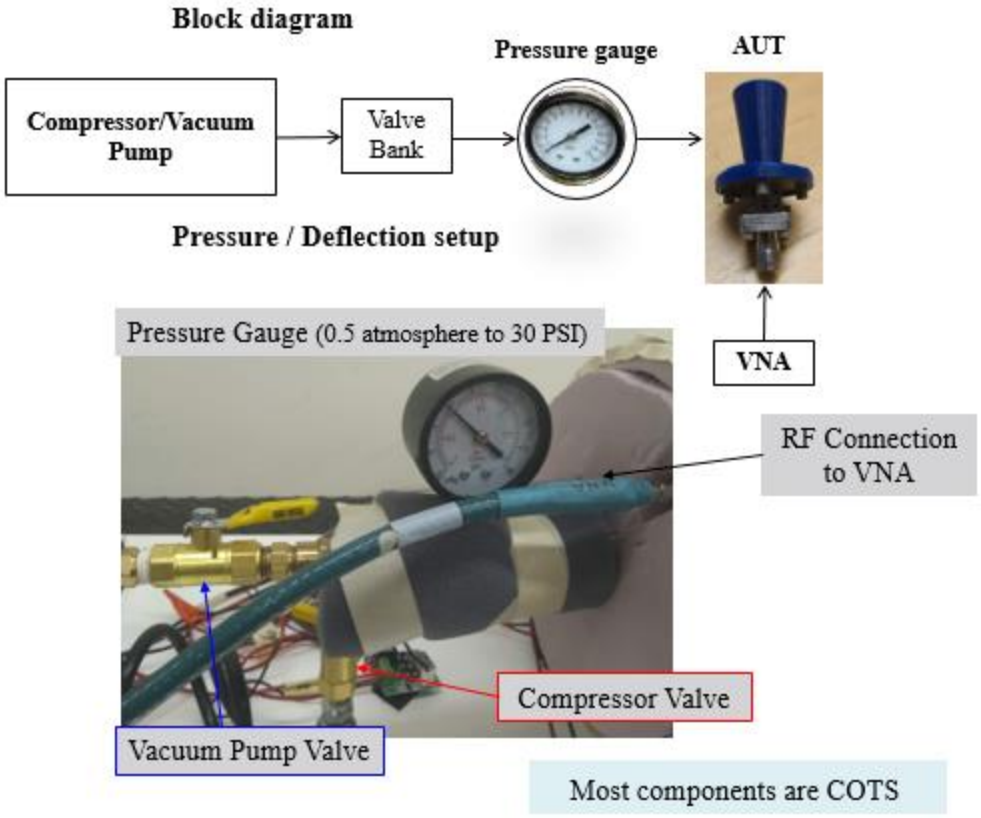


Fig. 82. Pressure system block diagram.

The fully assembled system is presented in Fig. 83. with a helical antenna system assembled with an aluminum adapter. The thermal/pressure system is fully fabricated and assembled in-house.

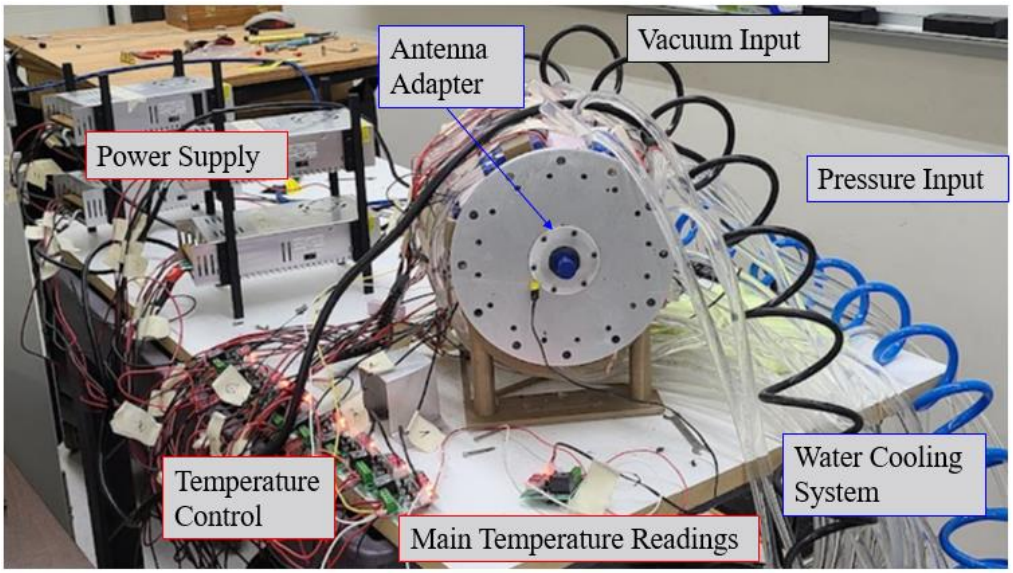


Fig. 83. Thermal/Pressure measurement system layout.

For a system to be fully operational, it takes about 30 minutes. First, recirculation pumps are used for cooling water, then the plumbing for the vacuum and pressure system is connected, and finally, the PNA is calibrated. The calibration port is inside the chamber. After the calibration is done, the antenna and the adapter flange (Fig. 79.) are assembled with the rest of the system and connectorized. The next step is to add ice to the cooling water, and when a system reaches a temperature between 0˚C and 4˚C, the thermoelectric elements are started. From this point in time to the point when the temperature hits -20˚C, it takes about 15 minutes. This is because the system is not ideally thermally isolated from the ambient temperature. To improve thermal isolation, foam is used. The minimum temperature achieved during the test is -22 ˚C, with the test lasting 30 minutes after the system reached a steady state.

Since the PNA is a very sensitive piece of equipment, the RF cable was disconnected when DC power was on to prevent any potential damage to the PNA. The impact of the disconnecting and reconnecting is presented in Fig. 84. There is no significant impact on calibration inside of the band of interest (23 GHz to 32 GHz).

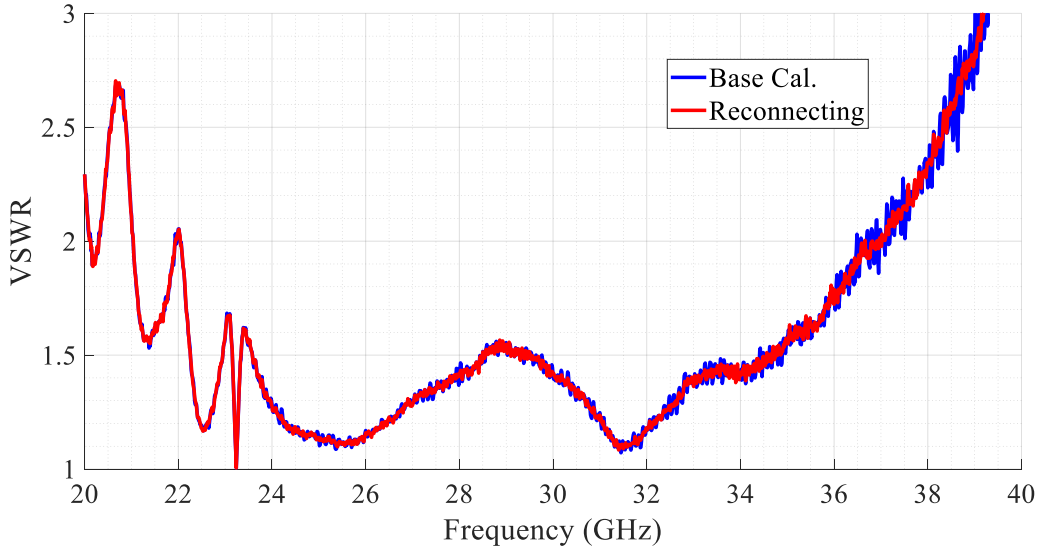


Fig. 84. Connecting and reconnecting test.

In Fig. 85, the temperature during the cooling test is presented, and ice formation was noticed on the chamber outside the wall during the test. During the cooling test, vacuum and pressure tests were performed (Fig. 86). A vacuum/pressure gauge is presented, and 0.5 atmospheres are achieved in a vacuum with 20 psi of pressure. The same test was performed during the hearing test after 30 minutes at -22 ˚C. The thermoelectric elements were turned off, and after the polarization switching, the heating process was started. The main probe at that time measured -10˚C.

For the system to reach 50˚C, about 20min. was needed. In Fig. 87, the maximum heating temperature is presented. The system is constrained to a maximum of 50˚C since that is the maximum operational temperature for thermo-electric elements.

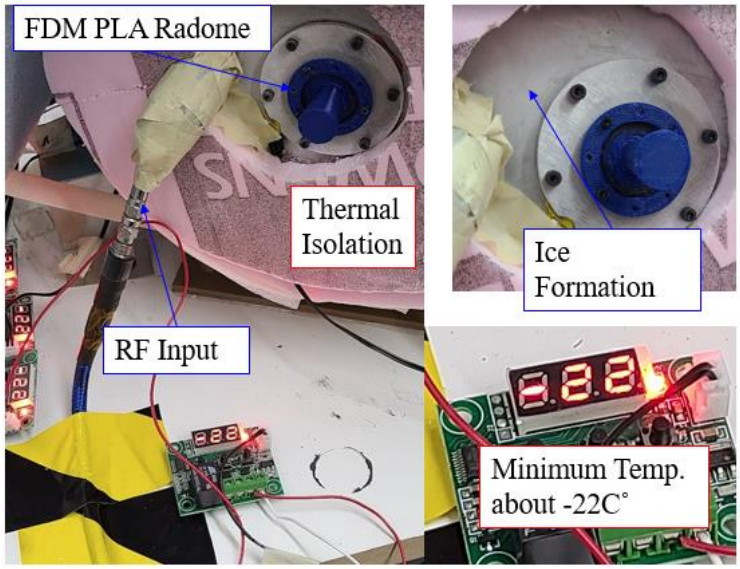


Fig. 85. Cooling temperature measurement.

Fig. 86. Vacuum/Pressure measurements.

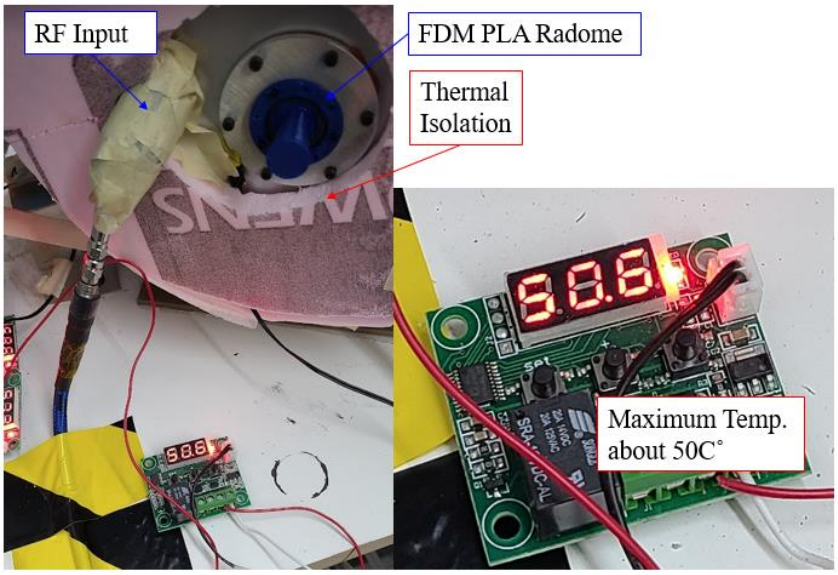


Fig. 87. Heating temperature measurements.

In Fig. 88. Heating and cooling results vs. ambient measurements for VSWR are presented. The biggest impact on the system is above 35GHz. However, it is quite minor. It is good to mention that after performing cooling and heating testing, a control test was conducted. The results are the same as the initial measurements, meaning the testing procedures do not impact the results. In Fig. 89 and Fig. 90, the vacuum and pressure test is presented during the cooling and heating, respectively. There is no significant impact inside the band of interest.

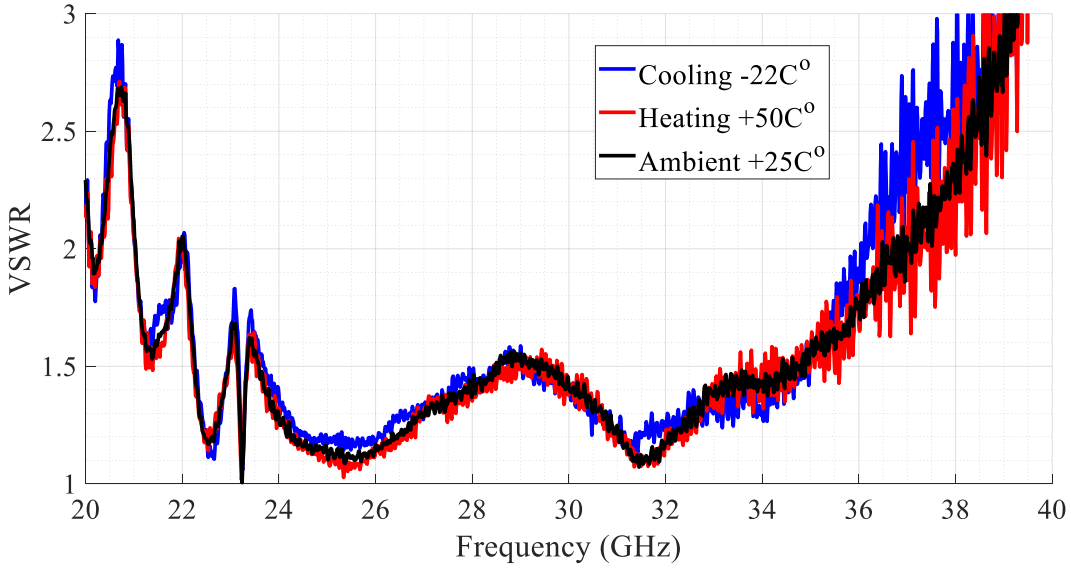


Fig. 88. Measured VSWR for cooling and heating.

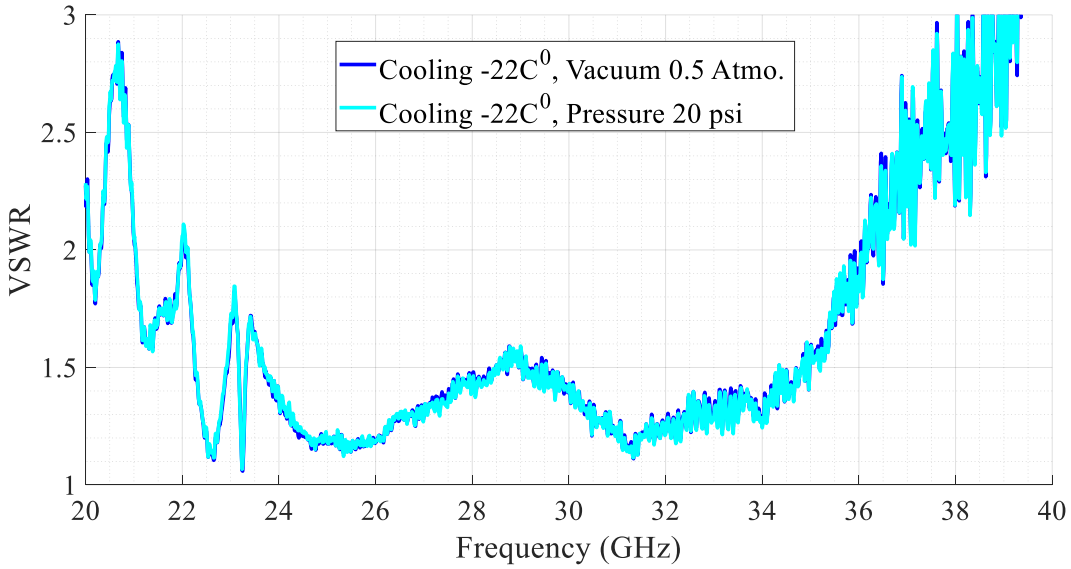


Fig. 89. VSWR for vacuum and pressure condition at -22C°

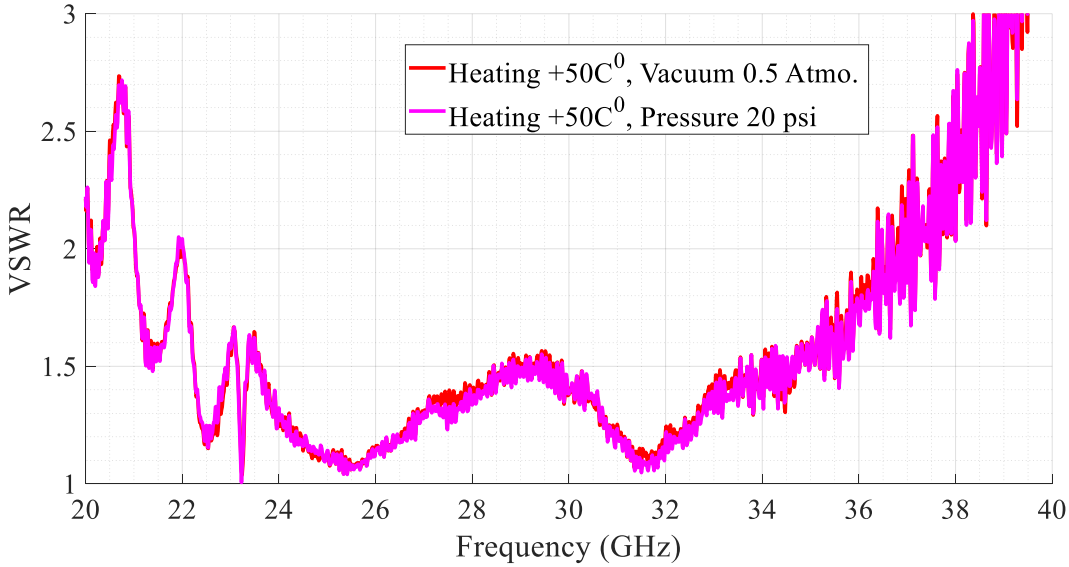


Fig. 90. VSWR for vacuum and pressure condition at 50C°.

## 5.4. Conclusion

Radome design is demonstrated for a millimeter-wave helical antenna. The radome is designed for fabrication with stereolithography and fused deposition modeling. VSWR 1.5:1, realized gain of ~14dBic, and axial ratio < 3 dB within the 14° field of view are obtained. Measurement results indicate that SLA material impacts the antenna performances more than FDM materials, mainly due to the possible mixture of air and FDM filament causing smaller permittivity. The best performing radome made from PLA is later used for thermal/pressure tests, and temperature and drifting pressure impact on electrical and mechanical performances inside of the band of interest is minor.

As a part of future work, more temperature tests and pressure tests are planned, particularly for temperatures higher than 50C° for more detailed FDM PLA radome characterization.

Acknowledgment

This work is funded by the Office of Naval Research under grant N00014-21-1-2641.

# CHAPTER VI

# CONCLUSION

This work presents a study for design and fabrication of millimeter-wave devices like an air-filled coaxial transmission line, coaxial quadrature hybrid, helical antenna, and radome with additive manufacturing. Techniques, such as DMLA, SLA, and FDM are emphasized.

The all-metal circular coaxial transmission line is designed for operation in K/Ka bands (Chapter II). The DMLS fabrication process-guided design for manufacturing yielded an 11.8 mm long line segment that works over 20-39GHz bandwidth with insertion loss < 0.35 dB and returns loss > 20 dB. The element is intended to be used as a mechanical anchor for other components and subsystems prototyped with 3D printing. Excavation and post-fabrication autopsy have shown good integrity of the device contacts and physical structure. In addition, from a mechanical perspective, it is calculated that for an anchor with two stabs, a diameter of 0.75 mm and a mainline of 1 mm in diameter, low-grade material stainless steel can sustain a load of 0.2 kg for the static material condition and 0.127 kg for dynamic material condition.

Impact of surface roughness and other imperfections, bandwidth increase, as well as integration with RF devices are all part of future studies.

The coaxial quadrature hybrid is demonstrated in the DMLS additive manufacturing technique (Chapter II). The fabrication is conducted in a split block configuration, and for conectorization, 2.4mm connectors were used. From the fabrication side, the primary constraint is the minimum feature size of 0.75mm, having in mind the DMLS process, aluminum alloy as a material, and direction of printing. The central operating frequency is 20GHz, and the amplitude and phase

imbalances are less than 1dB and 0.3˚, respectively, from 18.5GHz to 20.5GHz. One of the main emphases of future work includes increasing the operating bandwidth and reducing the number of fabricated components. Ideally, monolithic fabrication is preferable.

A helical antenna with integrated circular coaxial transmission line anchor and the ground plane is designed for operation in K/Ka bands (Chapter IV). The design for manufacturing in DMLS, is carried out. A 36.3mm tall antenna that works over 23.5-28GHz bandwidth is demonstrated. Post-processing steps are discussed for both processes. The successful experimental demonstration of impedance and pattern measurements showcases the suitability of all-metal additive manufacturing for prototyping devices of this and similar kinds. Improvement in SLA design for fabrication will be part of future works.

Radome development is demonstrated for a millimeter-wave helical antenna (Chapter V). The radome is designed for fabrication with SLA and FDM. VSWR 1.5:1, realized gain of ~14dBic, and axial ratio < 3 dB within the 14° field of view are obtained. Measurement results indicate that SLA materials impact the antenna performances more than FDM materials, mainly due to the possible mixture of air and FDM filament causing smaller permittivity. The best performing radome made from PLA is later used for thermal/pressure tests. Temperature and drifting pressure impact on electrical and mechanical performances inside of the band of interest are minor. As a part of future work, more temperature tests and pressure tests are planned, particularly for temperatures higher than 50C˚ for more detailed FDM PLA radome characterization.

# BIBLIOGRAPHY

[1] Terry Wohlers, Tim Gornet, “History of additive manufacturing”, Wohlers Report, 2016,

[2] S. Manafi, M. Al-Tarifi, and D.S. Filipovic, “45–110 GHz quad-ridge horn with stable gain and symmetric beam,” IEEE Transactions on Antennas and Propagation, vol. 65, no. 9, pp. 4858-4863, July 2017.

[3] S. Manafi, M. Al-Tarifi, and D. Filipovic, “Millimeter-wave double-ridge waveguide and components,” IEEE Transactions on Microwave Theory and Techniques, vol. 66, no. 11, pp. 4726-4736, August 2018.

[4] S. Manafi, M. Al-Tarifi, and D. Filipovic, “Isolation Improvement Techniques for Wideband Millimeter-Wave Repeaters,” IEEE Antennas and Wireless Propagation Letters, vol. 17, no. 2, pp. 355-358, January 2018.

[5] L. Gibson, D. Rosen, B. Stucker, “Additive manufacturing technologies: rapid prototyping to direct digital manufacturing”, Springer, New York, NY, 2009

[6] Concurrent Technology Corporation [Online]. Available: https://www.ctc.com/public/solutions/techandinnovation/additive-manufacturing-hybrid,

[7] Formlabs company [Online]. Available: https://formlabs.com/blog/ultimate-guide-to-stereolithography-sla-3d-printing/

[8] Manfred Schmida, Antonio Amadoa, and Konrad Wegenerb, “Polymer powders for selective laser sintering (SLS)”, AIP Conference Proceedings 1664, 160009 (2015),

[9] Ankita Jaisingh Sheoran, Harish Kumar, “Fused Deposition modeling process parameters optimization and effect on mechanical properties and part quality: Review and reflection on present research”, Volume 21, Part 3, 2020, Pages 1659-1672,

[10]Protolabs company [Online]. Available: https://www.protolabs.com/services/3d-printing/,

[11]Loughborough University, United Kingdom, Additive Manufacturing Group, [Online]. Available: https://www.lboro.ac.uk/research/amrg/about/the7categoriesofadditivemanufacturing/binderjetting/

[12]D. D. Gu, W. Meiners, K. Wissenbach, and R. Poprawe, Laser additive manufacturing of metallic components: materials, processes, and mechanisms, International Materials Reviews, vol. 57, pp.133-164, 2012/05/01 (2012).

[13]All 3D Printing [Online]. Available: https://all3dp.com/2/how-much-does-a-metal-3d-printer-cost/

[14]J. J. Adams, E. B. Duoss, T. F. Malkowski, M. J. Motala, B. Yeop Ahn, R. G. Nuzzo, J. T. Bernhard, and J. A. Lewis, "Conformal printing of electrically small antennas on three-dimensional surfaces, Advanced Materials, vol. 23, no. 11, pp. 1335-1340, 2011,

[15]M. Ahmadloo and P. Mousavi, "A novel integrated dielectric-and-conductive ink 3D printing technique for fabrication of microwave devices," IEEE MTT-S International Microwave Symposium Digest (IMS), Seattle, WA, June 2013.

[16]Galati, Manuela & Minetola, Paolo, “Analysis of Density, Roughness, and Accuracy of the Atomic Diffusion Additive Manufacturing (ADAM) Process for Metal Parts” Materials. 12. 4122. 10.3390, 2019,

[17]HFSS: High Frequency Structure Simulator Ansoft Corporation [Online]. Available: http://www.hfss.com.

[18]Z. Popovic, S. Rondineau, D. Filipovic, D. Sherrer, C. Nichols J. Rollin, and K. Vanhille, "An Enabling New 3-D Architecture for Microwave Components and Systems", Microwave Journal, vol. 51, pp. 66, Feb. 2008.

[19]Y. Qin, “Integrated, multidisciplinary approaches for micro-manufacturing research, and new opportunities and challenges to micro-manufacturing,” Journal of Nanomaterials, Nanoengineering, and Nanosystems. vol. 232, no. 1, pp. 5-21, Nov. 2017.

[20]V. Palazzi, P. Mezzanotte, F. Alimenti, M. Tentzeris, and L. Roselli, "Microfluidics-based 3D-Printed 4 × 4 Butler Matrix in Coaxial Technology for Applications up to K Band," in Proc. IEEE MTT-S International Microwave Symposium (IMS), 2019, pp. 1371-1374.

[21]J. Shen, D. P. Parekh, M. D. Dickey, and D. S. Ricketts, "3D Printed Coaxial Transmission Line Using Low Loss Dielectric and Liquid Metal Conductor," in Proc. IEEE MTT-S International Microwave Symposium, 2018, pp. 59-62,

[22]G. Venanzoni, C. Tomassoni, M. Dionigi, M. Mongiardo, and R. Sorrentino, "Design and Fabrication of 3-D Printed Inline Coaxial Filters With Improved Stopband," IEEE Transactions on Microwave Theory and Techniques, vol. 68, no. 7, pp. 2633-2643, July 2020.

[23]M. Uhm, K. Kim, and D. S. Filipovic, "Ultra-Wideband Bandpass Filters Using Quarter-Wave Short-Circuited Shunt Stubs and Quarter-Wave Series Transformers," in *IEEE Microwave and Wireless Components Letters*, vol. 18, no. 10, pp. 668-670, Oct. 2008,

[24]Dan B. Marghitu, “Mechanical Engineer’s Handbook”, A volume in Academic Press Series in Engineering, 2001,

[25]ISO Standard, [Online]. Available: https://www.iso.org/ics/77.040.10/x/

[26]Fracture and Fatigue Emanating from Stress Concentrators by G. Pluvinage Université de Metz, Metz, France, Springer, 2004,

[27]Beatriz Henriques, Mariana Carvalho, Sérgio M. O. Tavares, Paulo M. S. T. de Castro, “A Comparison of Safety Factor Values for Soderberg and DIN 743 Fatigue Analysis”, University of Porto, Vol. 7, No. 2, 2021,

[28]Thomas G. Digges and Samuel J. Rosenberg, “Heat Treatment and Properties of Iron and Steel”, UNITED STATES DEPARTMENT OF COMMERCE, NATIONAL BUREAU OF STANDARDS, 1960,

[29]Pozar, D.M. Microwave Engineering. 4th Edition. Wiley, New York, 2011,

[30]J. D. Kraus, "The Helical Antenna," in Proceedings of the IRE, vol. 37, no. 3, pp. 263- 272,

[31]C. A. Balanis, Antenna Theory Analysis, and Design, Third Edition, Wiley, 2017.

[32]L. Boskovic, J. Cazden and D. Filipovic, "Design and Characterization of an All-Metal 3-D Printed Air-Dielectric Coaxial Line," in IEEE Microwave and Wireless Components Letters, doi: 10.1109/LMWC.2022.3157553.

[33]L. Boskovic , I. Pisani , J. Cazden, and D.S. Filipovic, E. Lier, T. Hand, W. Neill Kefauver, “Design and Characterisation of a 3D Printed Helical Antenna Monoliticaly Integrated and Fed by an Air-Loaded Coaxial Line” Antenna Application Symposium, Urbana-Champaign, Ilinois 2021.

[34]D.J. Kozakoff, Analysis of Radome-Enclosed Antennas, 2nd ed., Norwood, MA: Artech House, 2010.

[35]L. Boskovic, M. Ignatenko, C. Andrews, R. Hasse, and D. S. Filipovic, "Electro-mechanical analysis of flat radomes for airborne antennas at K/Ka/V-band," 2017 IEEE International Symposium on Antennas and Propagation & USNC/URSI National Radio Science Meeting, 2017, pp. 497-498.

[36]Standard Atmosphere [Online]. Available: http://www.ilpi.com/msds/ref/stp.

[37]Thermo-electric Pump [Online]. Available: https://tinkersphere.com/electronic-components/358-peltier-thermoelectric-cooler-40x40mm.html

[38]Thermo-electric Pump Diagram [Online]. Available: https://www.meerstetter.ch/compendium/peltier-elements

[39]Temperature Chambers [Online]. Available: https://www.nlr.org/capabilities/antennas-flight-testing/

[40]Temperature Chambers [Online]. Available: https://www.yaswas.com/clean-temperature-humidity-chamber-th-cr-270.html#

[41]Autodesk Computational Fluid Dynamics [Online]. Available: https://www.autodesk.com/products/cfd/overview